TRANSIENT BEHAVIOR OF AN SF_6 POST-ARC CHANNEL ON HIGH CURRENT ARC INTERRUPTION

YASUNORI TANAKA

TRANSIENT BEHAVIOR OF AN SF_6 POST-ARC CHANNEL ON HIGH CURRENT ARC INTERRUPTION

by

YASUNORI TANAKA

A dissertation submitted to the Department of Electrical Engineering,
Nagoya University for the degree of Doctor of Philosophy in Engineering

March 1998

Contents

Chapter 1 Introduction

1.1 Duties and functions of circuit breakers

In the face of ever increasing electric power energy demand, electric power systems have considerably grown in size. For example in Japan, by the year 1996 itself, the total generating capacity and the total electrical energy output have reached to the remarkable figures of 233 737 MW and 1 009 349 GWh, respectively [1]. To cope up with these growths, the nominal line voltage of the underlying EHV/UHV transmission networks has been raised from time to time from the view point of economic reasons. The highest nominal voltage over the world is in Russia where the network rated at 1150 kV has been in operatation since 1985 [2]. In Russia, the transmission line length for 1150 kV has already reached 2500 km including the lines under construction. In the United States, experimental transmission lines for 1500 kV were constructed around Chicago in 1976, and experimental investigations have been carried out [2]. In Japan, the highest nominal line voltage of transmission networks has been raised to 500 kV since 1973. Transmission lines rated at 1000 kV has already been built from Shin-Imaichi to Higashi-Yamanashi via Nishi-Gumma although it is being operated at 500 kV [3]. The plan to construct another transmission systems rated at 1000 kV is underway.

On the other hand, besides the economic factors, the high quality and high reliability of electric power are required for ensuring steady voltage and frequency as well as avoiding any kind of blackouts. These requirements arise, for example, from the dramatic increase in the computer applications to industrial as well as other sectors, since these computer equipment cannot normally operate if the electric power supply is cut off for a few hundred milliseconds. Under such circumstances, the duties imposed on a circuit breaker become

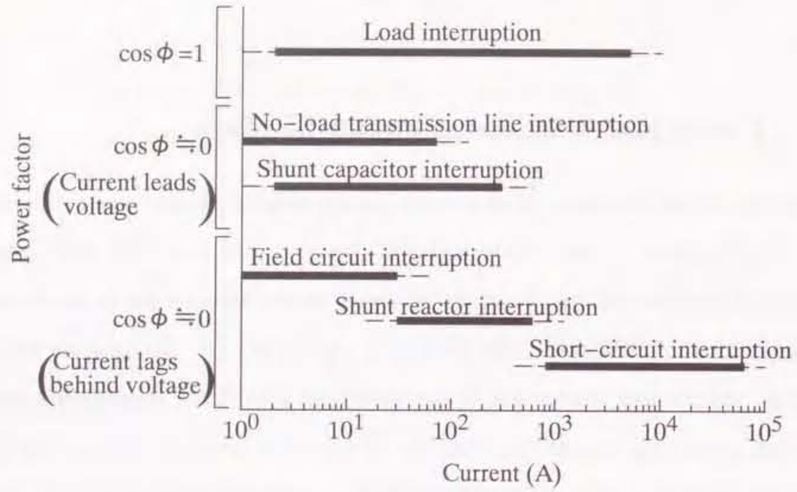

Figure 1.1. Current flowing through a circuit breaker [6].

severe in maintaining high reliability.

The circuit breaker has main four duties : (1) to switch electrical power networks on, (2) to allow to flow current without impediment in a network under normal operating conditions, (3) to interrupt the flow of excessive current in a faulty network, and (4) to interrupt load current under various circumstances [4, 5]. It is also required to insulate one contact from the other in the 'open' state. Furthermore, it is necessary to perform these duties in a time as short as possible with high reliability. Figure 1.1 indicates the typical current which a circuit breaker must interrupt in different cases [6]. In this figure, the power factor based current classification is given. It should be noted that a circuit breaker must be able to interrupt currents in extremely wide range.

The most severe and important duty of a circuit breaker is to interrupt short-circuit

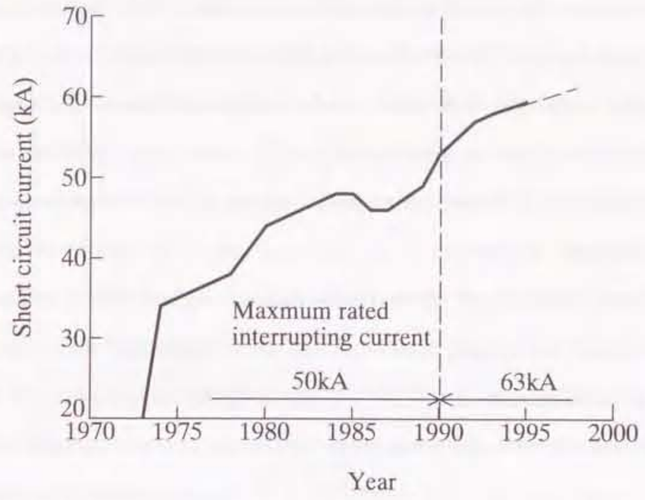

Figure 1.2. Short-circuit currents in ac transmission network in Japan [7].

currents. The severity of this duty imposed on circuit breakers has increased immensely as a result of growth in network size. Figure 1.2 shows the continuous increase in short-circuit current on 500 kV transmission network over the years in Japan [7]. It should be pointed out that the short-circuit current has exceeded 50 kA since 1990. With the increase in the short-circuit current, an interruption capability of a circuit breaker has also steadily increased. In 1993, a one-break SF_6 puffer circuit breaker rated at 550 kV–63 kA was developed in Japan [7].

1.2 Alternating current interruption

One of the duties of a circuit breaker is to switch off a faulty part of the network. The circuit breaker is tripped by a protection system. As soon as the contacts open, an electric

arc is formed across the electrodes. Through the arc, the current continues to pass without getting interrupted. The flowing current heats the arc as a result of joule heating, making the arc temperature 10 000–20 000 K during high current phases. Such high-temperature arcs are usually considered to be under local thermal equilibrium condition where heavy particles and electrons have an identical temperature, since the circuit breaker has internal pressures above 0.1 MPa. From this point of view, the arc in a circuit breaker is identified as a kind of thermal plasmas.

The arc with temperatures above 10 000 K has a high electrical conductivity above 3000 S m^{-1}. Under the certain conditions, the arc is established until a natural current zero of the alternative current waveform is reached. At current zero, the joule heating effect turns out to be zero. If the loss power in the arc at current zero is high enough to decline temperature and electrical conductivity of the arc, the arc is quenched and the flowing current is interrupted.

It has been recognized that an electric arc is a switching element for high-current interruption, since the arc can change its resistance not only very rapidly, but also automatically and synchronously with the change in the alternating current. Thus, the high-current interruption is to control the resistance of the arc plasma.

High-voltage circuit breakers have two types of current interruption failure. One is a thermal failure, and the other is a dielectric failure. These two types of failures are interpreted as follows : At current zero, there remains hot gas with temperatures about 6000 K between the contacts. This hot gas is referred to as a post-arc channel. It has still higher electrical conductivity than SF_6 gas at a temperature of 300 K. On the other hand, the network reacts to this circuit interruption by transient oscillations which cause a so-called transient recovery voltage TRV across the circuit breaker. During the imposition of high TRV, the current, occasionally with a few amperes, passes through the post-arc channel. This current is called a post-arc current. If the post-arc current reduces to zero, the current interruption is achieved.

However, when the rate of rise of the TRV, dv/dt, frequently abbreviated as RRRV, is greater than a critical value, the post-arc current cannot reduce to zero and the decaying arc channel is re-established by joule heating immediately after current zero. This failure is called a thermal failure. This failure can be determined only after a lapse of several microseconds following current zero. Thus, this period is referred to as a thermal failure mode, which is controlled by the energy balance. Figure 1.3 shows test oscillograms of voltage across the electrodes for the case which were taken for an SF_6 circuit breaker at 72 kA [4]. The rate of rise of the TRV after current zero is about 2 kV μs^{-1}. The oscillogram (a) shows a successful interruption, whilst (b) represents a thermal failure. As shown in Fig. 1.3 (b), the voltage across the electrodes deviates from the TRV in the case of (a) at about 2 μs after current zero and become equal to the arc voltage after a time period of several micro-seconds.

After a successful thermal interruption, the TRV may reach such a high peak value that the circuit breaker gap fails through dielectric breakdown. This is called a dielectric failure in the peak region of recovery voltage. Figure 1.4 shows test oscillograms of voltage across the electrodes for this mode. The oscillogram in Fig. 1.4 (a) shows a successful interruption, while that in (b) depicts the occurrence of a breakdown close to the peak. It is noted that the voltage decay occurs so fast that it cannot be resolved on the oscillogram. This is a typical feature of the dielectric failure.

The existence of these two basic failure modes, each having different properties, has important consequences to the range of application of a circuit breaker. Among the wide variety of possible fault locations and network conditions, only those types of faults are of interest, which produce the highest stresses owing to the two crucial parameters dv/dt and a peak value of the TRV together with the level of the short-circuit current.

For the thermal interruption mode, the critical fault is the one which occurs on a line at a certain distance from the circuit breaker. The most severe stresses in TRV occur in the case of relatively short lines a few kilometers in length, since TRV has a waveform

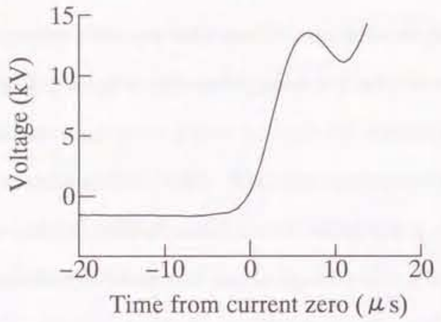

(a) Successful interruption

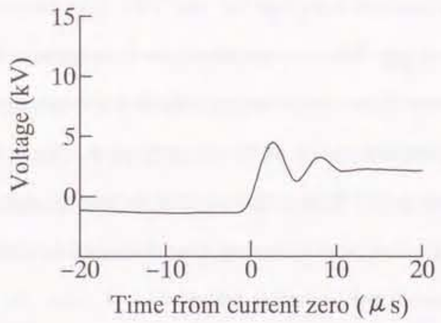

(b) Thermal failure

Figure 1.3. Transient recovery voltage in the thermal recovery region for an SF_6 circuit breaker(interrupting current is 72 kA) [4].

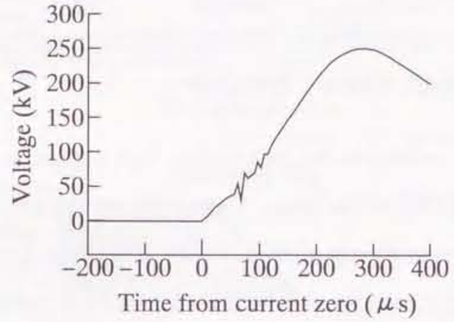

(a) Successful interruption

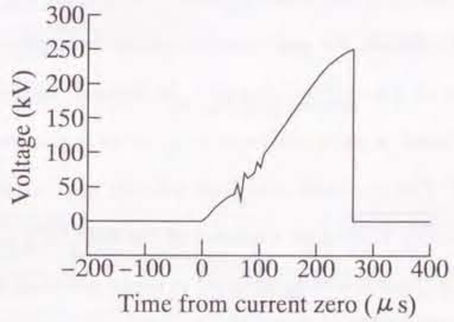

(b) Dielectric failure close to the peak of the TRV

Figure 1.4. Transient recovery voltage in the dielectric recovery region for an SF_6 circuit breaker(interrupting current is 50kA) [4].

like the teeth of a saw arisen from the reflection of voltage wave at terminals. The fault is therefore called a short-line fault (SLF). Practical experience shows that in the dielectric failure mode, the critical fault is the so-called terminal fault (TF), which occurs at the terminals of the circuit breaker.

1.3 SF_6 gas-blast circuit breaker

One of the effective techniques for interrupting high current is to blow the gas along the axial direction of the arc discharge. Figures 1.5 (a) (b) and (c) illustrates the cross section of a gas-blast circuit breaker schematically. The circuit breaker consists of a puffer chamber. The moving contact has the shape of a hollow tube. When the contacts separate, an electric arc is formed across the arcing contacts as shown in Fig. 1.5 (b). The presence of the arc produces a blocking effect on the nozzle preventing gas from flowing freely out of the puffer chamber. Hence, the gas pressure inside the puffer chamber increases to a high value, depending on the current intensity. At natural passage through current zero, the gas pressure will reach a value sufficient to produce a gas blast across the arc space in the axial direction. The gas blast with high velocity may remove a significant portion of heat in the arc, thereby leading to a quench of the arc. As a medium of the gas blast, sulfur hexafluoride (SF_6) gas is widely adopted in many gas-blast circuit breakers because of its excellent arc quenching ability.

Pure SF_6 gas is colorless, odorless, tasteless, non-toxic and non-flammable. It is also chemically stable, so it neither decomposes nor attacks ordinary materials of construction at temperatures below 425 K. It gets dissociated under the high-temperature arc column, however, the components recombine so that the net amount of decomposition products formed is actually very small. The electrical properties including the voltage withstand and arc quenching capabilities are very important for its use in high-voltage circuit breakers. The remarkable performance of SF_6 as an interrupting medium is largely due to its

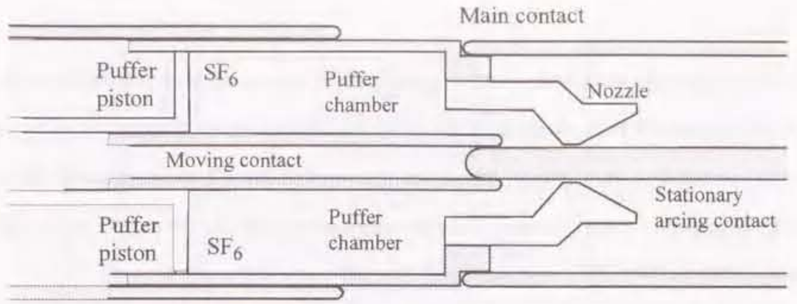

(a) Closed position

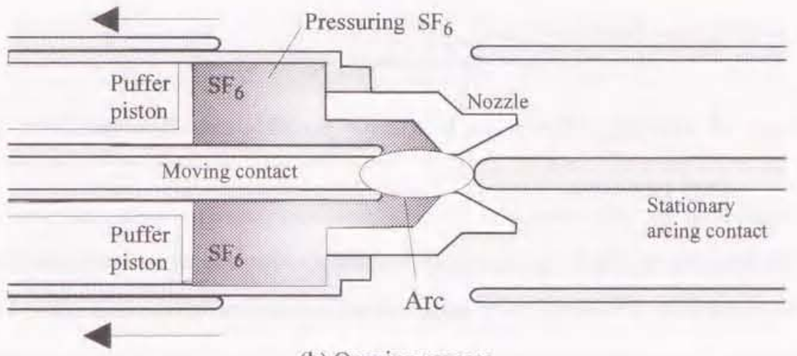

(b) Opening process

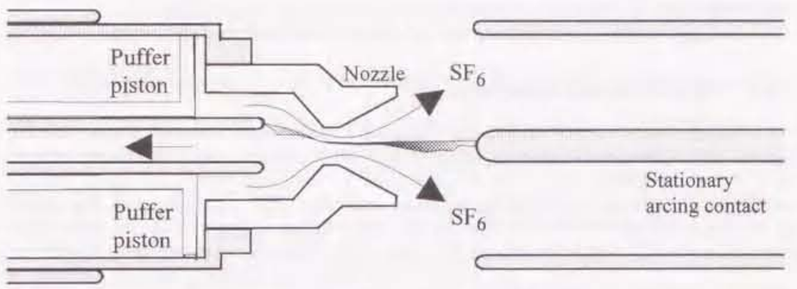

(c) Contact separation

Figure 1.5. Sequence of an opening operation in a gas-blast circuit breaker.

ability to recover dielectric strength quickly after the arc current passes through zero. One of the important performances of an arc-quenching medium is represented by its thermal time constant at the instant when the arc current passes through zero. In accordance with Frind *et al.* , the thermal time constant was found to be only 1 μs for SF_6 arcs, as compared to 100 μs for nitrogen arcs [8].

The use of SF_6 gas with such excellent properties permits the drastic development of a gas-blast circuit breaker. At present, one-break gas-blast circuit breakers rated at 550 kV–63 kA have been developed.

1.4 A survey of research works on SF_6 gas-blasted arc quenching process

The current interruption phenomenon has not yet been elucidated completely because of its complexity. Therefore, many engineers and researchers have concentrated their works on both the experimental and theoretical investigations relating the current interruption processes. In this section, the survey of recent investigations on SF_6 arcs is made from the viewpoints of both experimental and theoretical approaches.

1.4.1 Experimental approach

Numerous experimental investigations have been carried out to measure only macroscopic parameters such as the voltage applied between the contacts and the current flowing through a circuit breaker around current zero. However, recent investigations have been focused to obtain physical information concerning an arc itself, for example, arc diameter, temperature, pressure, electron density and/or radiation transfer [9]–[26].

Lewis *et al.* have measured diameters of arcs across the Cu-W electrodes for 78 Hz current in a model SF_6 gas-blast circuit breaker [15]. Figure 1.6 shows typical arc diameter variations near nozzle throat with time during the 10 μs before current zero for three

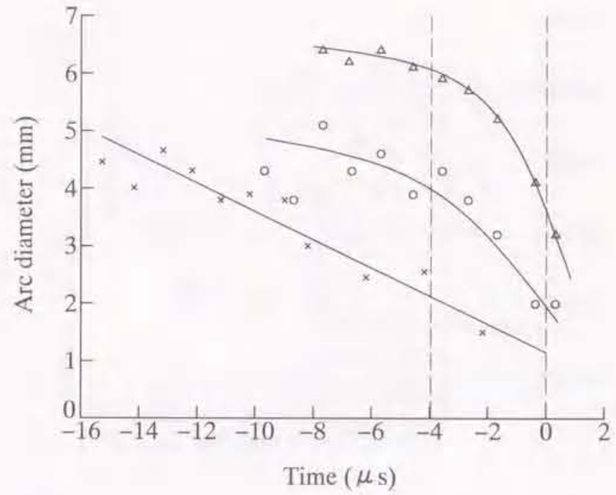

Figure 1.6. Arc diameter variations near nozzle throat in a model SF_6 gas-blast circuit breaker for three current decay rates ; ×, 15 A μs^{-1} ; ○, 16.5 A μs^{-1} ; △, 20.5 A μs^{-1} [15].

different current decay rates di/dt of 15, 16.5 and 20.5 A μs^{-1}. It is indicated that an arc diameter increases proportionally with the absolute value of current decay rates di/dt.

Lewis *et al.* also have measured arc temperature around current zero for current frequency of 78 Hz by the two-line method of Cu spectral lines at wavelengths of 515.3 and 510.5 nm [16]. Figure 1.7 represents the variations of radially averaged arc temperature at current zero with di/dt. There is an evidence of a distinct increase in the average arc temperature above a di/dt of about 20 A μs^{-1}.

Ikeda *et al.* have measured radial radiation distribution of S, F and Cu spectral lines [17]. From the analysis of profiles of these spectral lines, it was found that the temperature was less at the center of the arc than at the edge due to an increase in the copper vapor concentration around the center of the arc during peak current phase of 30 kA.

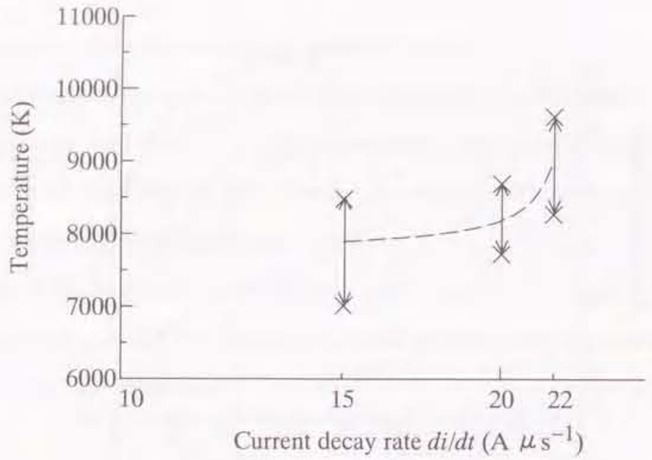

Figure 1.7. Average arc temperature at current zero in a model SF_6 gas-blast circuit breaker [16].

The pressure, which is significant for gas-blast effect, in a puffer chamber in a gas-blast circuit breaker has been measured. Mori *et al.* have measured pressure in the puffer chamber in a model gas-blast circuit breaker rated at 50kA [21]. They compared pressure rises in the chambers of gas-blast circuit breakers in different cases : the one with an additional nozzle, what is called an inner-nozzle, on the end of the movable arcing contact and the other without inner-nozzle. Figure 1.8 shows the pressure rises during SLF interruption of 90% of rated interrupting current. In Fig 1.8, it can be seen that the pressure rise in the model gas circuit breaker with an inner-nozzle is 1.24 times higher than that without an inner-nozzle, and the circuit breaker is improved enough to interrupt a current of 63kA by installing the inner-nozzle. They concluded that the installation of the inner-nozzle for the pressure rise successfully contributed to the improvement of the SLF interruption performance.

During the peak current phase, a sufficient amount of power is dissipated to produce

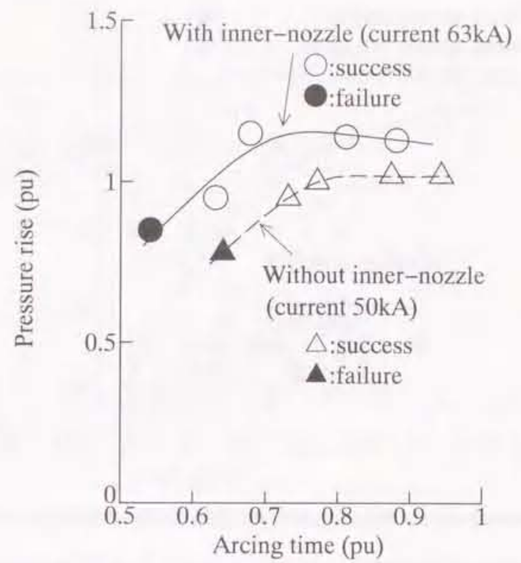

Figure 1.8. Pressure rise at SLF 90% interruption in a model gas-blast circuit breaker [21].

substantial evaporation of the electrode material. The metallic vapor may affect the interrupting capability of a circuit breaker, because it enhances the electrical conductivity. Jones *et al.* carried out spectroscopic observations between the Cu-W electrodes in a model SF_6 gas-blast circuit breaker in a wavelength range of 510–516 nm [23]. Figure 1.9 depicts the correlated results between the occurrence of W spectral lines and the failure of current interruption at a upstream pressure of 4.25 bar. They found the approximate correlation between the occurrence of W line emission at the critical instant of current zero and a deterioration in the current interrupting ability of the circuit breaker.

Maftoul *et al.* have observed a sustained current conduction in the breaking chamber from measurements of post-arc current across an SF_6 puffer circuit breaker after a current interruption for peak current of 36 kA [25]. They concluded that the conduction was due

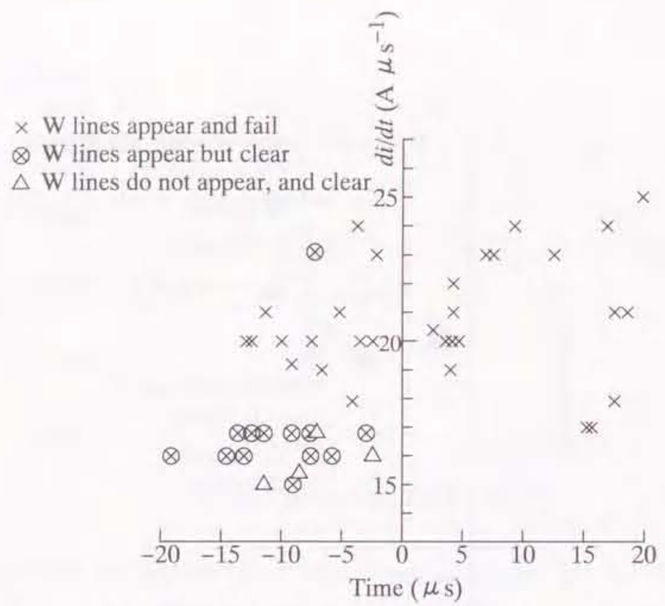

Figure 1.9. Correlation between the occurrence of W lines and failure of current interruption in a model SF_6 circuit breaker. Upstream pressure is 4.25 bar absolute [23].

to mainly S_2^+ and found that the temperature of the conducting gas was about 2000 K after 5ms from current zero.

In the region after current zero, however, the radiation intensities of spectral lines are too low to be detected even with high sensitive equipment. Therefore, few research papers on diagnosis of a post-arc channel after current zero have been published in the open literature.

1.4.2 Theoretical and numerical approach

Theoretical calculations for an arc can be distinguished as follows : one is to theoretically calculate fundamental data on SF_6 properties including radiation transfer, composition, relaxation time, transport and thermodynamic properties [27]–[33], and the other is to simulate dynamic behavior of the arc and hot gas using the fundamental data by means

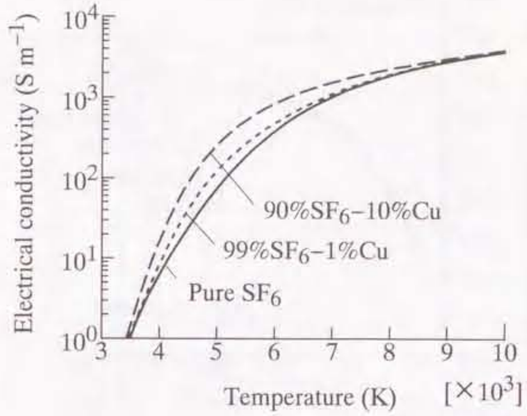

Figure 1.10. Electrical conductivity of SF_6-Cu mixture at a pressure of 0.1 MPa as a function of temperature [27].

of computer fluid dynamics techniques [34]–[56].

Chervy *et al.* have calculated the equilibrium composition and transport and thermodynamic properties of SF_6-Cu mixture in a wide temperature range of 300–30 000 K, taking into account the contamination with Cu vapor injected from the electrodes in a circuit breaker [27]. Figure 1.10 illustrates the electrical conductivity of SF_6-Cu mixture as a function of temperature at a pressure of 0.1 MPa. It is revealed from this figure that electrical conductivity increases remarkably in proportion to Cu vapor concentration.

An arc radiates extreme insensitive light. The quantity of light emission is one of the important factors to formulate the energy balance in the arc. Gleizes *et al.* have calculated the net emission coefficient radiated from cylindrical SF_6-Cu arc column [30]. Figure 1.11 shows the calculated results. The emission radiated at the center of an arc is absorbed at its cool edges. Therefore, the net emission coefficient decreases with increasing arc radius.

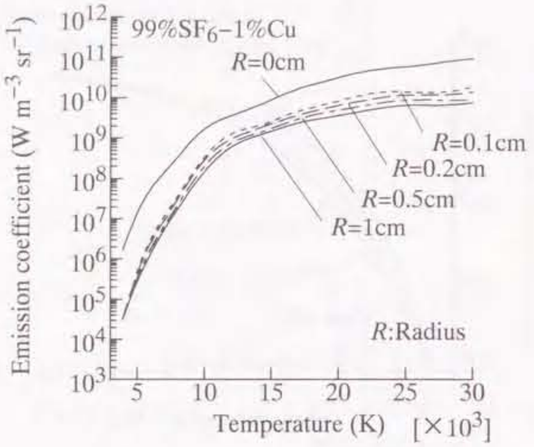

Figure 1.11. Influence of plasma thickness on the net emission coefficient of SF_6-Cu mixture : Pressure, 0.1 MPa [30].

They also pointed out that the decrease in emission radiated outside leads to a change in temperature profile of an arc.

Recent developments in computer fluid dynamics techniques enable the transient arc plasma to be simulated. The flow velocity and temperature profiles of SF_6 in a circuit breaker have been attempted to be computed by solving simultaneous equations, i.e. the mass, momentum and energy conservation equations on the assumption of local thermal equilibrium LTE.

For the prediction of thermal failure, many researchers have calculated arc behavior before and after current zero. Fang *et al.* have analyzed arc behavior such as arc temperature, mass density, pressure and flow velocity in a model SF_6 gas-blast circuit breaker [50]. The turbulent effect on the arc cooling was taken into account using Prandtl mixing length model. Figure 1.12 demonstrates the calculated radial temperature distri-

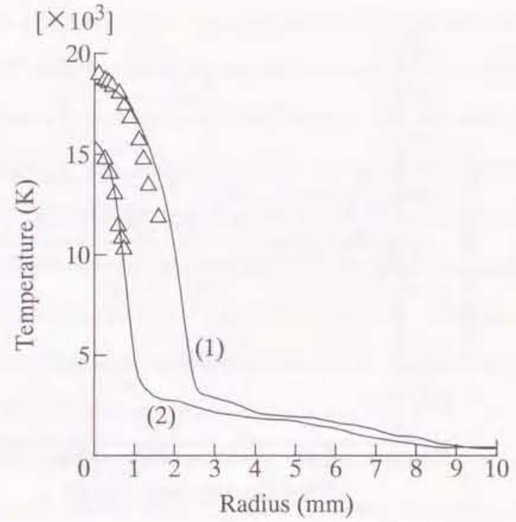

Figure 1.12. Comparison between calculated and measured temperature profiles at nozzle throat for Aachen nozzle : △ experimental results. Stagnation pressure 0.9 MPa, peak value of current I_0=1000A, di/dt=16A μs^{-1}. Instantaneous current (1) 600 A ; (2)100 A [50].

bution in an SF_6 arc at a stagnation pressure of 0.9 MPa at the nozzle throat in Aachen nozzle. Taking the turbulent effect into account leads to the calculation results that agree with experimentally obtained temperature profiles. They pointed out in their paper that the turbulent cooling effect dominated the temperature decay in downstream region.

Further developments have been made in computational tools and in arc modeling methods. Trepanier *et al.* have developed a computational fluid dynamics tool capable of calculating self-induced magnetic field [51]. Tong *et al.* have analyzed the arc and hot gas behavior during current interruption not only in the thermal mode but also in

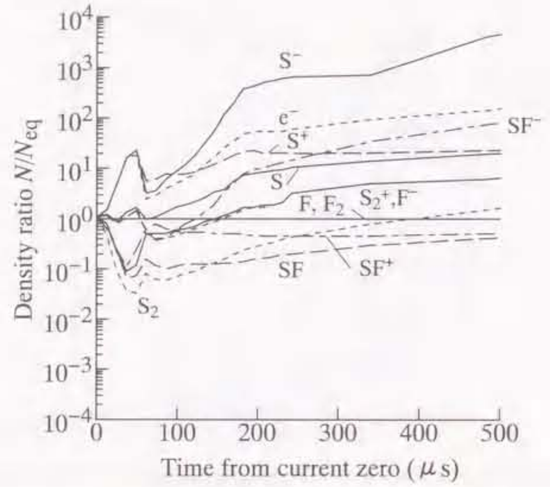

Figure 1.13. Decay of relative particle concentrations. The denominator is the density of the partial diatomic equilibrium [58].

the dielectric mode of an SF_6 circuit breaker [55]. Blundel *et al.* have investigated the similarity and scaling law of arc in a circuit breaker [56].

In the computation of arc behavior with a fluid model, local thermal equilibrium LTE is assumed to be established in the arc. However, LTE may not always be established in a transient arc or in an arc under high electric field [57]. Recently, many calculations of particle compositions have been seen in the open literature, considering these non-equilibrium effects [58]–[67].

When an arc temperature decays too rapidly compared with the time taken in chemical reactions, chemical equilibrium may not exist in a post-arc channel. Brand and Kopainsky have used reaction kinetics to analyze time variation in particle densities without applying

recovery voltage [58]. Figure 1.13 illustrates decay of relative particle concentrations with a rapid temperature decrease. It is concluded that during about 100 μs after current zero there is a strong deviation from the equilibrium and the overpopulation of electron density. Similar analyses have been made by Gleizes *et al.* [59] and Adamec *et al.* [67] for particle compositions of SF_6 plasma under non-chemical equilibrium conditions.

During the post-arc phase in SF_6 gas-blast circuit breakers, high electric field strengths are applied to the post-arc channel, originating from the recovery voltage. Such high electric field strength elevates the kinetic energy of the electrons. Furthermore, electrons may have non-Maxwellian distribution functions depending on the electric field strength. Taking non-maxwellian effect in electron energy distribution functions into account, Gonzalez *et al.* have investigated the effects of the electric field on the electrical conductivity of SF_6 plasma in a model circuit breaker [61]. Figure 1.14 shows time variations of the post-arc current for RRRV=7 kV μs^{-1} while taking into account the influence of electric field strength on the electrical conductivity. The results show that the presence of the electric field increases the electrical conductivity generally and thus decreases the calculated interruption capability.

1.5 Purposes and composition of the dissertation

1.5.1 Purposes of the dissertation

As mentioned in the preceding sections, many investigations have been performed on the arc phenomena before current zero. This is due to the fact that the spectral lines can be readily measured to analyze an arc. However, few research work on the post-arc channel after current zero have been performed since the diagnosis of a post-arc channel is very difficult. Therefore it is desirable to measure the post-arc parameters such as a post-arc temperature, metallic vapor concentration and electron density in an SF_6 post-arc channel.

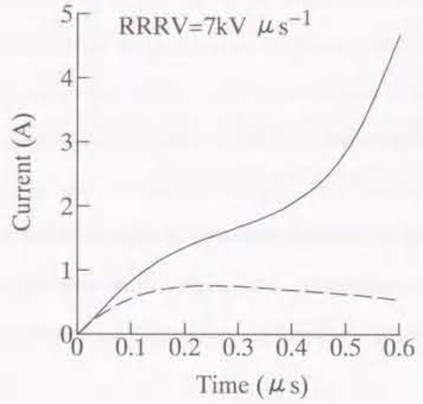

Figure 1.14. Variations of the post-arc current for RRRV=7 kV μs^{-1}, with (full curves) and without (dotted curves) taking into account the influence of electric field strength on electrical conductivity [61].

One of the purposes of the present study is to experimentally elucidate transient variations in physical parameters such as temperature, metallic vapor concentration and electrical resistivity in an SF_6 gas-blasted arc both before and after current zero during current interruption processes. In order to attain these purposes, a method for measuring transient temperature below 6000 K in a post-arc channel with spectroscopic techniques is devised [68]. Using the devised method, the arc temperature is measured along the nozzle axis in a flat-type SF_6 gas-blast quenching chamber [68, 69]. Furthermore, a new method for estimating metallic vapor concentration in a post-arc channel is developed [70]–[72]. In addition, a new interpretation is given to the arc interruption processes from the viewpoint of an increase in electrical resistivity [73, 74].

Another purpose of this study is to derive fundamental data on SF_6 plasma under the non-thermal equilibrium. A post-arc channel is exposed to high electric field. The high electric field elevates kinetic energy of electrons in a post-arc channel, resulting in a rise of electron temperature T_e even if at a high pressure of 0.1 MPa. As a result, T_e may become greater than gas temperature T_g. In such a two-temperature situation, the particle composition may differ from that under the thermal equilibrium. Thus, the particle composition is revealed theoretically on the basis of second law of thermodynamics for two-temperature SF_6 plasmas [75, 76].

1.5.2 Composition of the dissertation

The present dissertation is composed of the following six chapters :

Chapter 1 is the introduction of this dissertation. The survey of the progress and the remaining problem for elucidation of SF_6 gas-blasted arc interruption phenomena is described

In chapter 2, an estimation of transient axial temperature distribution in a post-arc channel in a flat-type SF_6 gas-blast quenching chamber is described [68, 69]. In order to decide two spectral lines for estimating post-arc temperature by the two-line method,

emission coefficients for 132 Fe spectral lines are calculated together with those for spectral lines of particles concerned with SF_6 gas and electrode materials. These calculations show that Fe spectral lines at wavelengths of 426.0 and 442.7 nm have much higher emission coefficients than S^+, F or Cu at temperatures below 5000 K, and these two spectral lines are suitable for the temperature estimation below 5000 K. In the practical experiment, iron is intentionally used as the electrode material in a flat-type SF_6 gas-blast quenching chamber. Measurements of radiation intensities of these two Fe spectral lines make it possible to estimate post-arc temperature below 3500 K at 100 μs after current zero in the chamber. Owing to these temperature estimation, axial temperature distribution is acquired.

In chapter 3, the axial distribution of iron vapor concentration X_{Fe} in a SF_6 post-arc channel in a flat-type SF_6 gas-blast quenching chamber with iron electrodes is described [71, 72]. A method for estimating X_{Fe} is developed on the basis of spectroscopy, which utilizes the relative radiation intensity of background spectra at 455.0 nm to Fe spectral line at 426.0 nm. As the method requires theoretical data on emission coefficients of background spectra and Fe spectra, the coefficients are thus calculated. From these calculations, it is observed that the background spectra at 455.0 nm have not only continuous contribution but also those of S_2 spectra [70]. It is shown that the method is capable of estimating iron vapor concentration X_{Fe} up to 100 μs after current zero. It is also found that X_{Fe} is of the order of 0.01% around current zero along the arc axis in the chamber.

In chapter 4, a new concept of 'thermal plasma contacts' is described in order to interpret the behavior of a post-arc channel from the viewpoint of transient axial electrical resistivity distribution in a post-arc channel [73]. It is represented that fictitious 'thermal plasma contacts' are present in front of the practical metallic electrodes. The thermal plasma contacts are found to open in the axial direction during arc quenching period. It is also revealed that the fictitious contacts have the opening velocity exceeds 100 m s^{-1}.

Furthermore, behavior of the thermal plasma contacts applied TRV of the order of 2 or 3 V μs^{-1} was discussed [74]. From these discussions, an interpretation on thermal failure and successful interruption is given [74].

In chapter 5, particle compositions and electrical conductivity of SF_6 plasmas are calculated considering the non-equilibrium effect, i.e. two-temperature effect [75, 76]. In the calculation of particle compositions, effective excitation temperature is newly introduced in order to express the populations of the internal states of heavy particles in high-pressure and high-gas temperature plasma in two-temperature steady state. From the calculation results, the effect of an increase in electron temperature is described on the variation in particle composition and electrical conductivity of SF_6 plasmas.

In chapter 6, the conclusions of the present dissertation are summarized and the scope for the future research work is also given.

References are listed cumulatively at the end of each chapter.

References

[1] *Hand Book of Electric Power Industry*. Tokyo : Nippon Electric Society, 1997 (in Japanese).

[2] Y. Yamagata and H. Suzuki, *Technical Report of Mitsubishi Electric Cooporation*, Vol. 69, pp.872–876, 1995.

[3] T. Takebe and T. Komaba, "Great advanced transmission technology", *J. IEE Japan*, Vol. 116, pp.651–653, 1996 (in Japanese).

[4] T. E. Browne, *Circuit Interruption, Theory and Techniques*. New York : Marcel Dekker, 1984.

[5] C. H. Flurscheim, *Power Circuit Breaker Theory and Design*. England : Peter Peregrunus, 1982.

[6] Y. Kito, *Electric Energy –Its Generation and Transmission –*. Tokyo : Corona, 1995, p.181 (in Japanese).

[7] *Technical Report of IEE of Japan*, No.497, 1995 (in Japanese).

[8] G. Frind, "Über der Abklinken von Lichtbogen I", *Z. Angewandte Phys.*, Vol. 12, pp.231–237, 1960.

[9] D. R. Airey, P. H. Richards and J. D. Swift, "Time-resolved radial temperature profiles for 10 kA SF_6 arcs", *J. Phys. D: Appl. Phys.*, Vol. 27 pp.1982–1993, 1975.

[10] W. Hermann, U. Kogelschatz, L. Niemeyer, K. Ragaller and E. Schade, "Investigation on the physical phenomena around current zero in HV gas circuit breakers", *IEEE Trans. Power Appar. Syst.*, Vol. 95, pp.1165–1176, 1976.

[11] D. R. Airey, "Time dependent energy balance of a 20 kA SF_6 arc contaminated with electrode vapor", *in Proc. 5th Int. Conf. on Gas Discharges and Their Applications*, 1978, pp.21–24.

[12] J. P. Dinguirard, C. Espardeillier and S. Vacquie S, "Study of an extinguishing arc discharge in copper nitrogen mixture", *in Proc. 5th Int. Conf. on Gas Discharges and Their Applications*, 1978, pp.143–143.

[13] D. R. Airey, "A rapid-scanning polychromator for time-resolved temperature and radius measurements in 40 kA SF_6 arcs", *J. Phys. E: Sci. Instrum.*, Vol. 12, pp.397–402, 1979.

[14] D. Leseberg and G. Pietsch, "Optical investigations on a SF_6 switching arc inside a glass nozzle", *in Proc. 7th Int. Conf. on Gas Discharges and Their Applications*, 1982, pp.9–12.

[15] E. Lewis , N. Y. Shammas and G. R. Jones, "The current zero SF_6 blast arc at high di/dt", *in Proc. 8th Int. Conf. on Gas Discharges and Their Applications*, 1985, pp.35–38.

[16] E. Lewis E, A. N. Prasad and G. R. Jones, "Current zero spectroscopy of a high power SF_6 circuit breaker arc", *in Proc. 8th Int. Conf. on Gas Discharges and Their Applications*, 1985, pp.31–34.

[17] H. Ikeda, G. R. Jones, M. Irie and A. N. Prasad, "Spectroscopy of very high current, convection arcs", *in Proc. 7th Int. Conf. on Gas Discharges and Their Applications*, 1982, pp.5–8.

[18] S. Vacquie, A. Gleizes and H. Kafrouni, "Measurements of electron density in a SF_6 arc plasma", *J. Phys. D: Appl. Phys.*, Vol. 18, pp.2193–2205, 1985.

[19] K-P. Hinz, "Optical diagnostics of SF_6 high-current discharges", *J. Phys. D: Appl. Phys.*, Vol. 19, pp.2381–2391, 1986.

[20] S. M. El-Kholy, G. R. Jones and E. Lewis, "Evaluation of the spectra of decaying arcs in gas blast circuit breakers", *in Proc. 9th Int. Conf. on Gas Discharges and Their Applications*, 1988, pp.43–46.

[21] T. Mori , H. Ohashi, H. Mizoguchi and K. Suzuki, "Investigation of technology for developing large capacity and compact size GCB", *IEEE Trans. Power Delivery*, Vol. 12, pp.747–753, 1997.

[22] D. W. Shimmin, G. R. Jones and S. M. G. Ali, "Transient pressure variations in SF_6 puffer circuit breakers", *J. Phys. D: Appl. Phys.*, Vol. 23, pp.533–541, 1989.

[23] G. R. Jones, W. Hu and S. M. El-Kholy, "A spectroscopic investigation of electrode material entrained into the extinguished arc of an SF_6 circuit breaker", *J. Phys. D: Appl. Phys.*, Vol. 21, pp.1414–1420, 1988.

[24] V. W. Smith and A. D. Stokes, "Arc-gas flow structures in gas blast arcs in plane-parallel nozzles", *in Proc. 10th Int. Conf. on Gas Discharges and Their Applications*, 1992, Vol. I, pp.34–37.

[25] J. Maftoul, M. Barrault, G. Bernard, P. Chevrier and S. Rowe, "Study of the post-recovery current in SF_6 circuit breakers", *J. Phys. D: Appl. Phys.*, Vol. 28, pp.1133–1140, 1995.

[26] V. W. Smith and A. D. Stokes, "Experimental and theoretical studies of temperature and radiation in gas-blast arcs in plane-parallel nozzles", *in Proc. 11th Int. Conf. on Gas Discharges and Their Applications*, 1995, Vol. I, pp 54–57.

[27] B. Chervy, A. Gleizes and M. Razafinimanana, "Thermodynamic properties and transport coefficients in SF_6-Cu mixtures at temperatures of 300–30 000 K and pressures of 0.1–1 MPa", *J. Phys. D: Appl. Phys.*, Vol. 27, pp.1193–1206, 1994.

[28] A. Gleizes, A. A. M. Habib and S. Vacquie, "Calculation of electron-ion recombination in an SF_6 arc plasma", *J. Phys. D: Appl. Phys.*, Vol. 22, pp.1464–1470, 1989.

[29] A. Gleizes, B. Rahmani, J. J. Gonzalez and B. Liani, "Calculation of net emission coefficient in N_2, SF_6 and SF_6-N_2 arc plasmas", *J. Phys. D: Appl. Phys.*, pp.1300–1309, 1991.

[30] A. Gleizes, J. J. Gonzalez, B. Liani and G. Raynal, "Calculation of net emission coefficient of thermal plasmas in mixtures of gas with metallic vapor", *J. Phys. D: Appl. Phys.*, Vol. 26, pp.1921–1927, 1993.

[31] V. Aubrecht and J. J. Lowke, "Calculations of radiation transfer in SF_6 plasmas using the method of partial characteristics", *J. Phys. D: Appl. Phys.*, pp.2066–2073, 1994.

[32] G. Raynal, P. J. Vergne and A. Gleizes, "Radiative transfer in SF_6 and SF_6-Cu arcs", *J. Phys. D: Appl. Phys.*, pp.508–515, 1995.

[33] G. Raynal and A. Gleizes, "Radiative transfer calculation in SF_6 arc plasmas using partial characteristics", *J. Phys. D: Appl. Phys.*, pp.152–160, 1995.

[34] B. Chervy, H. Riad and A. Gleizes, "Calculation of the interruption capability of SF_6-CF_4 and SF_6-C_2F_6 Mixtures–part I : plasma properties", *IEEE Trans. Plasma Sci.*, Vol. 24, pp.198–209, 1996.

[35] B. Chervy, J. J. Gonzalez and A. Gleizes, "Calculation of the interruption capability of SF_6-CF_4 and SF_6-C_2F_6 Mixtures–part II : arc decay modeling", *IEEE Trans. Plasma Sci.*, Vol. 24, pp.210–217, 1996.

[36] B. Chervy, "The influence of the presence of tungsten on SF_6 arc plasmas", *J. Phys. D: Appl. Phys.*, Vol. 29, pp.2156–2161, 1996.

[37] V. Aubrecht, M. Bartlova and B. Gross, "Temperature of a wall-stabilised arc plasma with respect to radiative transport of energy", *in Proc. Symposium on Phys. Switching Arc*, 1996, pp.9–12.

[38] B. W. Swanson and R. M. Roidt, "Some numerical solutions of the boundary layer equations for an SF_6 arc", *Proc. IEEE*, Vol. 59, pp.493–501, 1971.

[39] W. Hermann and K. Ragaller, "Theoretical description of the current interruption in HV gas blast breakers", *IEEE Trans. Power Appar. Syst.*, Vol. 96, pp.1546–1555, 1977.

[40] E. Richley and D. T. Tuma, "Free recovery of the gas-blast arc column", *IEEE Trans. Plasma Sci.*, Vol. 8, pp.405–410, 1980.

[41] J. J. Lowke and H. Lee "A numerical study of a two-dimensional circuit breaker arc during current interruption", *in Proc. 8th Int. Conf. on Gas Discharges and Their Applications*, 1985, pp.54–56.

[42] R. R. Mitchell, D. T. Tuma and J. F. Osterle, "Transient two-dimensional calculations of properties of forced convection-stabilized electric arcs", *IEEE Trans. Plasma Sci.*, Vol. 13, pp.207–220, 1985.

[43] H. Ikeda, M. Ishikawa and S. Yanabu, "Analyses of axial energy distribution in decaying arc of SF_6 gas circuit breaker", *IEEE Trans. Plasma Sci.*, Vol. 14, pp.395–401, 1986.

[44] A. Gleizes, A. M. Rahal, H. Delacroix and P. V. Doan, "Study of a circuit-breaker arc with self-generated flow : part I–energy transfer in the high-circuit phase", *IEEE Trans. on Plasma Sci.*, Vol. 16, pp.606–614, 1988.

[45] A. Gleizes, A. M. Rahal, S. Papadopoulos and S. Vacquie, "Study of a circuit-breaker arc with self-generated flow : part II–the flow phase", *IEEE Trans. Plasma Sci.*, Vol. 16, pp.615–622, 1988.

[46] A. Gleizes, M. Mitiche and P. V. Doan, "Study of a circuit-breaker arc with self-generated flow : part III–the post-arc phase", *IEEE Trans. Plasma Sci.*, Vol. 19, pp.12–19, 1991.

[47] J. F. Zhang and M. T. C. Fang, "Dynamic behavior of high-pressure arcs near the flow stagnation point", *IEEE Trans. Plasma Sci.*, Vol. 17, pp.524–533, 1989.

[48] M. T. C. Fang and Q. Zhuang, "Current zero behavior of an SF_6 gas-blast arc. part I : laminar flow", *J. Phys. D: Appl. Phys.*, Vol. 25, pp.1197–1204, 1992.

[49] A. Gleizes, T. Robert, J. J. Gonzalez and A. Pons, "Modelling of the SF_6 circuit breaker arc and of its interaction with the circuit", *J. Phys. D: Appl. Phys.*, Vol. 26, pp.1439–1444, 1993.

[50] M. T. C. Fang, Q. Zhuang and X. J. Guo, "Current-zero behavior of an SF_6 gas-blast arc. part II : turbulent flow", *J. Phys. D: Appl. Phys.*, Vol. 27, pp.74–83, 1994.

[51] J. Y. Trepanier, H. Pellegrin, X. D. Zhang and R. Camarero, "Computational fluid dynamics tools for circuit-breaker analysis", *in Proc. 11th Int. Conf. on Gas Discharges and Their Applications*, 1995, Vol. I pp.342–345.

[52] S. Kwan, M. S. Chistodoulou, W. Hall and M. T. C. Fang, "The theoretical modeling of puffer circuit breakers", *in Proc. 11th Int. Conf. on Gas Discharges and Their Appellations*, 1995, Vol. I, pp.374–377.

[53] K. Y. Park, Y. J. Shin and K. D. Song and M. T. C. Fang, "Hybrid arc modeling of SF_6 puffer circuit breakers", *in Proc. 11th Int. Conf. on Gas Discharges and Their Applications*, 1995, Vol. I, pp.386–389.

[54] J. Vertite, T. Boucher, A. Comte, C. Delalondre and O. Simonin, "Turbulence models and flows in SF_6 circuit-breaker", *Proc. 11th Int. Conf. on Gas Discharges and Their Applications*, 1995, Vol. I, pp.406–409.

[55] L. Z. Tong, Q. P. Wang and E. Z. Wang, "Investigation of the dielectric recovery characteristics of SF_6 circuit breaker", *in Proc. 11th Int. Conf. on Gas Discharges and Their Applications*, 1995, Vol. I, pp.414–417.

[56] R. E. Blundell and M. T. C. Fang, "The similarity and scaling of radiating arcs burning in a turbulent, axially accelerating gas flow", *J. Phys. D: Appl. Phys.*, Vol. 30, pp.628–635, 1997.

[57] M. I. Boulos, P. Fauchais and E. Pfender, *Thermal Plasmas, Fundamentals and Applications, Vol.1*. New York : Plenum, 1994, p.252.

[58] K. P. Brand and J. Kopainsky, "Particle Densities in a decaying SF_6 plasma", *Appl. Phys.*, Vol. 16, pp.425–432, 1978.

[59] A. Gleizes, F. Mbolidi, M. Razafinimanana, S. Vacquie and D. Gravelle, "Cooling and chemical kinetics in a wall stabilized SF_6 arc in extinction", *J. Phys. D: Appl. Phys.*, Vol. 24, pp.1333–1338, 1991.

[60] A. Gleizes, F. Mbolidi and A. A. M. Habib, "Kinetic model of a decaying SF_6 plasma over the temperature range 12 000 K to 3000 K", *Plasma Sources Sci. Technol.*, Vol. 2, pp.173–179, 1993.

[61] J. J. Gonzalez, A. Gleizes and P. Krenek, "SF_6 circuit breaker arc modelling : influence of the electric field on the electrical conductivity", *J. Phys. D: Appl. Phys.*, Vol. 27, pp.985–993, 1994.

[62] G. Cliteur, M. Ishikawa and H. Takahashi, "Determination of the thermal inertia time constant of an SF_6 arc by measurement and theory", *in Proc. 11th Int. Conf. on Gas Discharges and Their Applications*, 1995, Vol. I, pp.22–25.

[63] A. Gleizes, E. Borge, A. M. Casanovas and B. Belmadani, "Kinetic model of a decaying SF_6 arc plasma in the pressure of impurities", *in Proc. 11th Int. Conf. on Gas Discharges and Their Applications*, 1995, Vol. I, pp. 50–53.

[64] L. Adamec, M. Bartlova and O. Coufal, "Relaxation of chemical equilibrium in SF_6-arc plasma", *in Proc. 12th Symposium on Phys. Switching Arc*, 1996, Vol. I, pp.5–8.

[65] M. Bartlova, "Reaction rate constants of electron-ion recombination in SF_6 arc plasma", *in Proc. 12th Symposium on Phys. Switching Arc*, 1996, pp.13–15.

[66] J. J. Gonzalez, J. B. Belhaouari and A. Gleizes, "Kinetic study of a decaying SF_6 arc plasma", *in Proc. 12th Symp. Phys. Switching Arc*, 1996, pp.45–48.

[67] L. Adamec and O. Coufal, "Comments on the computation of the composition of quenching media in HV circuit breakers after current zero", *J. Phys. D: Appl. Phys.*, Vol. 30, pp.1646–1652, 1997

[68] Y. Tanaka, Y. Yokomizu, T. Matsumura and Y. Kito, "Transient behavior of axial temperature distribution in post-arc channel after current zero around nozzle throat in flat-type SF_6 gas-blast quenching chamber", *J. Phys. D: Appl. Phys.*, Vol. 28, pp.2095–2103, 1995.

[69] Y. Tanaka, Y. Yokomizu, T. Matsumura and Y. Kito, "Transient distributions of arc temperature and its electrical resistivity along nozzle throat axis around current zero in a flat-type SF_6 gas-blast quenching chamber", *in Proc. 11th Int. Conf. on Gas Discharges and Their Applications*, 1995, Vol. I, pp.42–45.

[70] Y. Tanaka, M. Ishikawa, Y. Yokomizu, and T. Matsumura, "Dominant spectra of background radiation in an SF_6 post-arc channel", *IEEE Trans. Plasma Sci.*, Vol.25, pp.986–990, 1997.

[71] Y. Tanaka, Y. Yokomizu, T. Matsumura and Y. Kito, "Transient distribution of metallic vapor concentration in post-arc channel after current zero along nozzle axis in a flat-type SF_6 gas-blast quenching chamber", *J. Phys. D: Appl. Phys.*, Vol. 29, pp.1540–1550, 1996.

[72] Y. Tanaka, Y. Yokomizu, T. Matsumura and Y. Kito, "Diagnosis of temperature and metallic vapor concentration in post-arc at nozzle throat in flat-type SF_6 gas-blast quenching chamber", *in Proc. 7th Annual Conf. Power & Energy Society IEE Japan*, 1996, pp.345–350.

[73] Y. Tanaka, Y. Yokomizu, T. Matsumura and Y. Kito, "The opening process of thermal plasma contacts in a post-arc channel after current zero in a flat-type SF_6 gas-blast quenching chamber", *J. Phys. D: Appl. Phys.*, Vol. 30, pp.407–416, 1997.

[74] Y. Tanaka, Y. Yokomizu, T. Matsumura and Y. Kito, "Opening process of fictitious contacts made of thermal plasma after current zero in a flat-type SF_6 gas-blast quenching chamber", *IEE Japan*, Vol. 116-B, pp.1204–1211, 1996 (in Japanese).

[75] Y. Tanaka, Y. Yokomizu, M. Ishikawa and T. Matsumura, "Particle composition of high-pressure SF_6 plasma with electron temperature greater than gas temperature", *IEEE Trans. Plasma Sci.*, Vol.25, pp.991–995, 1997.

[76] Y. Tanaka, Y. Yokomizu, T. Matsubara and T. Matsumura, "Particle composition of two-temperature SF_6 plasma in pressure range from 0.1 to 1 MPa", *in Proc. 12th Int. Conf. on Gas Discharges and Their Applications*, 1997, Vol.2, pp.566–569.

Chapter 2 Transient behavior of axial temperature distribution in an SF_6 post-arc channel

2.1 Introduction

In an SF_6 gas-blast circuit breaker, an ac arc discharge between the electrodes is extinguished at current zero following a peak current of several thousands of amperes. After current zero, a post-arc with temperatures below about 6000 K still remains between the electrodes. Diagnosis of the post-arc in the transient state is therefore of great importance for understanding of the arc quenching process.

Arc temperature is considered to be one of the important factors for the arc quenching process. To estimate the temperature of the SF_6 gas blasted arc, a spectroscopic observation method is often adopted. In the spectroscopic method, spectral lines emitted from atoms and/or ions such as S, S^+ and F have frequently been observed [1]–[6]. However, observations have been performed only during peak current phases of a few hundreds of amperes or above.

As is well known, metallic vapor is injected into the arc from the electrodes in the arc interruption process [7]–[11]. For example, by observing spectral lines emitted from Cu in the SF_6 gas arc between copper electrodes, Lewis *et al.* estimated the arc temperature at a few micro-seconds before current zero [9].

The radiation intensities of the above-mentioned spectral lines are extremely low in the post-arc channel after current zero and thus are scarcely detectable even with high sensitive photomultiplier tubes. This is because the temperature of the post-arc decays to magnitudes below 6000 K and then the radiation intensities of the spectral lines reduced markedly. Consequently, a good deal of research work has been centered on ways to measure the temperature of the post-arc channel after current zero.

In this chapter, the author describes decaying behavior of temperature of a post-arc channel after current zero around nozzle throat in a flat-type SF_6 gas-blast quenching chamber with iron electrodes. The temperature was determined from the radiation intensities of the spectral lines of Fe originating from the iron electrodes. Firstly, theoretical calculations were made of the emission coefficients of 132 main spectral lines for Fe in the wavelength range of 400.0 to 700.0 nm. The emission coefficients of particles concerning S^+, F and Cu were also calculated. From these calculation results, the author found that several spectral lines radiated from Fe have higher emission coefficients than those radiated from S^+ or Cu at temperatures below 5000 K. Two Fe spectral lines at wavelengths 426.0 and 442.7 nm were selected from the 132 lines to estimate the post-arc temperature by means of the two-line method. Secondly, experiments were performed concerning the post-arc in a flat-type SF_6 gas blast quenching chamber. In these experiments, the two Fe spectral lines were observed at each of five axial positions around the nozzle throat. The radiation intensities of the Fe spectral lines were successfully detected with photomultiplier tubes up to an elapsed time of 100 μs after current zero. Finally, from the detected radiation intensities, transient distributions of temperature in the post-arc channel along the nozzle axis were estimated. From the results, the post-arc temperature at the nozzle throat was found to decrease markedly after current zero, becoming much lower than temperatures at the other axial positions.

2.2 Calculation of emission coefficients of Fe spectral lines

It is widely known that iron has many bright spectral lines. Therefore, it might be expected that there are several of these spectral lines having high intensity even in SF_6 post-arc channel with temperature below 6000 K, and that they can be utilized for the estimation of post-arc temperature. Then, the author calculates emission coefficients of many Fe spectral lines in SF_6-Fe mixture and investigate whether Fe spectral lines can be

used for estimation of post-arc temperature or not.

2.2.1 Equilibrium composition of SF_6-Fe mixture

Calculation of emission coefficients requires the number density data. However, the calculation result of SF_6-Fe mixture composition can hardly be found in the open literatures. Thus, considering the molecular, atomic and ionized species SF_6, SF_4, SF_2, F_2, S_2, F, S, F^+, S^+, F^{2+}, S^{2+}, F^-, S^-, Fe, Fe^+, Fe^{2+} and the electron, the author computed the equilibrium composition by solving simultaneous equations : Guldberg-Waage's equations for dissociation reactions, Saha's equations for ionization reactions, the charge neutrality equations, Dalton's law of partial pressures and iron vapor concentration. In this dissertation, the iron vapor concentration X_{Fe} in percentage was defined as the ratio of the sum of mass of Fe, Fe^+ and Fe^{2+} to the sum of those of all heavy species as follows :

$$X_{\mathrm{Fe}} = \frac{m_{\mathrm{Fe}}(N_{\mathrm{Fe}}(T) + N_{\mathrm{Fe}^+}(T) + N_{\mathrm{Fe}^{2+}}(T))}{\sum_j m_j N_j(T)} \times 100, \tag{2.1}$$

where $N_j(T)$ is the number density of species j, m_j is the mass of species j. Figure 2.1 shows the calculated particle composition in the temperature range of 3000–8000 K at a pressure of 0.1 MPa. The iron vapor concentration X_{Fe} is taken to be 0.01%.

Recently, Chervy *et al.* have computed the equilibrium composition of high-temperature SF_6 gas, taking account of more molecules : SF_5, SF_3, SSF_2, FSSF, F_2^+, S_2^+, SF and SF^- [12]. The composition for a pure SF_6 gas calculated by the author is in general agreement with that by Chervy *et al.* , although these molecules were neglected in the present calculation. This is because the number densities of the above molecules SF_5, SF_3, SSF_2, FSSF, F_2^+, S_2^+ and SF^- are very much lower than those of the other particles at temperatures above 3000 K.

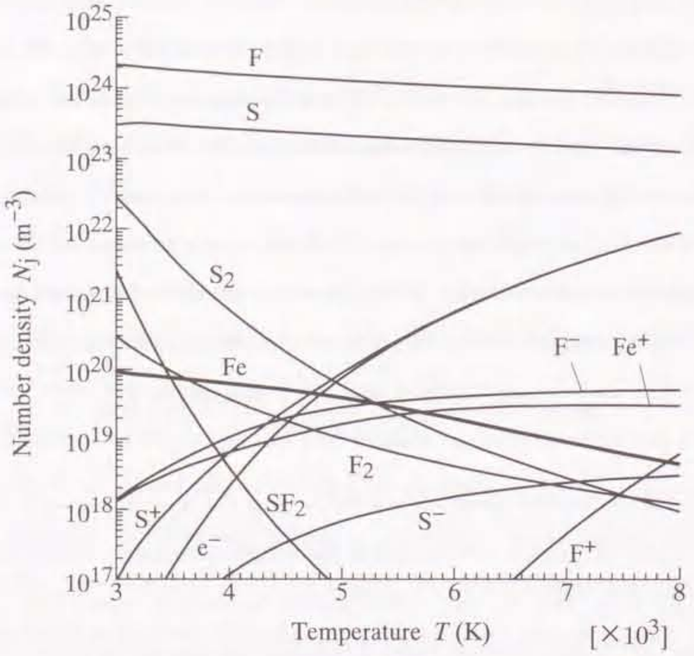

Figure 2.1. Equilibrium composition of 99.99% SF_6– 0.01% Fe mixture at a pressure of 0.1 MPa : bold curve, number density of Fe.

2.2.2 Method for calculating emission coefficient of Fe spectral line

The emission coefficient ε_{nm} of the Fe spectral line as a function of temperature T is expressed by

$$\varepsilon_{nm} = \frac{hc}{4\pi\lambda_{nm}} g_n A_{nm} \frac{N_{\mathrm{Fe}}(T)}{U_{\mathrm{Fe}}(T)} \exp\left(-\frac{E_n}{kT}\right) \quad [\mathrm{W\ m^{-3}sr^{-1}}], \tag{2.2}$$

where $U_{\mathrm{Fe}}(T)$ is the internal partition function of Fe, the subscripts n and m refer to the upper and lower energy levels respectively, g_n is the statistical weight for the upper energy level n, A_{nm} is the transition probability, λ_{nm} is the wavelength of the spectral line, E_n is the energy of the upper level n , and h, c and k are Planck's constant, the velocity of light and Boltzmann's constant, respectively [13, 14]. The calculation of the emission coefficient ε_{nm} from equation (2.2) requires numerical data for $N_{\mathrm{Fe}}(T)$, $U_{\mathrm{Fe}}(T)$, g_n, A_{nm} and λ_{nm}. The numerical data were obtained in the following ways.

(1) **Number density $N_{\mathrm{Fe}}(T)$.** The number density $N_{\mathrm{Fe}}(T)$ has theoretically been obtained as seen in Fig. 2.1. In this figure, the number density of the Fe was indicated by the bold curve.

(2) **Internal partition function $U_{\mathrm{Fe}}(T)$.** The internal partition function of $U_{\mathrm{Fe}}(T)$ was calculated from the following expression [15]:

$$U_{\mathrm{Fe}}(T) = \sum (2J+1) \exp\left(-\frac{E_l}{kT}\right), \tag{2.3}$$

where J is the quantum number of the energy level of the Fe, and E_l is the corresponding energy level of excited states. The values of J and E_l are given by Moore [16].

(3) **Atomic constants g_n, A_{nm}, λ_{nm} and E_n.** The values of g_n, A_{nm}, λ_{nm} and E_n with respect to each of the Fe spectral lines are experimantally given by Fuhr *et al.* [17] and Bridges and Kornblith [18].

Table 2.1. Emission constants for Fe spectral lines at wavelengths of 426, 430, 433, 438, 440, 442 and 443nm.

Wavelength	Upper energy level	gA-value	
λ_{nm}[nm]	E_n [eV]	$g_n A_{nm}[\times 10^8 \mathrm{s}^{-1}]$	
426.047	5.3085	3.52	[17]
430.790	4.4367	3.06	[17]
432.576	4.4732	3.5	[17]
438.354	4.3124	5.50	[17]
440.475	4.3713	2.475	[17]
441.512	4.4153	0.833	[17]
442.731	2.8512	0.0108	[18]

2.2.3 Calculation results of emission coefficients of Fe spectral lines

Corliss and Bozman show that Fe emits usually 132 main spectral lines in the wavelength range from 400.0 to 700.0 nm [19]. For each of these 132 spectral lines, the author calculated the emission coefficients in the temperature range of 3000–8000 K by substituting the data for $N_{\mathrm{Fe}}(T)$, g_n, A_{nm}, λ_{nm} and E_n into equation (2.2). The calculation results revealed that the spectral lines at wavelengths of 426.0, 430.8, 432.6, 438.4, 440.5, 441.5 and 442.7 nm have much higher emission coefficients than those at the other wavelengths at temperature 4000 K. Table 2.1 summarizes the atomic constants g_n, A_{nm}, λ_{nm} and E_n for the seven spectral lines. Figure 2.2 shows the calculated emission coefficients $\varepsilon_{\mathrm{Fe426}}$, $\varepsilon_{\mathrm{Fe431}}$, $\varepsilon_{\mathrm{Fe433}}$, $\varepsilon_{\mathrm{Fe438}}$, $\varepsilon_{\mathrm{Fe440}}$, $\varepsilon_{\mathrm{Fe442}}$ and $\varepsilon_{\mathrm{Fe443}}$ of the seven spectral lines as a function of

temperature at an iron vapor concentration X_{Fe} of 0.01%.

In a similar way, the emission coefficients $\varepsilon_{\mathrm{Cu511}}$, $\varepsilon_{\mathrm{Cu515}}$ and $\varepsilon_{\mathrm{Cu529}}$ of Cu spectral lines at wavelengths of 510.6, 515.3 and 529.3 nm were also calculated in the case of a copper vapor concentration X_{Cu} of 0.01%, in order to permit a comparison with those of the Fe spectral lines. These Cu spectral lines have habitually been observed to measure the temperature of the arc between the copper electrodes [9]–[11]. The author also calculated emission coefficients $\varepsilon_{\mathrm{S+532}}$ and $\varepsilon_{\mathrm{S+545}}$ of S^+ spectral lines at wavelengths of 532.1 and 545.4 nm and $\varepsilon_{\mathrm{F624}}$ of a F spectral line at 623.9 nm. These spectral lines of F and S^+ have frequently been measured to determine the temperature of the SF_6 gas arc during peak current phases [1]–[6]. Figure 2.2 also indicates $\varepsilon_{\mathrm{Cu511}}$, $\varepsilon_{\mathrm{Cu515}}$, $\varepsilon_{\mathrm{Cu529}}$, $\varepsilon_{\mathrm{S+532}}$, $\varepsilon_{\mathrm{S+545}}$ and $\varepsilon_{\mathrm{F624}}$ as a function of temperature.

From the data thus obtained it is possible to compare the emission coefficients of the seven Fe spectral lines with those of the F and S^+ spectral lines. As can be seen in Fig. 2.2, the emission coefficients of the F and S^+ are much lower than those of the Fe. For example, the emission coefficient $\varepsilon_{\mathrm{F624}}$ has a magnitude of 8.5×10^{-4} W m^{-3} sr^{-1} at 5000 K, and $\varepsilon_{\mathrm{S+532}}$ and $\varepsilon_{\mathrm{S+545}}$ attain magnitudes of less than 3.5×10^{-8} W m^{-3} sr^{-1} at 5000 K.

Next compare Fe spectral lines with those of Cu. It can be verified from Fig. 2.2 that the seven Fe spectral lines have much higher emission coefficients than the Cu spectral lines at 515.3 and 529.3 nm at temperatures below 5000 K. For example, at 4000 K $\varepsilon_{\mathrm{Cu515}}$ and $\varepsilon_{\mathrm{Cu529}}$ are 3.1 and 1.2×10^{-2} W m^{-3} sr^{-1}, respectively. In contrast, $\varepsilon_{\mathrm{Fe443}}$ is 2.5×10^{1}W m^{-3} sr^{-1} at 4000 K. That is, this emission coefficient $\varepsilon_{\mathrm{Fe443}}$ is eight times as high as $\varepsilon_{\mathrm{Cu515}}$.

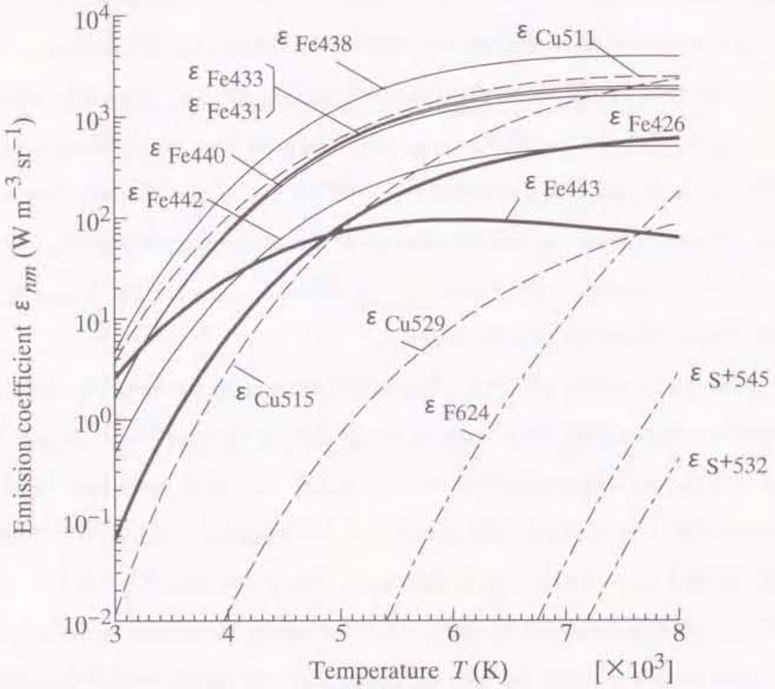

Figure 2.2. Emission coefficients of spectral lines emitted from various species for a 99.99% SF_6–0.01% metallic vapor mixture at a pressure of 0.1 MPa as a function of temperature. : full curves, Fe spectral lines ; broken curves, Cu spectral lines ; chain curves, S^+ and F spectral lines.

2.2.4 Selection of spectral lines suitable for determination of post-arc temperature

The two-line method is frequently used for determination of the arc temperature from the ratio of radiation intensities of two spectral lines at different wavelengths [4, 5, 20]. By rewriting equation (2.2) for the two cases ε_1 and ε_2, the following equation can be obtained :

$$\frac{\varepsilon_1}{\varepsilon_2} = \frac{g_1 A_1 \lambda_2}{g_2 A_2 \lambda_1} \exp\left(-\frac{E_1 - E_2}{kT}\right), \tag{2.4}$$

where subscripts 1 and 2 refer to the spectral lines at wavelengths λ_1 and λ_2, respectively. Solving equation (2.4) for T, we obtain

$$T = \frac{E_1 - E_2}{k\left(\ln\dfrac{g_1 A_1 \lambda_2}{g_2 A_2 \lambda_1} - \ln\dfrac{\varepsilon_1}{\varepsilon_2}\right)}. \tag{2.5}$$

Equation (2.5) demonstrates that measurement of the radiation intensities of two spectral lines at different wavelengths λ_1 and λ_2 enables us to determine the arc temperature T without any knowledge of the number density and internal partition function of the Fe.

In order to easily detect the radiation intensities of two Fe spectral lines after current zero and to determine arc temperature with high accuracy by the two-line method, two suitable Fe spectral lines need to be selected from among the 132 lines. The following four criteria were then taken to select the two suitable spectral lines.

(i) The two spectral lines should have high emission coefficients at temperatures below 6000 K. This is in order to allow the radiation intensities of spectral lines to be easily detectable even for the post-arc after current zero.

(ii) The spectral lines should not be resonance lines. The reason for this criterion is that a resonance line has a self-absorption function, the effect of which greatly reduces the radiation intensity emitted toward the outside of the arc. The measurement of the radiation intensity of a resonance line thus leads to a large error in the determination of the temperature.

(iii) The two spectral lines selected should display a sufficiently large difference between their upper energy levels. This is in order to permit higher accuracy in the determination of the temperature in the post-arc channel.

(iv) The two spectral lines should have emission coefficients of the same order at temperatures below 6000 K. In other words, the emission coefficient ratio of the two spectral lines should be in the range of 0.1–10 at such temperatures. This is to ensure that both the emission coefficients can easily be measured using detectors with the same sensitivity.

It now needs to be verified which two Fe spectral lines best satisfy the above four criteria.

(1) As described earlier, seven Fe spectral lines, at wavelengths 426.0, 430.8, 432.6, 438.4, 440.5, 441.5 and 442.7 nm, have much greater emission coefficients than the remaining 125 lines at temperatures below 6000 K. Consequently, these seven spectral lines satisfy criterion (i). Therefore the discussion is limited to these seven spectral lines.

(2) None of the above seven spectral lines is a resonance line.

(3) Twenty-one pairs may be formed among the seven spectral lines. It may be noted from Table 2.1 that the pair of lines Fe_{426} and Fe_{443} has the largest difference of 2.45 eV in upper energy levels.

(4) Figure 2.3 shows the calculated ratio of ε_{Fe443} to ε_{Fe426} as a function of temperature. It can be seen that the ratio $\varepsilon_{Fe443}/\varepsilon_{Fe426}$ is in the range 0.1 to 10 for temperatures between 3500 and 8000 K. In other words, emission coefficients ε_{Fe443} and ε_{Fe426} in the temperature range 3500–8000 K can easily be observed using two detectors with the same sensitivities. Figure 2.3 also represents the emission coefficient ratio $\varepsilon_{Cu515}/\varepsilon_{Cu511}$ for the Cu spectral lines at wavelengths 510.6 and 515.3 nm. These

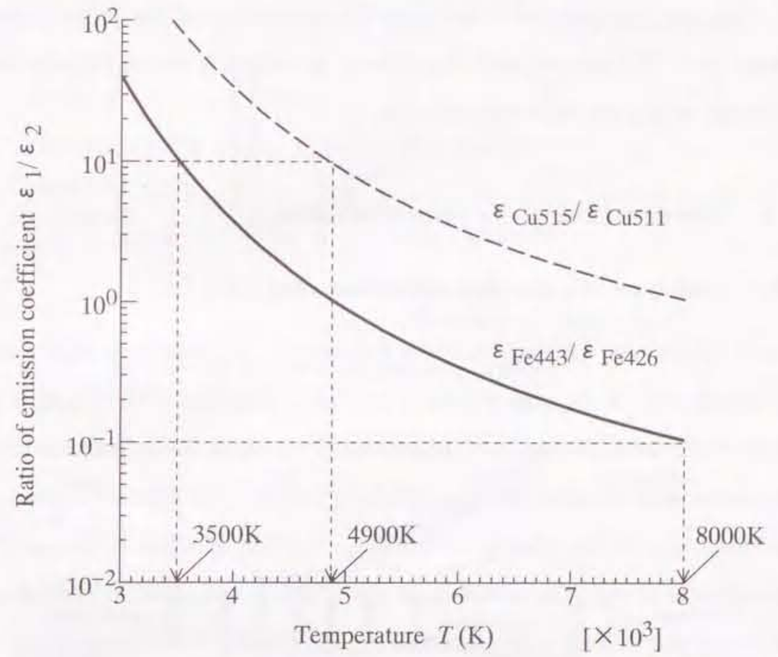

Figure 2.3. Ratios of emission coefficients of Fe spectral line and Cu spectral lines as a function of temperature.

Cu spectral lines are frequently observed in order to determine the arc temperature by means of the two-line method [6, 10]. The intensity ratio far exceeds ten at temperatures below 4900 K.

As discussed above in points (1)–(4), the two spectral lines at wavelengths 426.0 and 442.7 nm were thus selected to determine the temperature of the post-arc channel after current zero. This two-line method enables us to determine the arc temperature without knowledge of the iron vapor concentration.

2.3 Observation of Fe spectral lines

2.3.1 Flat-type SF_6 gas-blast quenching chamber

Figure 2.4 presents a general view of a flat-type SF_6 gas-blast quenching chamber and the arrangement of the experimental apparatus. Adoption of the flat-type quenching chamber facilitates observation of the arc around the nozzle throat. Iron was intentionally used as the electrode material in the quenching chamber. The distance between electrodes was adjusted to 50 mm. The flat nozzle was made of polytetrafluoroethylene (PTFE) with a thickness of 10 mm. The nozzle throat was 10 mm in width and 10 mm in length. This flat nozzle was sandwiched between two ceramic plates. These ceramic plates are heat-resistant, mainly comprising SiO_2, Al_2O_3 and CaO.

The PTFE nozzle is ablated by the heat of the arc. However, the presence of PTFE vapor at concentrations below 80 % has little influence on the electron number density and the electrical conductivity of SF_6 plasma [21]. The electrical conductivity is one of the most important factors in the arc interruption phenomena. On the other hand, the ceramic plates are hardly ablated by the heat of the arc. This was confirmed by another spectroscopic observation. The observation result showed that little spectral lines from Si, Al, Ca and O were observed around current zero for 5 kA arcs.

Sulfur hexa-fluoride gas was supplied through tubes along the cathode to blow in the

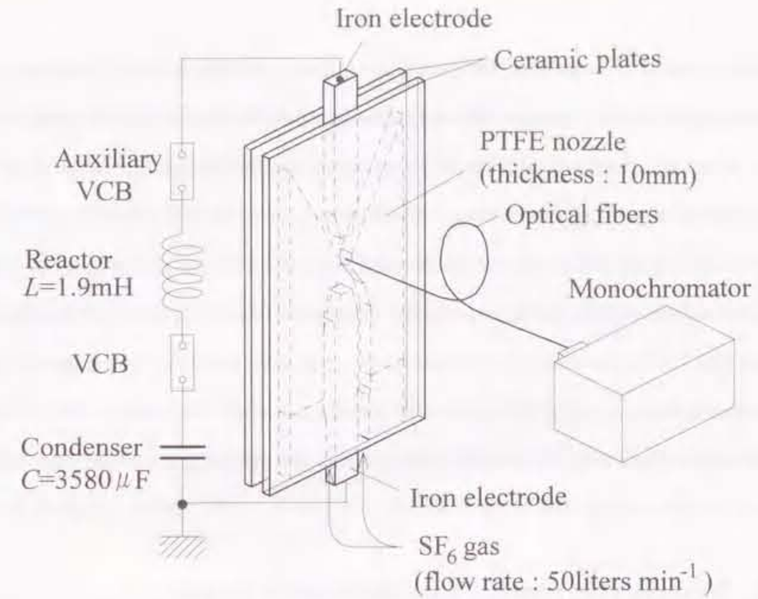

(a) Flat-type SF6 gas-blast quenching chamber

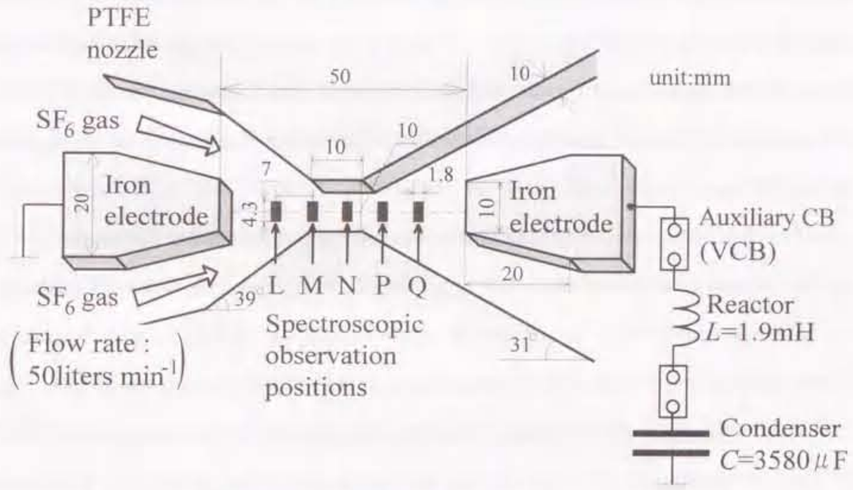

(b) Spectroscopic observation positions

Figure 2.4. Experimental arrangement

axial direction to the arc. The flow rate was adjusted to 50 liters min^{-1} before arc ignition. A damping sinusoidal current with a frequency of 60 Hz was supplied from a condenser bank (with capacitance C of 3580 μF) through a reactor (with inductance L of 1.9 mH). Peak value of the current was adjusted to 5 kA.

One of the purposes of this research work is to elucidate the decay process of the post-arc temperature in the free-recovery state after current zero. Hence, an auxiliary circuit breaker (VCB) was intentionally connected in series with the flat-type quenching chamber, interrupting the sinusoidal current at the first current zero. No transient recovery voltage (TRV) was applied between the electrodes, so that the temperature of the post-arc channel gradually decreased after current zero.

2.3.2 Spectroscopic observation around nozzle throat

Spectroscopic observation was carried out to measure the temperature of the post-arc channel after the current zero. The radiation from the arc was observed at five points along the nozzle axis at intervals of 7 mm. The five observation positions are shown by the symbols L, M, N, P and Q in Fig. 2.4(b). Observation position N corresponds to the nozzle throat.

At each of these observation positions, one of the ceramic plates sandwiching the flat nozzle has an almost rectangular hole 4 mm wide and 1 mm high. Through the hole, the arc radiation was observed by means of a bundle of four optical fibers made of quartz glass. These optical fibers are capable of transmitting light in the wavelength range from 200.0 to 1300.0 nm with little attenuation in radiation intensity. Each fiber has a core of diameter 0.8 mm, a cladding of diameter 1.0 mm and a numerical aperture of 0.2. The receiving ends of the fibers were located at a distance of 6 mm from the arc chamber. Hence, the bundle of fibers detected arc radiation from a region with spatial dimensions of 4.3 mm × 1.8 mm. Such optical fiber techniques are widely used in the plasma diagnosis [22]–[25].

Each bundle of fibers transmits the arc radiation from the observation point to the

entrance slit of a monochromator with a reciprocal dispersion of 0.8 nm mm^{-1}. An electromagnetic shutter was placed at the front of the entrance slit of the monochromator, to prevent intense arc radiation from entering the monochromator during peak current phase. A multi-channel detector with photomultiplier tubes was fitted on the focal plane at the exit of the monochromator. Use of this detector permits a simultaneous observation at three different wavelengths. The observation width of each channel corresponds to 0.6 nm in wavelength.

The time variations of the intensity signals were recorded with a digital wave-memory unit. The relative spectral sensitivity of the overall optical system was measured using a standard tungsten-halide lamp. Then, the calibration was carried out for above three signals.

As mentioned in section 2.2.4, Fe_{426} and Fe_{443}-lines were selected to estimate the temperature of the post-arc channel after current zero. Therefore, the author observed the radiation intensities I'_{426} and I'_{443} in the wavelength ranges 426.0±0.3 nm and 442.7±0.3 nm respectively, by means of the multi-channel detector. The observed radiation intensities I'_{426} and I'_{443} include radiation intensity of background spectra. Therefore, the radiation intensity I_{455} was simultaneously observed in the wavelength range of 455.0 ± 0.3 nm. This wavelength range are free from overlapping line spectra of atoms and ions. Numerical subtraction of I_{455} from I'_{426} and I'_{443} yielded net radiation intensities I_{Fe426} and I_{Fe443}.

2.4 Measurement of temperature in post-arc channel

2.4.1 Decay process of temperature in post-arc channel

Figure 2.5 (a) shows a typical oscillogram of radiation intensities I'_{426}, I'_{443} and I_{455}. These intensities were measured around current zero at observation position P. It should be noted that these three radiation intensities could be detected up to the time of 100 μs

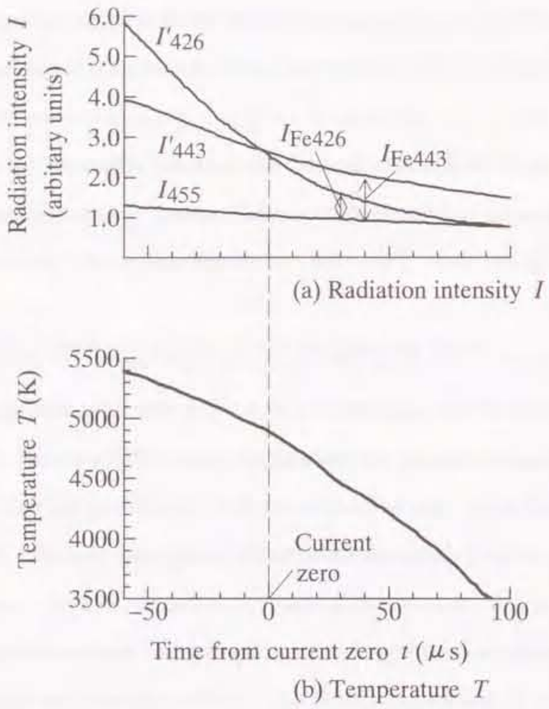

Figure 2.5. Decay process of radiation intensities and derived temperature T around current zero at observation position P in 5kA arcs.

after current zero. As mentioned above, numerical subtraction of I_{455} from I'_{426} and I'_{443} yielded the net radiation intensities I_{Fe426} and I_{Fe443}. From the net intensities I_{Fe426} and I_{Fe443}, the temperature was estimated using equation (2.5). Figure 2.5 (b) represents the decay process of the temperature thus estimated. As seen in this figure, the temperature was 4900 K at current zero. It can be seen that the temperature decreased gradually to reach 3500 K at 100 μs after current zero. This result demonstrates that it is possible through observation of the Fe spectral lines to measure the temperature of the post-arc channel after current zero. Such a low temperature of 3500 K has never been measured by the observation of the spectral lines emitted from other species such as sulfur ions or fluorine atoms.

2.4.2 Transient distribution of temperature along nozzle axis

At the same observation position, five measurements of the temperature were made just before and after current zero. From the five temperature measurements, an average temperature was numerically derived corresponding to each of a series of selected points of time. In this way, the decay process of the average temperatures was obtained at each of the observation positions L–Q along the nozzle axis. Figure 2.6 represents the axial distribution of the arc temperature around current zero. The time t from current zero is taken as a parameter. Each circle shows the average temperature obtained from five measurements. The temperature fluctuation among the five measurements was not more than 500 K at any time from -60 to 100 μs. In Fig. 2.6, the fluctuations appearing among the five measurements are indicated for the time of -60μs from current zero, as examples. From Fig. 2.6, the following features are apparent :

(1) During the period from -60 to 0 μs from current zero, the temperature distribution shows a local maximum value at the position N, i.e. at the nozzle throat. The curve of the axial distribution of temperature has the form of the letter W.

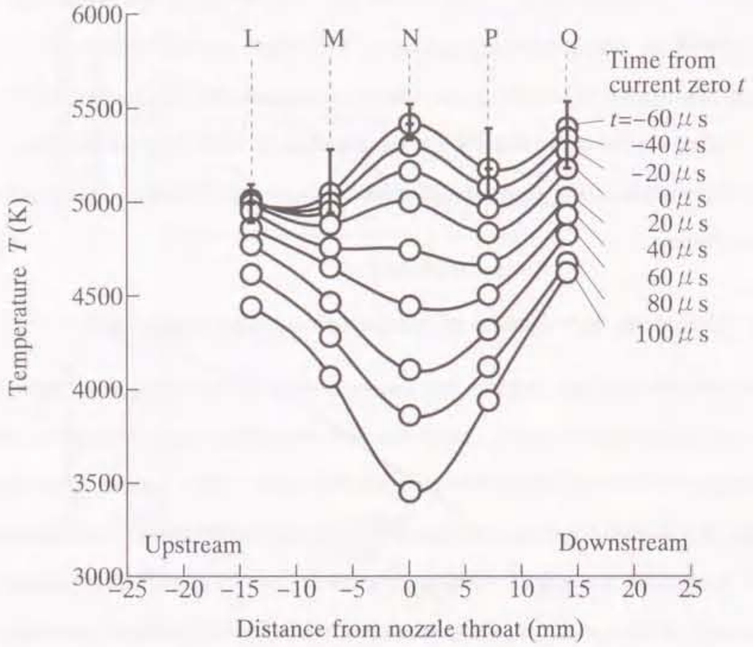

Figure 2.6. Transient axial distribution of arc temperature around current zero (peak value of current, 5kA ; SF_6 gas flow rate, 50 liters min^{-1}).

(2) However, it should be noted that the decay rate of the temperature is much higher at the nozzle throat N than at the other positions L, M, P and Q in the periods both before and after current zero.

(3) As a result, the temperature at the nozzle throat N drops to a lower magnitude than the temperatures at the other observation positions during the period from 40 to 100 μs after current zero. In this period, the curve of the axial distribution of temperature had the form of the letter U.

(4) At 100 μs after current zero, the temperature at the nozzle throat N becomes about 3500 K.

The results shown in Fig. 2.6 lead to the conclusion that the temperature at the nozzle throat decreases markedly with the passage of time in the period around current zero, becoming much lower in magnitude than at the other axial positions. This is one important point that requires emphasizing.

2.4.3 Energy loss estimation

Since it is considered that energy balance in a post-arc channel determines whether successful interruption is achieved or not, energy loss estimation is very significant for investigation of arc interruption process. Temperature variation in a post-arc channel is considered to follow a energy balance equation :

$$\rho_{\mathrm{m}} C_{\mathrm{p}} \frac{\partial T}{\partial t} = \frac{E^2}{\rho_{\mathrm{res}}} - P_{\mathrm{loss}} \tag{2.6}$$

where ρ_{m} is the mass density, C_{p} the specific heat at constant pressure, E the electric field strength, t the time, P_{loss} the energy loss including the losses due to radiation, convection and conduction.

Since no TRV is applied between the electrodes in the experiment as described previously, no electric field strength originates in a post-arc channel. In this case, equation

(2.6) can be rewritten into the following form for the time after current zero, i.e. by setting E=0,

$$P_{\text{loss}} = -\rho_{\text{m}} C_{\text{p}} \frac{\partial T}{\partial t} \tag{2.7}$$

If temperature decay rate $\partial T/\partial t$ and heat capacity $\rho_{\text{m}} C_{\text{p}}$ at constant pressure per unit volume are given, P_{loss} can be estimated through equation (2.7). The quantities $\partial T/\partial t$ and $\rho_{\text{m}} C_{\text{p}}$ were obtained as follows :

(1) **Temperature decay rate $\partial T/\partial t$.** Figure 2.7 shows temperature decays obtained at each of observation positions in the flat-type SF_6 gas-blast quenching chamber. These correspond to the evolution in Fig. 2.6. It is noted that the temperature decays are almost in proportion to the time. For example, $\partial T/\partial t$ can be estimated to be -15.5 K μs^{-1} at position N by method of least squares.

(2) **Heat capacity $\rho_{\text{m}} C_{\text{p}}$.** Frost and Liebermann have computed mass density ρ_{m} and enthalpy of pure SF_6 gas at a pressure of 0.1 MPa [26]. From these data, $\rho_{\text{m}} C_{\text{p}}$ was calculated. Figure 2.8 shows the theoretical data of $\rho_{\text{m}} C_{\text{p}}$ for pure SF_6 at a pressure of 0.1 MPa as a function of temperature. The quantity $\rho_{\text{m}} C_{\text{p}}$ rises with decreasing temperature. It is known that $\rho_{\text{m}} C_{\text{p}}$ is hardly influenced by iron vapor concentration less than 1%. As seen in later chapter, iron vapor concentration around current zero is estimated to be of the order of 0.01%.

Substitution of the obtained values $\partial T/\partial t$ and $\rho_{\text{m}} C_{\text{p}}$ into equation (2.7) yielded the energy loss P_{loss}. Figure 2.9 represents the axial distribution of loss with time t after current zero as a parameter. At nozzle throat P_{loss} is 0.8 GW m^{-3} at $t = 0$ μs, while it is 2.8 GW m^{-3} at $t = 100$ μs. Energy loss P_{loss} declines with increasing axial distance from nozzle throat. At a distance of +14mm, i.e. at position P, P_{loss} is 0.35 GW m^{-3} which is 0.125 times as high as that at nozzle throat. The obtained value of energy loss is much lower than those in a practical circuit breaker, where it was calculated to be about

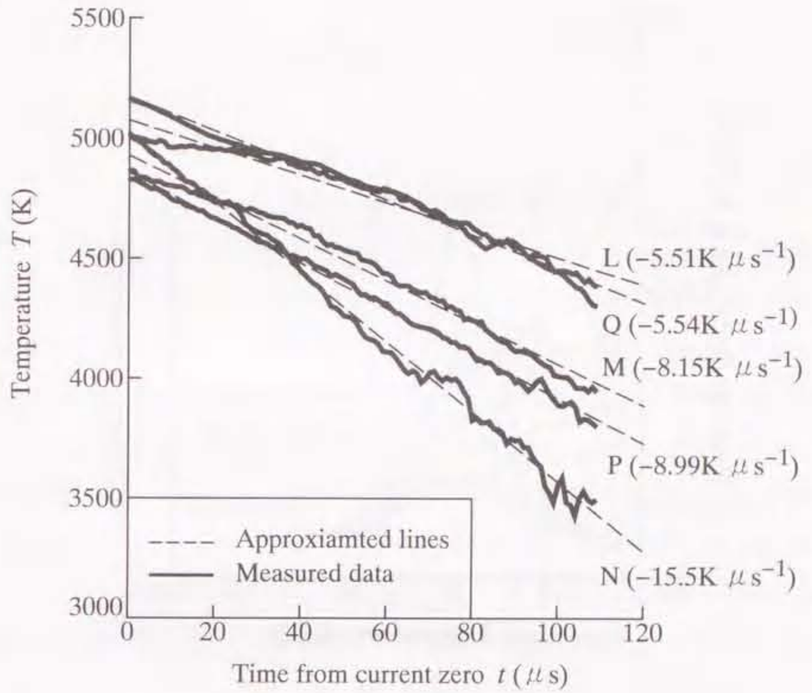

Figure 2.7. Time evolution of temperature in flat-type SF_6 gas-blast quenching chamber (peak value of current, 5kA ; SF_6 gas flow rate, 50 liters min^{-1}).

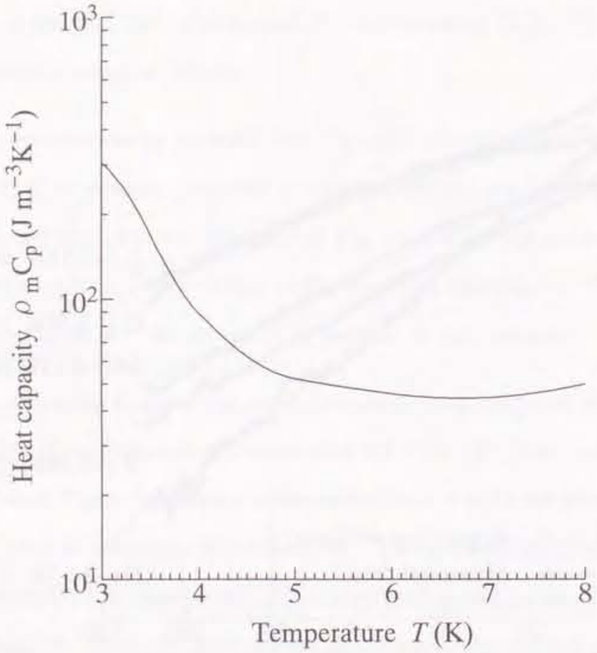

Figure 2.8. Heat capacity $\rho_m C_p$ at constant pressure per unit volume of pure SF_6 as a function of temperature. Pressure is fixed at 0.1 MPa [26].

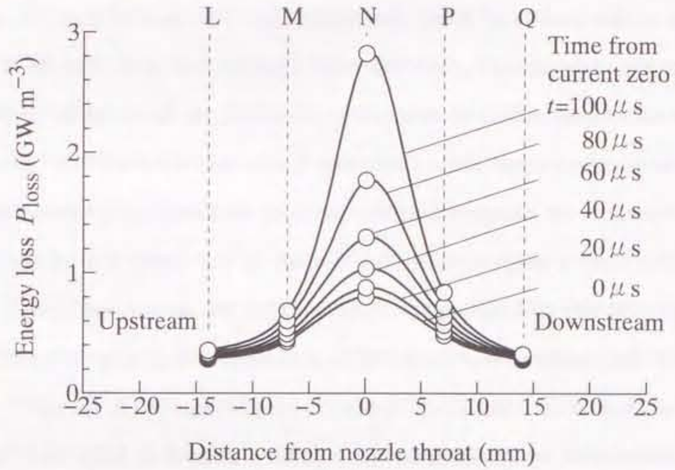

Figure 2.9. Axial distribution of energy loss after current zero (peak value of current : 5kA ; SF_6 gas flow rate : 50 liters min^{-1}).

7×10^2 GW m^{-3} at the center of an arc [27]. This low energy loss proves a low current interruption capacity of the flat chamber.

2.5 Discussion

2.5.1 Radiation intensity measured by means of a bundle of optical fibers

As described in section 2.3.2, a bundle of four optical fibers was intentionally arranged with a spatial resolution of 4.3 mm × 1.8 mm. While measuring the radiation intensity by means of this bundle of fibers, the author does not assume that the arc column is uniform in the observation region. The reason for the use of the bundle of fibers is that the arc radiation can always be detected by the fibers. It seems highly probable that the arc channel around current zero is very thin and is also distorted [28]. It follows that it cannot necessarily be assumed that the arc is to be found along the center axis of the nozzle. Therefore, a single optical fiber located on the center axis of the nozzle would have great difficulty in detecting the radiation from the arc around current zero. On the other hand, the bundle of four fibers will be successful in detecting the radiation from the arc channel, even if the channel shifts from the center axis of the nozzle.

The temperature estimated from the measured intensities I_{Fe426} and I_{Fe443} is almost equal to the highest temperature in the observation region, i.e. within the spatial resolution of 4.3 mm × 1.8 mm and the depth of 10 mm of the arc chamber. The detailed explanation is as follows. The measured radiation intensities I_{Fe426} and I_{Fe443} are integrated intensities over the whole observation region. On the assumption that the temperature distribution has a parabolic shape in a given cross-section of the arc, a calculation was made of the intensity integrated over the observation region. The calculation results show that the integrated intensity is almost equal to the intensity at the location with the highest temperature in the cross-section. This is because the emission coefficient of the Fe spectral line decreases drastically with a reduction of temperature in the range below

10 000K. From the calculation results, the difference between the highest temperature in the cross-section and the temperature derived from the integrated intensities was found to be below 10%. The above discussion leads to the conclusion that the measured intensities may be taken as an approximation of those existing at the point of the highest temperature in the observation region, and that the temperature estimated from these intensities corresponds to almost exactly the highest temperature in the observation region.

2.5.2 Estimated temperature

In the present investigation, the temperature was estimated from the radiation intensities of the Fe injected from the electrodes. Strictly speaking, the estimated temperature is the excitation temperature of the Fe on the assumption that the populations of excited states follow the Boltzmann distribution. However, the author regards the estimated temperature as representative of bulk arc temperatures. The reasons are as follows. Firstly, as is well known, local thermal equilibrium(LTE) is generally considered to obtain in the arc [20],[29]–[32]. This is mainly because the mean free path of the electron is small and the electric field strength of the arc is low. Moreover, in the present experiments, no transient recovery voltage was applied to the post-arc after the current zero, and thus the electric field strength of the arc was zero. In consequence, the temperature of each particle in the arc may be considered almost the same. Secondly, the temperatures for the metallic vapors injected from the electrodes are the same as those for gas species as explained below. Sakuta observed N_2^+ spectral lines and Cu spectral lines radiated from a wall stabilized air arc burning between copper electrodes, then estimated the temperature from the radiation intensities [33]. As a result, the temperature estimated from the radiation intensities of Cu spectral lines proved to be in good agreement with that estimated from N_2^+ spectra. For the above reasons, the author concludes that the iron vapor temperatures are representative of the bulk arc temperature.

2.5.3 Error in determining of arc temperature

2.5.3.1 Line broadening and shifting

In the present experiment, the spectral lines of Fe were observed with the multi-channel detector. The observation width of each channel corresponds to 0.6 nm in wavelength. This wavelength width of 0.6 nm is much greater than the broadening and shifting of the Fe spectral line caused by mechanisms such as Stark effect [34, 35]. Consequently, the errors of radiation intensities introduced by the broadening and shifting are negligible, and thus the errors of temperatures resulting from these mechanisms are also negligible.

2.5.3.2 Uncertainty in transition probability

The uncertainties of the transition probabilities of the two spectral lines causes the uncertainty in temperature in determination by the two-line method. The relative uncertainty $\Delta T/T$ in temperature is given by the following expression [36] :

$$\frac{\Delta T}{T} = \left(\frac{\Delta A_{426}}{A_{426}} + \frac{\Delta A_{443}}{A_{443}}\right) \frac{kT}{E_{426} - E_{443}}, \tag{2.8}$$

where A is the transition probability, ΔA is the uncertainty of the transition probability, E is the upper energy level and k is Boltzmann's constant. The script numbers denote the wavelengths in nano-meters.

The transition probability for the Fe spectral line at 426.0 nm have an uncertainty $\Delta A_{426}/A_{426}$ of ± 25 % [17], whilst an uncertainty $\Delta A_{443}/A_{443}$ for Fe spectral line at 442.7 nm is ± 7.5 % [18]. Substituting the above values E_{426}=42816 cm^{-1}, E_{443}=22997 cm^{-1} and T into equation (2.8) yields the relative uncertainty $\Delta T/T$. For example, at a temperature 5000 K, $\Delta T/T$ is estimated to be ± 0.057 ($\Delta T = \pm 284$ K). The quantity $\Delta T/T$ increases linearly with T.

2.5.4 Temperature distribution along nozzle axis around current zero

As seen in Fig. 2.6, the temperature distribution along the nozzle axis shows a local maximum at the nozzle throat in the arcing period of -60 to 0 μs from current zero. This result can be explained as follows :

By solving simultaneously the mass conservation and the Navier-Stokes equations, the author calculated SF_6 gas flow velocity in a flat-type quenching chamber under conditions of absence of the arc. Figure 2.10 indicates the distribution of the calculated flow velocity along the nozzle axis. In this figure, the positions of spectroscopic observation are denoted by the symbols L, M, N, P and Q. As seen in Fig. 2.10, the velocity is greater at the nozzle throat N than at the other positions. This relation probably continues to hold good under conditions of the arc's presence around current zero.

Before current zero, the arc column is much thinner at the nozzle throat than at the other axial positions [37]. This seems to be mainly because the velocity of SF_6 gas flow is greater at the nozzle throat N than at the other axial positions. Therefore the arc has a higher current density at the nozzle throat than at the other positions. This drastically increases joule heating of the arc column at the nozzle throat, thus leading to the temperature rise of the arc at the nozzle throat.

On the other hand, after current zero the temperature becomes lower at the nozzle throat than at the other observation positions. This result can be interpreted as follows: in the experiment, no transient recovery voltage was applied between the electrodes after current zero, since the aim of the research is to elucidate the decay process of the temperature in the post-arc channel. Therefore, in the post-arc channel, there was no ohmic heating but only the energy loss. The energy loss may be assumed much higher at the nozzle throat than at the other axial positions. This is because the SF_6 gas flow velocity is highest at the nozzle throat, so that the convection loss is much greater than losses through conduction and radiation [37]. This causes the temperature at the nozzle throat

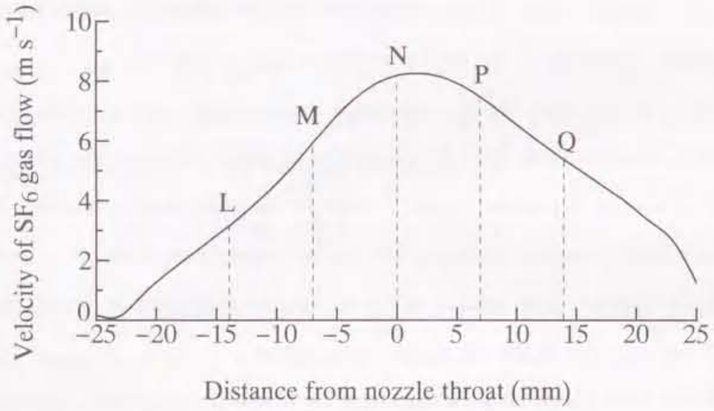

Figure 2.10. Velocity distribution of SF_6 gas flow along nozzle axis in flat-type SF_6 gas-blast quenching chamber under condition of absence of arc.

to decrease markedly.

2.5.5 Comparison of the experimental results with theoretical ones

Few experimental data on the arc temperature around current zero have been reported in the open literature. However, recent papers have described theoretical calculation results for the arc temperature around current zero. For example, by solving three conservation equations of mass, momentum and energy, Ikeda *et al.* analyzed the axial distributions of the arc temperature before current zero in a puffer SF_6 gas circuit breaker [38]. This calculation result shows that the arc temperature was higher at the nozzle throat than at the other axial positions in the time period from 50 to 0.1 μs before current zero. Fang *et al.* also calculated the arc temperature distribution along the nozzle axis in the time periods both before and after current zero in a model gas circuit breaker [39]. Their work revealed that the temperature decreases more rapidly at the nozzle throat than at the other positions. The experimental result shown in Fig. 2.6 indicates the similar pattern to those calculated by Ikeda and Fang, although their calculation was intended for a practical circuit breaker.

In the experiment in this work, the author obtained the temperature decay rate of -15.5 K μ s^{-1} at position N in the chamber. On the other hand, Ikeda and Fang obtained those of the order of -10^3 K μs^{-1} from their calculation for the practical circuit breaker. This difference in the temperature decay rate may arise from much smaller flow rate and loss in the flat-chamber than the practical circuit breaker as shown in Fig. 2.9.

2.5.6 The lowest temperature determinable by the spectroscopic observation method

Many papers have appeared reporting the temperatures of SF_6 gas-blasted arcs measured by means of spectroscopic observation methods [1]–[10]. For instance, by observing both a S^+ spectral line at the wavelength of 545.4 nm and a F spectral line at 623.9 nm, Airey *et*

al. measured radial distributions of arc temperatures for an ac current with a peak value of 10kA by means of the two-line method [1]. In the radial distribution thus obtained, temperatures above 12 000 K in the arc central region were measured, while temperatures below 12 000 K in the periphery of the arc central region were no longer measurable. In other words, as Airey suggested, the lowest limit of measurable temperature is around 12 000 K in the case where temperature is estimated from the radiation intensities of S^+ and F spectral lines. He also explained the reason as follows : the radiation intensities of these spectral lines are quite low at temperatures below 12 000 K, thus being scarcely detectable even with a photomultiplier tube.

Leseberg and Pietsch also measured radial distributions of temperatures for an SF_6 gas arc with a current of 1800 A [3]. They observed two S^+ spectral lines at the wavelengths of 532.1 and 545.4 nm, and then determined the temperatures from the ratio of these two radiation intensities. As a result, the lowest limit of measurable temperature proved to be approximately 12 000 K.

The research work carried out by Lewis *et al.* is of great interest, because the spectroscopic observation for an SF_6 arc was made at a few micro-seconds before current zero with an optical multi-channel analyzer [9]. In the experiment, Cu spectral lines at the wavelengths of 510.6 and 515.3 nm emitted from the arc were observed in order to measure the arc temperature. Judging from the results shown in the paper, it appears that the lowest limit of measurable temperature for this spectroscopic observation is 7400 K.

On the other hand, as far as the experimental results shown in Fig. 2.6 are concerned, the lowest limit of measurable temperature is approximately 3500 K for the observation of Fe spectral lines. This is another point deserving emphasis. The observation of these Fe spectral lines also makes it possible to measure the temperature of the post-arc channel up until the time of 100 μs after current zero for a sinusoidal current with peak value of 5 kA. It is to be noted that experimental data on the decay process of the temperature in the post-arc channel after current zero have scarcely been published until now.

2.6 Conclusions

The experiment has elucidated the decay process of the temperature in the post-arc channel up to 100 μs after current zero using measurements taken at five axial positions around the nozzle throat in a flat-type SF_6 gas blast quenching chamber. In the experiment, peak value of current and SF_6 gas flow rate was adjusted to 5kA and 50 liters min^{-1}, respectively. At each of the five positions, the temperature was estimated from the radiation intensities of two Fe spectral lines at the wavelengths of 426.0 and 442.7 nm. Even after current zero, the Fe spectral lines proved to have high radiation intensities detectable with photomultiplier tubes. The experimental results showed that the post-arc temperature decayed markedly at the nozzle throat in comparison with temperatures at the other axial positions. As a result, at 40μs after current zero the temperature at the nozzle throat becomes the lowest in the arc, and then continues to decrease to about 3500 K at 100 μs.

Energy loss was estimated from the temperature decay rates experimentally obtained. It was found that the energy loss at the nozzle throat reached to 2.8 GW m^{-3} at 100μs after current zero. This value is much greater than those at the other axial positions. From these results, it was suggested that nozzle throat is essential for current interruption.

References

[1] D. R. Airey, P. H. Richards and J. D. Swift, "Time-resolved radial temperature profiles for 10kA SF_6 arcs", *J. Phys. D: Appl. Phys.*, Vol. 8, pp.1982–1993, 1975.

[2] D. R. Airey, "A rapid-scanning polychromator for time-resolved temperature and radius measurements in 40kA SF_6 arcs", *J. Phys. E: Sci. Instrum.*, Vol. 12, pp.397–402, 1979.

[3] D. Leseberg and G. Pietsch, "Optical investigations on a SF_6 switching arc inside a glass nozzle", *in Proc. 7th Int. Conf. on Gas Discharges and Their Applications*, 1982, pp 9–12.

[4] S. Vacquie, A. Gleizes and H. Kafrouni, "Measurements of electron density in a SF_6 arc plasma", *J. Phys. D: Appl. Phys.*, Vol. 18, pp.2193–2205, 1985.

[5] K-P, Hinz, "Optical diagnostics of SF_6 high-current discharges", *J. Phys.D: Appl. Phys.*, Vol. 19, pp.2381–2391, 1986.

[6] H. Ikeda, G. R. Jones, M. Irie and A. N. Prasad, "Spectroscopy of very high current , convection arcs", *in Proc. 9th Int. Conf. on Gas Discharges and Their Applications*, 1988, pp.5–8.

[7] Y. Kito, T. Sakuta and M. Kurono, "Decaying processes of temperature and copper vapour concentration toward current zero in alternative–current arc", *Trans. IEE of Japan*, Vol. 103, pp.125–126, 1983.

[8] G. R. Jones, W. Hu and S. M. El-Kholy, "A spectroscopic investigation of electrode material entrained into the extinguished arc of an SF_6 circuit breaker", *J. Phys. D: Appl. Phys.*, Vol. 21, pp.1414–1420, 1988.

[9] E. Lewis E, A. N. Prasad and G. R. Jones, "Current zero spectroscopy of a high power SF_6 circuit breaker arc", *in Proc. 8th Int. Conf. on Gas Discharges and Their Applications*, 1985, pp.31–34.

[10] S. M. El-Kholy, G. R. Jones and E. Lewis, "Evaluation of the spectra of decaying arcs in gas blast circuit breakers", *in Proc. 9th Int. Conf. on Gas Discharges and Their Applications*, pp.43–46, 1988.

[11] G. R. Jones, *High pressure arcs in industrial devices, Diagnostic and monitoring techniques.* Cambridge. Cambridge University Press, 1988, p.167.

[12] B. Chervy, A. Gleizes and M. Razafinimanana, "Thermodynamic properties and transport coefficients in SF_6-Cu mixtures at temperatures of 300–30 000 K and pressures of 0.1–1 MPa", *J. Phys. D: Appl. Phys.*, Vol. 27, pp.1193–206, 1994.

[13] G.R. Jones, *High pressure arcs in industrial devices, Diagnostic and monitoring techniques.* Cambridge : Cambridge University Press, 1988, p.158.

[14] M. I. Boulos, P. Fauchais and E. Pfender, *Thermal Plasmas, Fundamentals and Applications, Vol. 1.* New York : Plenum, 1994, p.345.

[15] M. I. Boulos, P. Fauchais and E. Pfender, *Thermal Plasmas, Fundamentals and Applications, Vol. 1.* New York : Plenum, 1994, p.23.

[16] C. E. Moore *Atomic energy levels Volume II.* Washington DC :NBS, 1952, pp.49–54.

[17] J. R. Fuhr, G. A. Martin and W. L. Wiese, *Atomic Transition Probabilities Iron through Nickel Vol. 17, Suppl.4.* Maryland : NBS, 1988.

[18] J. M. Bridges and R. L. Kornblith, "Arc measurements of Fe I oscillator strengths", *Astrophys. J.*, Vol. 192, pp.793–812, 1974.

[19] C. H. Corliss and W. R. Bozman, *Experimental Transition Probabilities for Spectral Lines of Seventy Elements.* Washington DC : NBS, 1962 pp.95–108.

[20] W. J. Pearce, *Plasma-Jet Temperature Measurement* ed. P. J. Dickerman. Chicago : The University of Chicago, 1961, pp.125–167.

[21] T. Sakuta , S. Terauchi , T. Takashima and M. Ishikawa, "Transport properties of high temperature SF_6 gas contaminated with Cu and PTFE vapor at high pressure condition", *Trans. of IEE of Japan*, Vol. 113–B, pp.342–350, 1993 (in Japanese).

[22] S. M. G. Ali, H. M. Ryan, D. Lightle, D. W. Shimmin, S. Tayloy and G. R. Jones, "High power short circuit studies on a commercial 420 kV 60 kA puffer circuit breaker", *IEEE Trans. Power Appar. Syst.*, **104**, pp.459–467, 1985.

[23] G. R. Jones, *High Pressure Arcs in Industrial Devices, Diagnostic and Monitoring Techniques.* Cambridge : Cambridge University Press, 1988, p.141.

[24] D. W. Shimmin and G. R. Jones, "Arc radiation monitoring in a commercial EHV circuit breaker using optical fiber transmission", *J. Phys. D: Appl. Phys.*, Vol. 21, pp.731–743, 1988.

[25] G. R. Jones, "Electric arc monitoring utilising intelligent optical fibre systems", *in Proc. Int. Conf. on Gas Discharges and Their Applications*, 1995, Vol. II, pp.504–512.

[26] L. S. Frost and R. W. Liebermann, "Composition and transport properties of SF_6 and their use in a simplified enthalpy flow arc model", *Proc. IEEE*, Vol. 59, pp.474–485, 1971.

[27] R. E. Kinsinger, "Numerical model for current-zero arc interruption processes", *IEEE Trans Power Appar. Syst.*, Vol. 93, pp.1143–1149, 1974.

[28] W. Hermann, U. Kogelschatz, L. Niemeyer, K. Ragaller and E. Schade, Investigation on the physical phenomena around current zero in HV gas blast breakers", *IEEE Trans. Power Appar. Syst.*, Vol. 95, pp.1165–1176, 1976.

[29] S. Flügge, *Handbuch der Physik, Vol.22*. Berlin : Springer, 1956, p.307.

[30] W. Lochte-Holtgreven, *Plasma Diagnostics*. Amsterdam : North-Holl, 1968, pp.146–147.

[31] H. R. Griem, *Plasma Spectroscopy*. New York : McGraw-Hill, 1964, pp.129–131.

[32] M. F. Hoyaux, *Arc Physics*. New York : Springer, 1968, pp.34–35.

[33] T. Sakuta, Ph.D.Thesis, Nagoya University, Japan (in Japanese).

[34] C. W. Allen, *Astrophysical Quantities*. London : Athlone, 1955, pp.80–81.

[35] G. Herzberg, *Atomic Spectra and Atomic Structure*. New York : Dover, 1944, pp.114–118.

[36] F. Cabannes and J. Chapelle, *Reactions under Plasma Conditions*, Vol. 1, ed. Venugopalan. New York : Wiley–Interscience, 1971, ch. 7, p.396.

[37] W. Hermann, L. Niemeyer and E. Schade, "The transient behaviour of axially blown high pressure arcs", *in Proc. 3rd Int. Conf. on Gas Discharges and Their Applications*, 1974, pp.483–487.

[38] H. Ikeda, M. Ishikawa and S. Yanabu, "Analyses of axial energy distribution in decaying arc of SF_6 gas circuit breaker", *IEEE Trans. Plasma Sci.*, Vol. 14, pp.395–401, 1986

[39] M. T. C. Fang, Q. Zhuang and X. J. Guo, "Current-zero behaviour of an SF_6 gas-blast arc. Part II : turbulent flow", *J. Phys. D: Appl. Phys.*, Vol. 27, pp.74–83, 1994.

Chapter 3 Axial distribution of metallic vapor concentration in an SF_6 post-arc channel

3.1 Introduction

An arc discharge usually burns between two metallic electrodes in a circuit breaker during the high-current interruption process. As is widely known, metallic vapor is injected into the arc column from the electrodes [1]–[12]. The presence of much metallic vapor increases the number density of free electrons in an arc column. The increase in electron number density causes a marked enhancement of the electrical conductivity of the arc, resulting in a decrease in the interruption capability of the circuit breaker [12]. The diagnosis of the metallic vapor contamination is thus very important for an understanding of the arc condition.

Several papers have described experimental approaches to studying the arcs contaminated with metallic vapors [1]–[4]. In these experiments, spectroscopic observation techniques have often been performed to estimate the metallic vapor concentration or the number density of metallic particles in the arc column. Usually, both a spectral line emitted from the metallic vapor and that from a gas species have been observed. For example, for an a.c. 20 kA SF_6 gas arc burning between copper electrodes, Airey has measured the radiation intensities of Cu and S^+ spectra, finding that the copper vapor concentration reaches 40 % during high current phase [1, 2]. For a dc 30 A air arc burning between copper electrodes, Sakuta *et al.* have measured the radiation intensities of N_2^+ molecular spectra and a Cu spectrum to obtain the arc temperature and copper vapor

concentration [6]. Sakuta *et al.* concluded that the copper vapor concentration is about 0.5 %. For an ac 300 A air arc between copper electrodes, Kito *et al.* have measured the transient radial distribution of the copper vapor concentration up to 0.3 ms before current zero [7]. Kito *et al.* pointed out that copper vapor concentration at 0.3 ms before current zero reached to 0.02%.

However, there have been few research works on the measurement of the metallic vapor concentration in an SF_6 post-arc channel after current zero. This is mainly because the radiation intensities of spectral lines emitted from ions and atoms such as S^+, F or Cu are no longer detectable in the post-arc channel after current zero even with high sensitive photomultiplier tubes.

On the other hand, as stated in the previous chapter, the author measured the radiation intensities I_{Fe426} and I_{Fe443} of Fe spectral lines at wavelengths of 426.0 and 442.7 nm, as well as the radiation intensity I_{455} at 455.0 nm as background spectra. These spectroscopic measurement allowed the determination of the temperature of a post-arc channel up to 100 μs after current zero in the flat-type SF_6 gas-blast quenching chamber.

In this chapter, a novel method for estimating iron vapor concentration X_{Fe} in mass percentage from the radiation intensities of the above two Fe spectral lines and that of background spectra was developed. First, emission coefficient of background spectra at 455.0 nm was theoretically calculated for temperatures of 3000–6000 K considering continuous spectra as well as S_2 spectra. The calculated results reveal that continuous spectra dominates background at temperatures above 4000 K, while S_2 does at temperatures below 4000 K. Also, the emission coefficient of background spectra proved to agree with that obtained in the experiment in temperature dependence. Secondly, the developed method was applied to the post-arc after current zero. The method was capable of determining

X_{Fe} up to 100 μs after current zero. Finally, axial distribution of X_{Fe} around nozzle throat in the post-arc channel was estimated. As a consequence, it was found that X_{Fe} along nozzle axis maintained a magnitude around 1×10^{-2} % during the time around current zero.

3.2 Theoretical calculation of emission coefficients

3.2.1 Emission coefficient of background spectra

As described in the previous chapter, in order to estimate post-arc temperature, the author measured the radiation intensities in three wavelengths : two of which include Fe spectral lines and background spectra, and the other only background spectra. The author considers that the radiation intensity of background spectra is utilized for the estimation of iron vapor concentration. For the use of radiation intensity of background spectra, the detailed understanding of the characteristics of background spectra is required. Then, the emission coefficient of background spectra is calculated in this section.

3.2.1.1 Emission coefficient of continuous spectra

Background is usually considered to consist only of continuous spectra especially at temperatures above 6000 K. Further, the calculated result of emission coefficient of continuous spectra in temperature range below 6000 K can be rarely described in the open literature. Thus in this section, the emission coefficient of the continuous spectra is calculated for temperature range 3000–8000 K.

In general, continuous emission by plasma is due to the superimposition of several continuous spectra caused by different mechanisms. In this calculation, four radiative

mechanisms were taken into account : (1) recombination radiation, (2) radiation by electron attachment, (3) bremsstrahlung and (4) radiation by collision between electron and neutral species [13]–[15].

(1) **Recombination radiation.** Under thermal equilibrium conditions, the integrated emission coefficient $\varepsilon_{\mathrm{fb}}$ in W m^{-3} sr^{-1} due to recombination radiation in a wavelength range from λ to $\lambda+\Delta\lambda$ is given by

$$\varepsilon_{\mathrm{fb}} = C_1 \frac{N_{\mathrm{e}}(T)}{T^{\frac{1}{2}}} \left[1 - \exp\left(-\frac{hc}{kT\lambda}\right)\right] \sum_{j(\mathrm{ion})} \frac{g_{1j} Z_{\mathrm{eff}j}^2 N_j(T)}{U_j(T)} \xi_j(\lambda, T) \frac{c\Delta\lambda}{\lambda^2} \qquad (3.1)$$

$$C_1 = \frac{1}{(4\pi\varepsilon_0)^3} \frac{16\pi e^6}{3c^3 (6\pi m_{\mathrm{e}}^3 k)^{\frac{1}{2}}}$$

where T is the temperature, e the electronic charge, m_{e} the mass of an electron, h Planck's constant, c the velocity of light, k Boltzmann's constant, g_{1j} the statistical weight of the ground state of species j, and $U_j(T)$ the internal partition function of species j. The quantities $N_{\mathrm{e}}(T)$ and $N_j(T)$ are the number densities of the electron and the species j, respectively. $Z_{\mathrm{eff}j}$ is the effective ionic charge of the species j and $\xi_j(\lambda, T)$ is the Bibermann-Schlüter factor for non-hydrogenic particles [16]–[19].

To calculate equation (3.1), the author obtained numerical data concerning the above quantities in the following way. The numerical data on $N_{\mathrm{e}}(T)$ and $N_j(T)$ have been obtained in the previous chapter. The internal partition function $U_j(T)$ has also been already obtained in the calculation of equilibrium composition. The effective charge $Z_{\mathrm{eff}j}$ for an ionic particle was taken to be equal to its actual charge number [20]. The Bibermann-Schlüter factor $\xi_j(\lambda, T)$ was assumed to be 1.0 for SF_6, because $\xi_j(\lambda, T)$ is close to unity for most of particles in the wavelength range of 400.0–500.0 nm [16]–[19].

Since the radiation intensity of the continuous spectra within wavelength width of 455.0±0.3 nm were measured, the wavelength λ and wavelength width $\Delta\lambda$ are taken to be 455.0 nm and 0.6 nm respectively.

(2) **Radiation by electron attachment.** Electron attachment involves light emission with the integrated emission coefficient $\varepsilon_{\mathrm{attach}}$ given by

$$\varepsilon_{\mathrm{attach}} = \frac{2hc}{\lambda^3} \exp\left(-\frac{hc}{kT\lambda}\right) \sum_j N_j^-(T) \sigma_{\mathrm{det}j}^-(T) \frac{c\Delta\lambda}{\lambda^2}, \qquad (3.2)$$

where $N_j^-(T)$ is the number density of negative ion j, $\sigma_{\mathrm{det}j}^-(T)$ is the photo-detachment cross sections for negative ions j.

In an SF_6 plasma, negative ions F^- and S^- are produced through the electron attachment mechanism much more than the other negative ions such as SF^-. Further, because of the existence of the absorption edges, the attachment continuum of F^- occurs at wavelengths below 364.6 nm [21], whilst that of S^- at wavelengths below 614.4 nm [22]. Thus, at a wavelength of 455.0 nm, S^- emits the attachment continuum. Therefore, the author calculated the emission coefficient of the attachment continuum of S^- at the wavelength of 455.0 nm. In the calculation, the values of the photo-detachment cross section $\sigma_{\mathrm{det}}^{S^-}$ given by Robinson and Geltman [23] was used.

(3) **Bremsstrahlung.** The free-free transition of an electron in a Coulomb field leads to the emission of the continuous spectra. The integrated emission coefficient $\varepsilon_{\mathrm{ff}}$ corresponding to this mechanism on the assumption of thermal equilibrium is given by the following expression :

$$\varepsilon_{\mathrm{ff}} = C_1 \frac{N_{\mathrm{e}}(T)}{T^{\frac{1}{2}}} \exp\left(-\frac{hc}{kT\lambda}\right) \sum_{j(\mathrm{ion})} Z_{\mathrm{eff}j}^2 N_j(T) G_{\mathrm{ff}}(\lambda, T) \frac{c\Delta\lambda}{\lambda^2} \qquad (3.3)$$

where $G_{\mathrm{ff}}(\lambda, T)$ is the temperature-averaged free-free Gaunt factor, which is close to unity for a hydrogenic approximation [18, 19, 24]. In this calculation for SF_6 gas, it was assumed that $G_{\mathrm{ff}}(\lambda, T)$ was 1.0.

(4) **Radiation by collision between electron and neutral species.** Collisions between electron and neutral species also result in radiation of the continuous spectra. The corresponding integrated emission coefficient $\varepsilon_{\mathrm{en}}$ is expressed as follows [13, 14] :

$$\varepsilon_{\mathrm{en}} = C_2 T^{\frac{3}{2}} N_{\mathrm{e}}(T) \exp\left(-\frac{hc}{kT\lambda}\right) \sum_{j(\mathrm{neutral})} N_j(T) G_{\mathrm{n}j}(\lambda, T) \frac{c\Delta\lambda}{\lambda^2} \tag{3.4}$$

$$C_2 = \frac{32e^2}{3c^3(4\pi\varepsilon_0)} \left(\frac{k}{2\pi m_{\mathrm{e}}}\right)^{\frac{3}{2}}$$

$$G_{\mathrm{n}j}(\lambda, T) = Q_{\mathrm{en}j}(T) \left[1 + \left(1 + \frac{hc}{kT\lambda}\right)^2\right]$$

where $Q_{\mathrm{en}j}(T)$ is the elastic collision cross section between electron and neutral species j. For the cross sections of e–SF_6, e–SF_4, e–SF_2, e–F_2 and e–S_2, the hard-sphere approximation values given by Frie [25] were utilized. For e–S and e–F, the values calculated by Robinson and Geltman [23] was adopted. For e–Fe, this cross section was regarded as 'Ramsauer cross section' [26].

Figure 3.1 shows four kinds of integrated emission coefficients in pure SF_6 gas as a function of temperature at a pressure of 0.1 MPa. At temperatures below 8000 K, $\varepsilon_{\mathrm{attach}}$ is very much higher than $\varepsilon_{\mathrm{fb}}$, $\varepsilon_{\mathrm{ff}}$ and $\varepsilon_{\mathrm{en}}$. For example, at a temperature of 5000 K, $\varepsilon_{\mathrm{attach}}$ is more than 130 times greater than the values by the other three processes.

Summing up $\varepsilon_{\mathrm{fb}}$, $\varepsilon_{\mathrm{attach}}$, $\varepsilon_{\mathrm{ff}}$ and $\varepsilon_{\mathrm{en}}$ yields the integrated emission coefficient $\varepsilon_{\mathrm{cont}}$ of the continuous spectra as follows :

$$\varepsilon_{\mathrm{cont}} = \varepsilon_{\mathrm{fb}} + \varepsilon_{\mathrm{attach}} + \varepsilon_{\mathrm{ff}} + \varepsilon_{\mathrm{en}}. \tag{3.5}$$

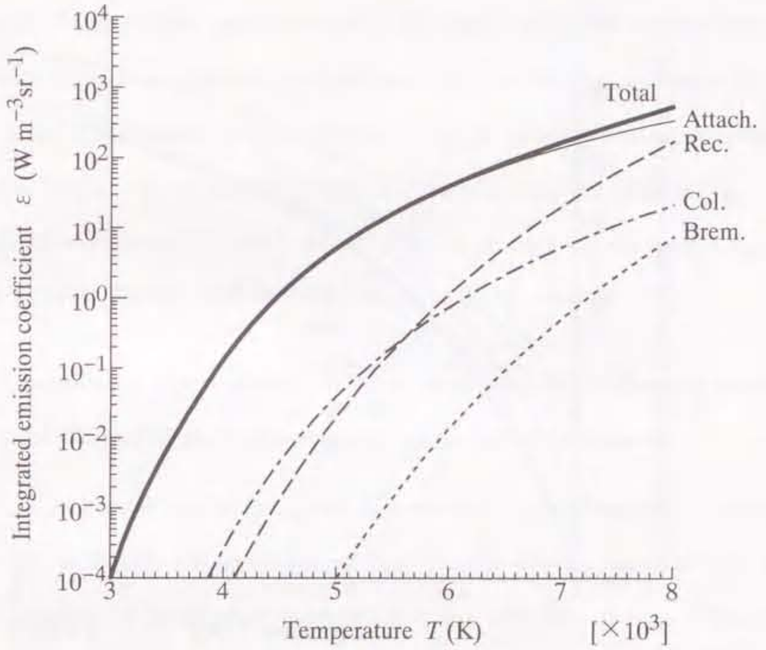

Figure 3.1. Four kinds of integrated emission coefficients of continuous spectra in wavelength range from 454.7 to 455.3 nm in pure SF_6 gas as a function of temperature at 0.1 MPa. Rec., by recombination ; Attach., by electron attachment ; Brem., by free-free transitions of electrons ; Col., by collision between electron-neutral species.

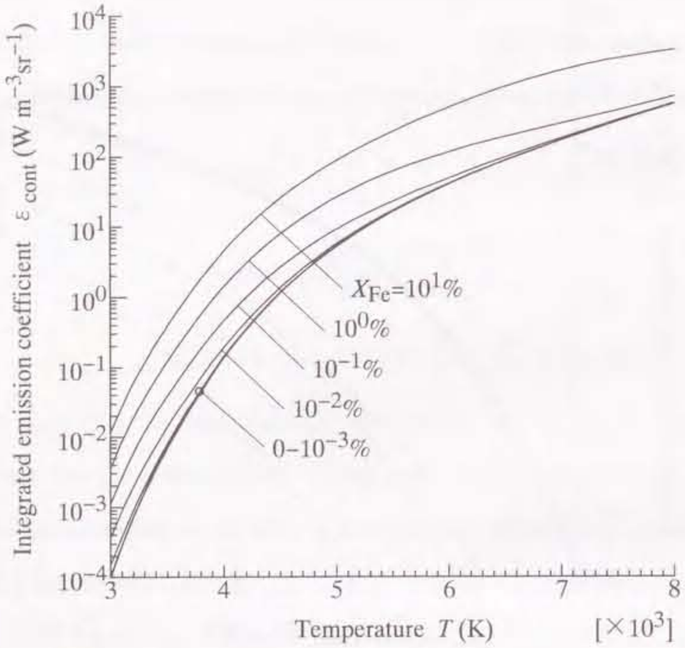

Figure 3.2. Integrated emission coefficient of continuous spectra ε_{cont} in wavelength range from 454.7 to 455.3 nm in SF_6 gas as a function of temperature at 0.1 MPa. Iron vapor concentration X_{Fe} in mass percentage is taken as a parameter.

Figure 3.2 indicates ε_{cont} as a function of temperature T at a pressure of 0.1 MPa. In this figure, iron vapor concentration X_{Fe} is taken as a parameter. As can been seen in this figure, ε_{cont} rises with X_{Fe} at a given temperature T. For instance, at T=4000 K, ε_{cont} for X_{Fe}=0.1 % is 2.42 times higher than that for 0.01 %. Furthermore, ε_{cont} for X_{Fe}=1.0 % is about 7.52 times higher than that for 0.01 %. These results can be interpreted as follows : Iron has a lower ionization potential than S or F [27]. Hence, an increase in X_{Fe} results in a rise of the number density of the electron. This increase causes remarkable electron attachment to S , raising the radiation. Remember that the radiation ε_{attach} by electron attachment account for more than 99 % of the total continuous spectra ε_{cont} at temperatures below 6000 K. Therefore, the increase in X_{Fe} raises ε_{cont}.

3.2.1.2 Comparison of calculated emission coefficient of continuous spectra with measured radiation intensity of background spectra

Now compare theoretically derived ε_{cont} with I_{455} measured in the experiment. Although not being able to directly compare values of I_{455} with the absolute values of ε_{cont}, one is able to compare the temperature dependence of I_{455} with that of ε_{cont}. Figure 3.3 illustrates an example of the measured radiation intensities and the temperature obtained at position M. Use of this figure permits one to obtain I_{455} as a function of temperature. Open circles in Fig. 3.4 indicate the temperature dependence of I_{455} corresponding to Fig. 3.3. The intensity I_{455} decreases with temperature from 5000 to 4600 K, whilst I_{455} increases slightly with a reduction of temperature from 4600 to 4100 K.

In Fig. 3.4, the temperature dependence of ε_{cont} theoretically derived is also shown with full curves. It should be noted that the temperature dependence of ε_{cont} greatly differs from that of I_{455}. This result represents that background spectra must include other

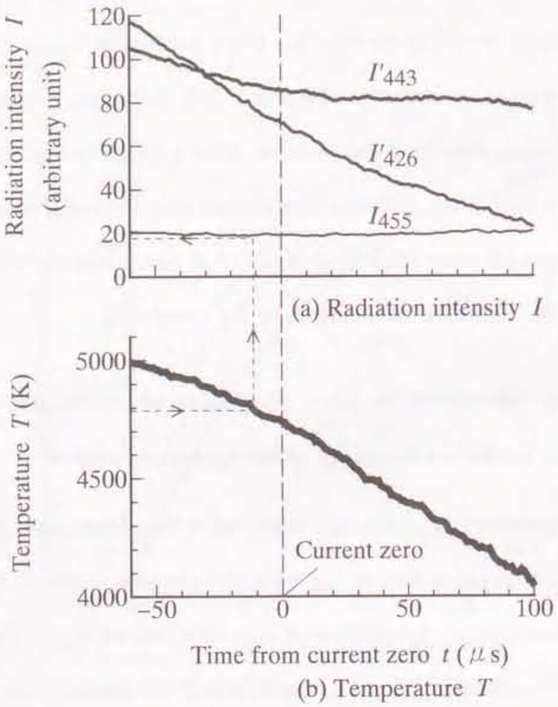

Figure 3.3. Time variations in radiation intensities and temperature at position M.

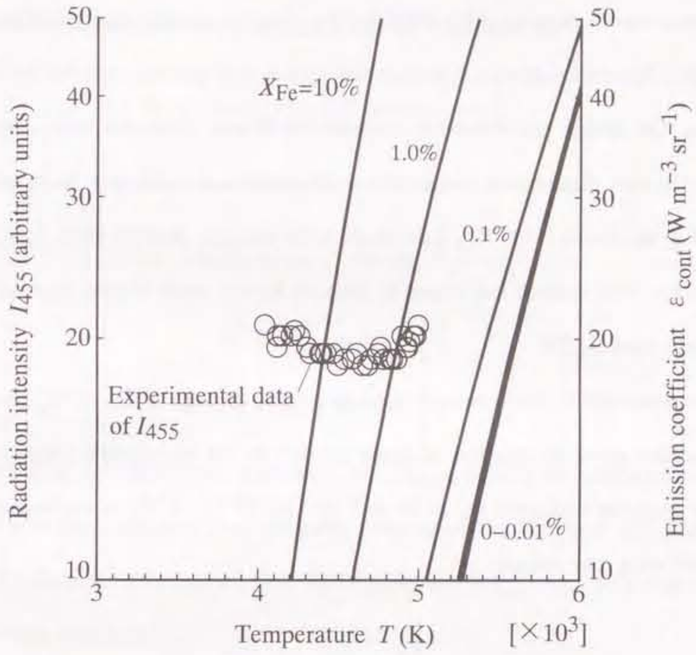

Figure 3.4. Comparison of calculated emission coefficient of continuous spectra with measured radiation intensity of background spectra.

significant spectra besides the continuous spectra in the temperature range of 3000–6000 K.

3.2.1.3 Emission coefficient of S_2 spectra due to $B^3\Sigma_u^- - X^3\Sigma_g^-$ transition

In the temperature range of 3000–6000 K, SF_6 plasmas contain the molecules such as S_2, F_2 and SF_2. Spectral radiation from these molecules may not be negligible for background. Therefore, the author calculates the emission coefficient of spectra from molecules in an SF_6 arc. In this dissertation, a particular attention was paid only to S_2 spectra. The reason is given below : (1) SF_2 has much lower number density than S_2, (2) F_2 emits band spectra with marked low intensity because F_2 has much higher electronic energy of upper state than S_2 [28].

Sulfur molecules S_2 emit the band spectra mainly through $B^3\Sigma_u^- - X^3\Sigma_g^-$ transition [29]. The transition involves emission of many spectra in the wavelength range of 455.0±0.3 nm. The emission coefficient ε_{S_2} in W m^{-3} sr^{-1} for $B^3\Sigma_u^- - X^3\Sigma_g^-$ transition of S_2 is given by the following expressions :

$$\varepsilon_{S_2} = \frac{hc}{4\pi\lambda_{n'n''v'v''J'J''}} N_{n'v'J'}(T) A_{n'n''v'v''J'J''} \tag{3.6}$$

$$N_{n'v'J'}(T) = \frac{N_{S_2}(T)}{U_{S_2}(T)}(2J'+1)\exp\left(-\frac{E'_e + E'_v + E'_r}{kT}\right) \tag{3.7}$$

$$A_{n'n''v'v''J'J''} = \frac{64\pi^4}{3h\lambda^3_{n'n''v'v''J'J''}} |R_e^{n'n''}|^2 q_{v'v''} \frac{S_{J'}}{2J'+1} \tag{3.8}$$

where n, v, J are the quantum numbers concerning electronic, vibrational and rotational state respectively. The prime $'$ denotes the upper state, the double prime $''$ the lower state. The quantities E'_e, E'_v and E'_r are the electronic, the vibrational and the rotational energy levels of upper state, respectively. Then, $\lambda_{n'n''v'v''J'J''}$ is the wavelength, $A_{n'n''v'v''J'J''}$ the

transition probability, $|R_e^{n'n''}|$ the matrix element of the electric dipole moment due to the transition from n' to n'', $q_{v'v''}$ Frank-Condon factor and $S_{J'}$ the line strength. In addition, $N_{S_2}(T)$ and $U_{S_2}(T)$ are the number density and the internal partition function of S_2 respectively. The numerical data on the above variables were obtained as follows :

The vibrational energy level E_v is approximately expressed by

$$E_v = hc\omega_e\left(v+\frac{1}{2}\right) + hc\omega_e x_e\left(v+\frac{1}{2}\right)^2. \tag{3.9}$$

On the other hand, the rotational energy level E_r is given by :

$$E_r = hcB_v J(J+1) - hcD_v J^2(J+1)^2, \tag{3.10}$$

$$B_v = B_e - \alpha_e\left(v+\frac{1}{2}\right), \tag{3.11}$$

$$D_v = D_e + \beta_e\left(v+\frac{1}{2}\right), \tag{3.12}$$

where ω_e and $\omega_e x_e$ are vibrational constants, B_e, D_e, α_e and β_e are rotational constants. These constants were obtained from the table summarized by Herzberg [28]. Using these energy level indicated by equations (3.9)–(3.12), the wavelength $\lambda_{n'n''v'v''J'J''}$ is expressed by the following equation :

$$\lambda_{n'n''v'v''J'J''} = \frac{hc}{(E'_e + E'_v + E'_r) - (E''_e + E''_v + E''_r)}. \tag{3.13}$$

The matrix element $|R_e^{n'n''}|$ of the electric dipole moment can be estimated by the magnitude of the radiative lifetime of the transition. The radiative lifetime of $B^3\Sigma_u^- - X^3\Sigma_g^-$ of S_2 was measured by Smith [30].

Frank-Condon factors $q_{v'v''}$ of S_2 $B^3\Sigma_u^- - X^3\Sigma_g^-$ transition are given by Smith and Liszt [31] and Herman and Felenbok [32]. These values are available for the calculation of equation (3.8).

The line strength $S_{J'}$ is formulated by Hönl and London on the basis of old quantum theory [33]. In accordance with their formulae, the line strengths $S^{\mathrm{P}}_{J'}$, $S^{\mathrm{Q}}_{J'}$ and $S^{\mathrm{R}}_{J'}$ for P, Q and R branch of the Σ–Σ transition are expressed by [33]

$$S^{\mathrm{P}}_{J'} = J', \tag{3.14}$$

$$S^{\mathrm{Q}}_{J'} = 0, \tag{3.15}$$

and

$$S^{\mathrm{R}}_{J'} = J' + 1. \tag{3.16}$$

In the above calculations, the vibrational transitions (v', v'')=(0,0), (0,1), (0,2), $\cdots$, (12,25), (12,26) were taken into account. For each of the vibrational transitions, the rotational transitions for P and R branches with J'=0, $\cdots$, 500 were taken into consideration. For each of the combinations (v', v'', J'), the wavelength $\lambda_{n'n''v'v''J'J''}$ were calculated using equations (3.9)–(3.13).

The integrated emission coefficient $\varepsilon_{\mathrm{S}_2 455}$ in the wavelength range of 455.0±0.3 nm was expressed as follows :

$$\varepsilon_{\mathrm{S}_2 455} = \sum_{455.0\pm0.3\mathrm{nm}} \varepsilon_{\mathrm{S}_2} \tag{3.17}$$

The summation sign $\sum_{455.0\pm0.3\mathrm{nm}}$ in equation (3.17) indicates that all the emission coefficients of spectra in the wavelength range of 455.0±0.3 nm should be summed up.

Figure 3.5 represents $\varepsilon_{\mathrm{S}_2 455}$ at a pressure of 0.1 MPa as a function of temperature for iron vapor concentration X_{Fe} from 0 to 10 %. It can be seen that for a given temperature, $\varepsilon_{\mathrm{S}_2 455}$ is almost independent of X_{Fe} in range of $0-10\%$. In addition, $\varepsilon_{\mathrm{S}_2 455}$ decreases gradually with increasing temperature. For example, $\varepsilon_{\mathrm{S}_2 455}$ has a magnitude of 19.8 W m^{-3} sr^{-1} at 3000 K, while $\varepsilon_{\mathrm{S}_2 455}$ is 5.39 W m^{-3} sr^{-1} at 8000 K.

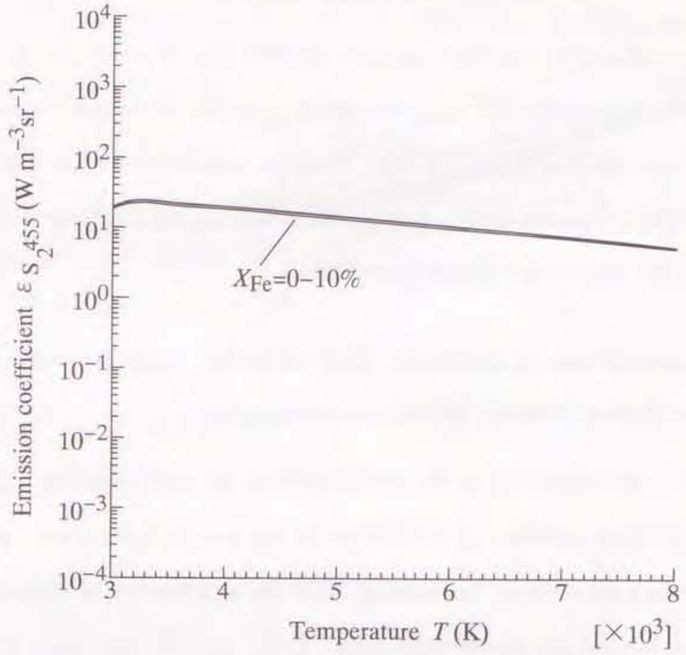

Figure 3.5. Integrated emission coefficient due to S_2 $B^3\Sigma_u^- - X^3\Sigma_g^-$ transition in wavelength range from 454.7 to 455.3 nm in SF_6 gas as a function of temperature at 0.1 MPa. Iron vapor concentration X_{Fe} is taken as a parameter.

3.2.1.4 Total emission coefficient at wavelength of 455.0 nm

Adding ε_{S_2455} to ε_{cont}, the author obtained the total emission coefficient ε_{455} at 455.0 nm, i.e.

$$\varepsilon_{455} = \varepsilon_{cont} + \varepsilon_{S_2455} \tag{3.18}$$

In Fig. 3.6, bold curves represent ε_{455} as a function of T at a pressure of 0.1 MPa. Dotted and broken curves show ε_{S_2455} and ε_{cont} respectively. At temperatures above 6000 K, ε_{455} is dominated by ε_{cont} for all X_{Fe}. While at temperatures below 4500 K, ε_{455} is predominated by ε_{S_2455} for all X_{Fe}. It is also noted that ε_{455} for X_{Fe} below 10^{-2} % is kept constant in the temperature from 4000 to 5000 K.

3.2.1.5 Comparison of calculated total emission coefficient with measured radiation intensity of background spectra

Figure 3.7 shows comparison of the calculated total emission coefficient ε_{455} with the measured radiation intensity I_{455} at 455.0 nm in temperature dependence. Bold curves represents the total emission coefficient at 455.0 nm as a function of temperature with reference to vertical axis on the right hand. Open circles in this figure indicates the temperature dependence of I_{455} with reference to the vertical axis on the left hand. These data are the same as those in Fig. 3.4. It should be noted that the temperature dependence of ε_{455} for X_{Fe}=0–0.01 % agrees fairly well with that of I_{455}. This agreement indicates that the radiation intensity at 455 nm mainly consists of not continuous spectra but S_2 spectra through $B^3\Sigma_u^- - X^3\Sigma_g^-$ transition at temperatures below 4500 K.

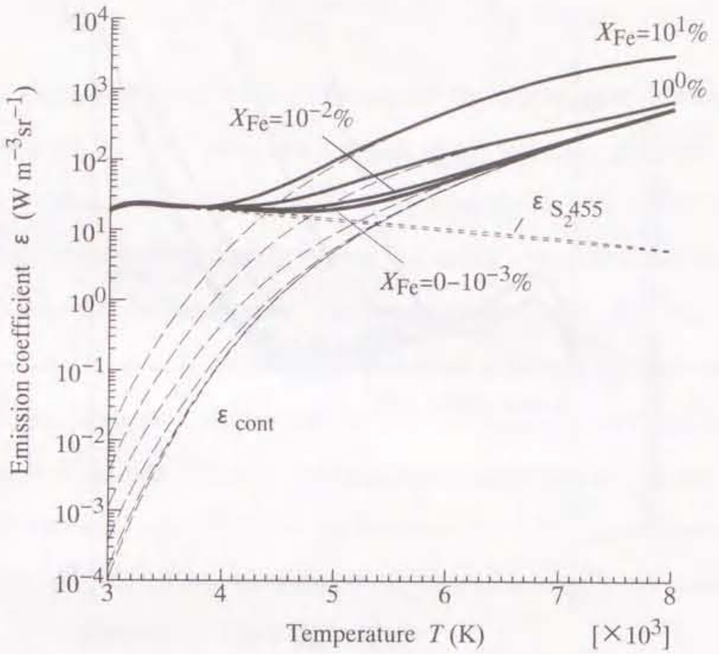

Figure 3.6. Total emission coefficient ε_{455} in wavelength range from 454.7 to 455.3 nm in SF_6 gas as a function of temperature at 0.1 MPa. Iron vapor concentration X_{Fe} is taken as a parameter.

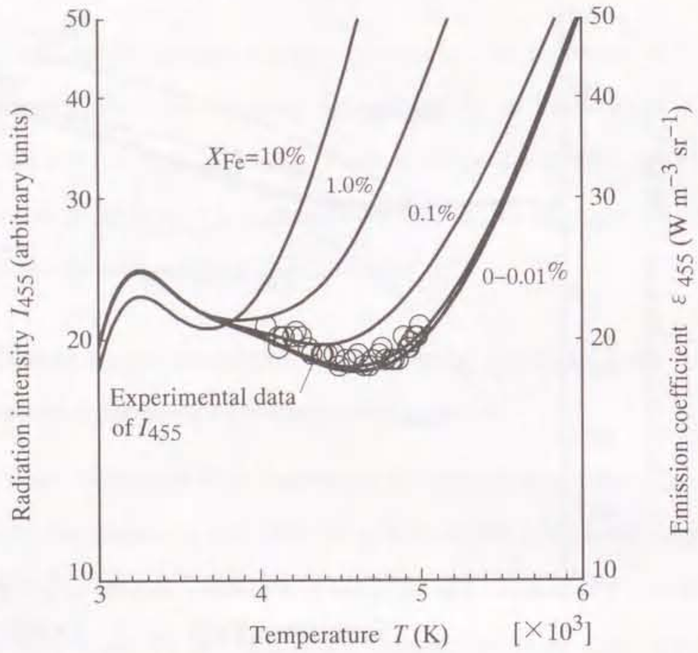

Figure 3.7. Comparison of total emission coefficient of background spectra with measured radiation intensity at 455.0 nm.

3.2.2 Emission coefficient of Fe spectral line

As described in section 2.2.2, The absolute emission coefficient ε_{nm} (in W m^{-3} sr^{-1}) of an Fe spectral line is given by:

$$\varepsilon_{nm} = \frac{hc}{4\pi} \frac{N_{\mathrm{Fe}}(T)}{U_{\mathrm{Fe}}(T)} \frac{g_n A_{nm}}{\lambda_{nm}} \exp\left(-\frac{E_n}{kT}\right), \tag{3.19}$$

where $N_{\mathrm{Fe}}(T)$ and $U_{\mathrm{Fe}}(T)$ are the number density and the internal partition function of Fe respectively [34, 35]. The subscripts n and m denote the upper and lower energy levels respectively, g_n is the statistical weight of the upper state n, A_{nm} is the transition probability, λ_{nm} is the wavelength of the spectral line and E_n is the potential of the upper level n with respect to the ground state. The atomic constants of g_n, A_{nm}, λ_{nm} and E_n of Fe spectral lines are given by Fuhr *et al.* as summarized in Table 2.1 [36]. On the basis of the above data, the author calculated the emission coefficient $\varepsilon_{\mathrm{Fe426}}$ of Fe spectral line at a wavelength of 426.0 nm. Figure 3.8 shows $\varepsilon_{\mathrm{Fe426}}$ as a function of temperature T at a pressure of 0.1 MPa for various X_{Fe}. As can be seen in Fig. 3.8, $\varepsilon_{\mathrm{Fe426}}$ increases with a rise of temperature T for all X_{Fe}. For a given T, as X_{Fe} increases, $\varepsilon_{\mathrm{Fe426}}$ also increases.

3.2.3 Ratio of emission coefficient of Fe spectrum to that of background spectra

From ε_{455} and $\varepsilon_{\mathrm{Fe426}}$, the ratio $\varepsilon_{\mathrm{Fe426}}/\varepsilon_{455}$ was derived. Figure 3.9 shows the $\varepsilon_{\mathrm{Fe426}}/\varepsilon_{455}$ at 0.1 MPa as a function of T with X_{Fe} as a parameter. Use of this figure allows the determination of X_{Fe} in the arc channel. The next section will explain the detailed procedure.

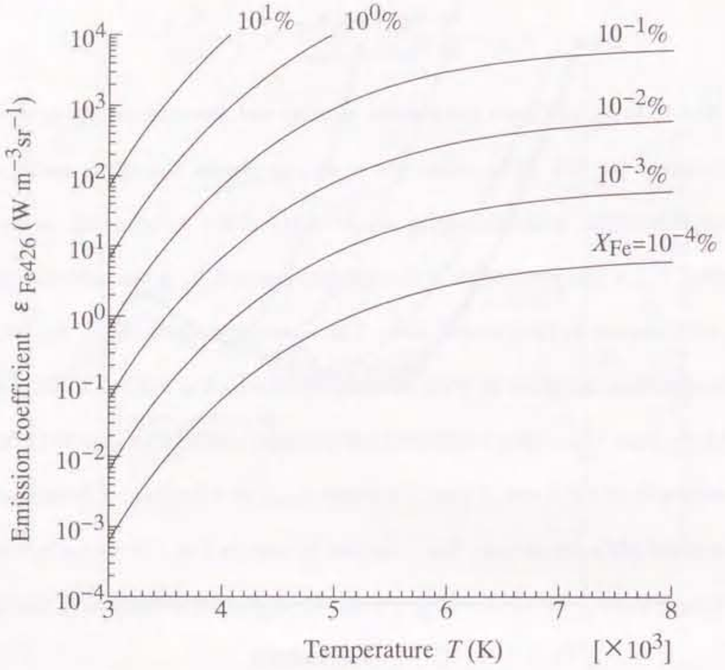

Figure 3.8. Emission coefficient ε_{Fe426} of Fe spectral line at 426.0 nm in SF_6 gas as a function of temperature at 0.1 MPa. Iron vapor concentration is taken as a parameter.

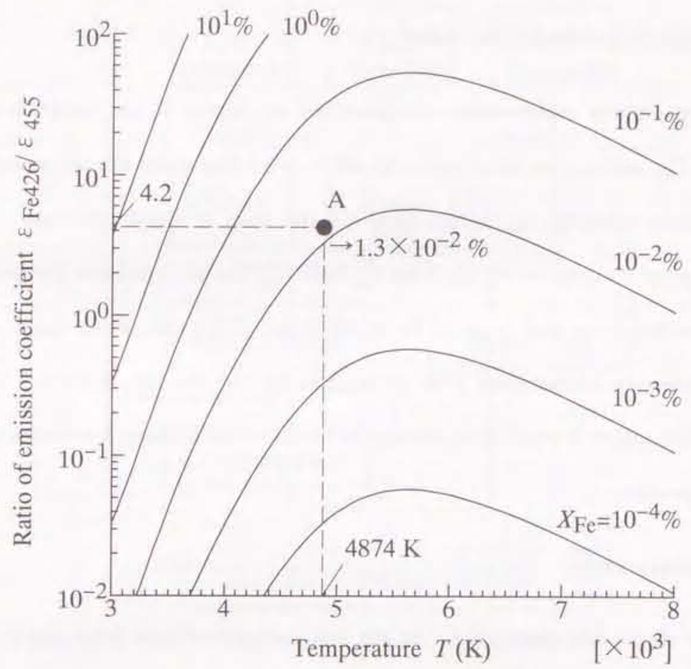

Figure 3.9. Ratio of emission coefficients ε_{Fe426} to ε_{455} in SF_6 gas as a function of temperature at 0.1 MPa. Iron vapor concentration X_{Fe} is taken as a parameter.

3.3 Method for deriving iron vapor concentration from spectroscopic observation

Figure 3.10 indicates a flow chart of the procedure for estimating X_{Fe} in the experiment. The detailed procedure is given below.

(1) **Temperature estimation.** As described in chapter 2, the radiation intensities I'_{426}, I'_{443} and I_{455} at wavelengths of 426.0, 442.7 and 455.0 nm are measured. The radiation intensity I_{455} is free from spectral lines of atoms and ions. Therefore, numerical subtraction of I_{455} from I'_{426} and I'_{443} directly produces the net radiation intensities I_{Fe426} and I_{Fe443} of Fe at 426.0 and 442.7 nm. From I_{Fe426} and I_{Fe443}, the post-arc temperature T is determined by the two-line method. Use of this method makes it possible to determine temperature without knowledge of particle composition.

(2) **Intensity ratio.** The ratio of I_{Fe426} to I_{455} is estimated.

(3) **Iron vapor concentration.** In Fig. 3.9, a measured point is plotted at a position with co-ordinates T and $I_{\mathrm{Fe426}}/I_{455}$. The iron vapor concentration X_{Fe} is estimated from the location of that point.

As an example, let us assume the temperature T and the intensity ratio $I_{\mathrm{Fe426}}/I_{455}$ to be 4874 K and 4.2 respectively. One can plot a filled circle at the position marked with A in Fig. 3.9. From the location of the filled circle, the iron vapor concentration is estimated to be 1.3×10^{-2} %.

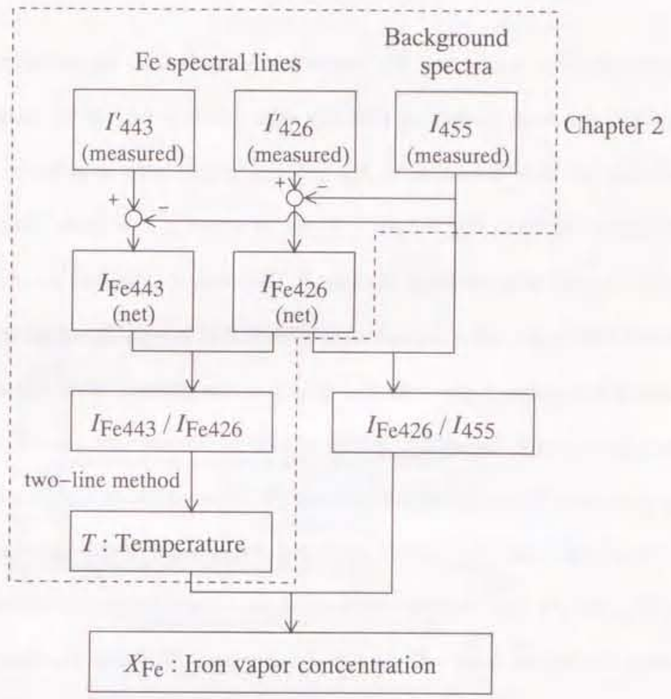

Figure 3.10. Flow chart of procedure for determination of iron vapor concentration.

3.4 Axial distribution of iron vapor concentration around current zero

The method for estimating X_{Fe} was actually applied to the post-arc channel in the flat-type SF_6 gas-blast quenching chamber with gas flow rate of 50 liters min^{-1}. Figure 3.11 indicates the time variation in X_{Fe} around current zero at position M derived from the waveforms shown in Fig. 3.3 (a). It can be noted in this figure that X_{Fe} mostly remains to be constant with the lapse of time. In this case, X_{Fe} was estimated to be about 1×10^{-2} % both before and after current zero. Figure 3.11 clearly demonstrates that the proposed method is capable of deriving X_{Fe} in a post-arc channel after current zero. This is one importance factor the author should emphasize – until now, metallic vapor concentration has been hardly measured by spectroscopic observation in a post-arc channel.

In a similar way, the author measured X_{Fe} at each of the observation positions on the nozzle axis. At any position, the iron vapor concentration X_{Fe} was also mostly constant during the period from -60 to 100 μs. Figure 3.12 shows the axial distribution of X_{Fe} during the time around current zero. Each triangle designates the average X_{Fe} of five measurements from -60 μs to 100 μs after current zero. The fluctuations in X_{Fe} are also given by the error bars. It should be noted in Fig. 3.12 that X_{Fe} values at all observation positions are around 1×10^{-2} % during the time around current zero.

3.5 Discussion

3.5.1 Advantages of new estimation method

The proposed method has the following four advantages :

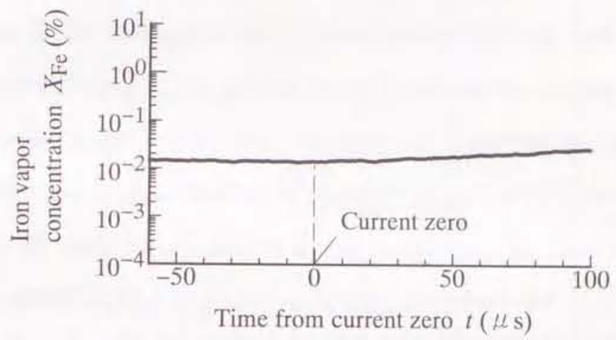

Figure 3.11. Time variation in iron vapor concentration X_{Fe} around current zero (peak value of current, 5 kA ; SF_6 gas flow rate, 50 liters min^{-1} ; observation position, M.)

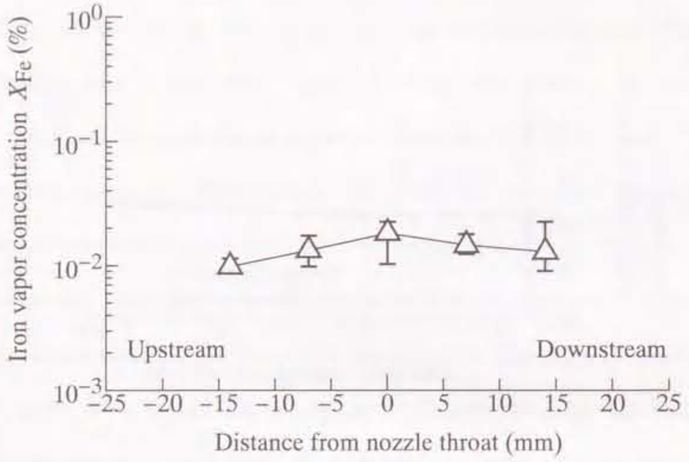

Figure 3.12. Axial distributions of iron vapor concentration X_{Fe} in SF_6 gas arcs around current zero : (peak value of current, 5 kA ; SF_6 gas flow rate, 50 liters min^{-1}).

(1) The observed two Fe spectral lines and the background spectra have radiation intensities enough to be detected with photomultiplier tubes even up to 100 μs after current zero. Thus, the iron vapor concentration X_{Fe} can be estimated up to this time.

(2) The iron vapor concentration X_{Fe} is estimated from T and I_{Fe426}/I_{455}. The temperature T is obtained from the ratio of I_{Fe443}/I_{Fe426}. Hence, the author's estimation method does not require the absolute radiation intensities I_{Fe426}, I_{Fe443} and I_{455}.

(3) Several papers have reported on the metallic vapor concentration in an arc during high current phase [1]–[4]. In these works, a spectral line emitted from gas species such as S^+ and F was observed together with a spectral line emitted from the metallic vapor species. However, it should be noted that the new method does not require the measurement of spectral lines emitted from gas particles but only three spectral lines required in estimation of temperature.

(4) Concerning the SF_6 gas arc burning between the iron electrodes, the author described the new method for determining metallic vapor concentration. The author's method seems to be applicable to arcs burning other materials such as copper. However, the measurement of other metallic vapor concentration is restricted to the arc during high current phases. This is because the radiation intensity reduces to a low magnitude around current zero.

3.5.2 Error in estimating iron vapor concentration

3.5.2.1 Uncertainty caused by the uncertainty in temperature

As seen in previous chapter, the measured temperature has an uncertainty due to uncertainties of transition probabilities. This uncertainty induces an uncertainty in determining the iron vapor concentration X_{Fe}. Figure 3.13 represents $\varepsilon_{\mathrm{Fe426}}/\varepsilon_{455}$ derived theoretically as a function of T for the estimation of X_{Fe}, namely, the same curves as those shown in Fig. 3.9. Let us take $T = 5000$ K and $I_{\mathrm{Fe426}}/I_{455}$=1.0 as an example. In this case, X_{Fe} is estimated to be 2.5×10^{-3}% from the position of the corresponding filled circle. Recall that the temperature has an uncertainty of ±284 K. In Fig. 3.13, the open triangle lies at the location corresponding to 4716 K, whilst the open square 5284 K. From the positions of the open triangle and square, X_{Fe} values are estimated to be 4.0×10^{-3} and 1.9×10^{-3}%, respectively. Thus, the relative uncertainties $\Delta X_{\mathrm{Fe}}/X_{\mathrm{Fe}}$ at $T = 5000$ K is found to be +0.6 and −0.23. These uncertainties are nearly constant irrespective of $I_{\mathrm{Fe426}}/I_{455}$.

3.5.2.2 Pressure rise

In the process of determining the iron vapor concentration, the gas pressure around the nozzle throat was assumed to be 0.1 MPa. In the quenching chamber, however, the pressure around current zero might be higher than 0.1 MPa. The author thus measured the pressure at the nozzle throat around current zero in the flat-type quenching chamber with a pressure transducer. The pressure at the nozzle throat around current zero was found to be 0.12 MPa.

The ratio $\varepsilon_{\mathrm{Fe426}}/\varepsilon_{455}$ as a function of temperature was theoretically calculated under the condition with a pressure of 0.12 MPa. The calculation results show that no remark-

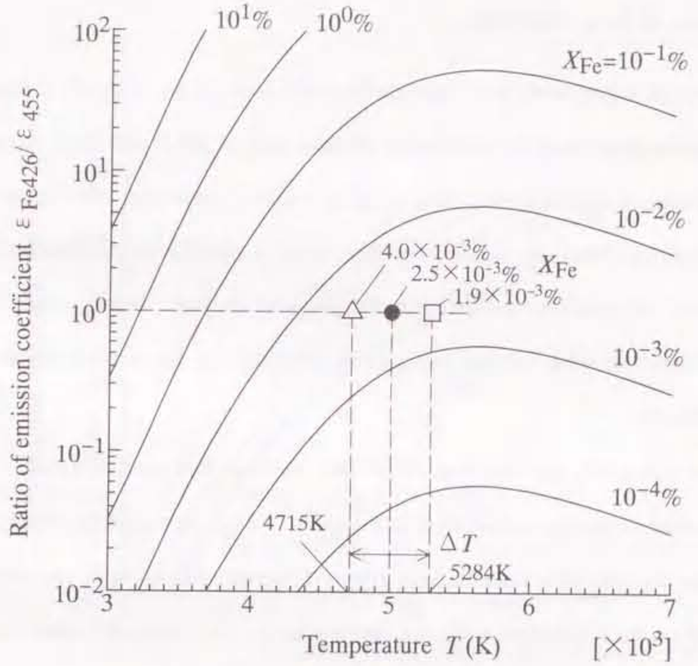

Figure 3.13. Uncertainty in estimating iron vapor concentration by uncertainty in temperature.

able difference in $\varepsilon_{\mathrm{Fe426}}/\varepsilon_{455}$ was found between cases at pressures of 0.12 MPa and 0.1 MPa. Consequently, a slight rise in the gas pressure causes little error in determining the iron vapor concentration.

3.5.3 Use of iron electrodes

In the present experiment, iron was intentionally used as an electrode material in the flat-type quenching chamber because Fe spectral lines at 426.0 and 442.7 nm much have higher emission coefficients than that of an S^+, F or Cu particles. Measurement of radiation intensities of the two Fe spectral lines makes it possible to determine the post-arc temperature after current zero, as seen in previous chapter. Furthermore, iron vapor concentration even after current zero can be estimated by the method described in the present chapter.

In a practical SF_6 gas-blast circuit breaker, not iron but another metal, e.g. copper-tungsten alloy, is usually used as an arcing contact. As is known, iron has different melting and boiling temperatures from those of copper-tungsten. Accordingly, the metallic vapor concentration in a chamber with iron electrodes is not necessarily same to that in a chamber with other metallic electrodes.

However, the author carried out experiments to find out that the iron vapor concentration was only of order 10^{-2} % around current zero. Theoretical calculations of particle composition showed that high-temperature SF_6 gas with an iron vapor concentration of only 10^{-2} % has almost the same properties as the pure SF_6 gas. Let us take electron density as an example. Figure 3.14 shows the electron number density in high-temperature SF_6 gas contaminated with iron vapor as a function of temperature. Iron vapor concentration X_{Fe} is taken as a parameter. As seen in the figure, the electron density for

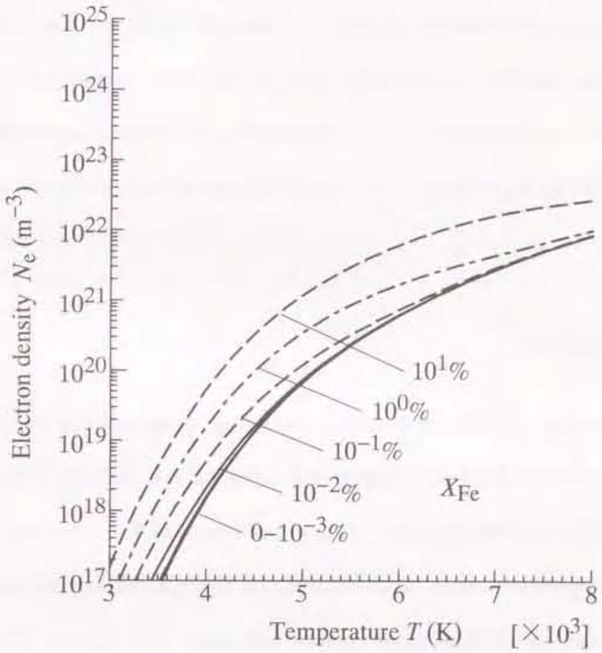

Figure 3.14. Electron density in SF_6 gas contaminated with iron vapor as a function of temperature at 0.1 MPa. Iron vapor concentration X_{Fe} is taken as a parameter.

X_{Fe}=10^{-2} % is as high as that for X_{Fe}=0 %, namely the pure SF_6 gas. For instance, at 5000 K, the electron density is 6.8×10^{19} m^{-3} for pure SF_6 gas, while 7.4×10^{19} m^{-3} for SF_6 gas with X_{Fe}=10^{-2} %. Above calculation results also suggest that the electrical conductivity of the SF_6 gas with X_{Fe} of 10^{-2} % is almost equal to that of the pure SF_6 gas. This is because the electrical conductivity depends chiefly on the electron density. Thus, it seems that use of iron electrodes gives no influence on post-arc characteristics after current zero in the chamber. As a consequence, the decaying process of post-arc in this experiment can be regarded as that in pure SF_6 gas, although the iron electrode was used.

3.6 Conclusions

A method for deriving metallic vapor concentration in an arc column was developed on the basis of spectroscopic method ; background radiation was utilized. For this purpose, emission coefficient of background spectra at a wavelength of 455.0 nm was theoretically calculated for temperature range 3000–8000 K. In this calculation, S_2 spectra due to $B^3\Sigma_u^-$–$X^3\Sigma_g^-$ as well as the continuous spectra was taken into account. The calculation revealed that the background spectra is dominated by the continuous spectra at temperatures above 4500 K, whilst by the S_2 spectra at temperatures below 4500 K. The calculated coefficient was compared with the measured radiation intensity of background spectra at 455.0 nm in temperature dependence. The comparison shows that the calculation result of emission coefficient fairly agrees with the experimental result of the radiation intensity.

The method was applied to the post-arc channel after current zero in a flat-type SF_6 gas-blast quenching chamber with iron electrodes as an example. From the radiation intensities measured at each of five positions, the iron vapor concentration was successfully

estimated up to 100 μs after current zero. Furthermore, the axial distribution of iron vapor concentration was also estimated around current zero. The iron vapor concentration at all observation positions along the nozzle axis had a magnitude of 1×10^{-2} % during the time around current zero.

References

[1] D. R. Airey, "Time dependent energy balance of a 20 kA SF_6 arc contaminated with electrode vapor", *in Proc. 5th Int. Conf. on Gas Discharges and Their Applications*, 1978, pp.21–24.

[2] D. R. Airey, "A rapid-scanning polychromator for time-resolved temperature and radius measurements in 40 kA SF_6 arcs", *J. Phys. E: Sci. Instrum.*, Vol. 12, pp.397–402, 1979.

[3] H. Ikeda, G. R. Jones, M. Irie and A. N. Prasad, "Spectroscopy of very high current, convention arcs", *in Proc. 7th Int. Conf. on Gas Discharges and Their Applications*, 1982, pp.5–8.

[4] J. P. Dinguirard, C. Espardeillier, and S. Vacquie, "Study of an extinguishing arc discharge in copper nitrogen mixture", *in Proc. 5th Int. Conf. on Gas Discharges and Their Applications*, 1978,pp.142–143.

[5] S. Tayor, G. R. Jones and S. M. El-Kholy, "Relationship between circuit-breaker performance and nozzle blocking, contact evaporation and particle production", *IEE Proc.–Sci. Meas. Technol.*, Vol. 141, pp.508–512, 1994.

[6] T. Sakuta, Y. Kito and I. Miyachi, "Practical evaluation of copper vapor concentration in high current air arcs", *in Proc. 6th Int. Conf. on Gas Discharges and Their Applications*, 1980, pp.239–242.

[7] Y. Kito, T. Sakuta and M. Kurono, "Decaying processes of temperature and copper vapor concentration toward current zero in the alternative-current arc", *Trans. IEE of Japan*, Vol. 103, pp.125–126, 1983.

[8] G. Raynal, P. J. Vergne and A. Gleizes, "Radiative transfer in SF_6 and SF_6-Cu arcs", *J. Phys. D: Appl. Phys.*, Vol. 28, pp.508–515, 1995.

[9] T. Sakuta and T. Takashima, "Multi-mixing effects of nozzle and electrode materials on transport and thermodynamic properties of SF_6 under current interrupting condition", *in Proc. 10th Int. Conf. on Gas Discharges and Their Applications*, Vol. I, 1992, pp.110–113.

[10] T. Sakuta, S. Terauchi, T. Takashima and M. Ishikawa, "Transport properties of high temperature SF_6 gas contaminated with Cu and PTFE vapor at high pressure condition", *Trans. of IEE of Japan*, Vol. 113–B, pp.342–350, 1993(in Japanese).

[11] B. Chervy, A. Gleizes and M. Razafinimanana, "Thermodynamic properties and transport coefficients in SF_6–Cu mixtures at temperatures of 300–30000K and pressures of 0.1–1 MPa", *J. Phys. D: Appl. Phys.*, Vol. 27, pp.1193–1206, 1994.

[12] Y. Yokomizu, T. Sakuta and Y. Kito, "A novel approach to AC air arc interruption phenomena viewed from the electron density at current zero", *J. Phys. D: Appl. Phys.*, Vol. 22, pp.129–135, 1989.

[13] F. Cabannes and J. Chapelle, *Reactions under Plasma Conditions*, Vol. 1, ed. Venugopalan. New York : Wiley–Interscience, 1971, ch.7.

[14] A. Gleizes, M. Gongassian and B. Rahmani, "Continuum absorption coefficient in SF_6 and SF_6–N_2 mixture plasmas", *J. Phys. D: Appl. Phys.*, Vol. 22, pp.83–89, 1989.

[15] M. I. Boulos, P. Fauchais and E. Pfender, *Thermal Plasma, Fundamentals and Applications, Vol. 1*. New York : Plenum, 1994, pp.348–358.

[16] L. M. Bibermann and G. E. Norman, "On the calculation of photoionization absorption", *Optics Spectrosc.*, Vol. 8, pp.230–232, 1960.

[17] M. Gongassian and A. Gleizes, "Calculation of recombination continuum of F^+ and F^{++} ions in thermal plasmas", *in Proc. 18th Int. Conf. on Phenomena in Ionized Gases*, 1987, pp.72–73.

[18] H. Kafrouni and S. Vacquie, "Study of the recombination continuum an SF_6 arc discharge", *J. Quant. Spectrosc. Radiat. Transfer*, Vol. 32, pp.219–224, 1984.

[19] J. Richter, *Plasma Diagnostics* ed. W. Lochte–Holtgreven. Amsterdam : North–Holland, 1968, ch.1.

[20] J. M. Yos, *Transport properties of nitrogen, hydrogen, oxygen and air to 30,000 K, Technical Memorandum, RAD–TM–63–7*. Massachusetts : Research and Advanced Development Division AVCO Corporation, 1963, p.16.

[21] A. Mandl, "Electron photodetachment cross section of the negative iron of fluorine", *Phys. Rev. A*, Vol. 3, pp.251–255, 1971.

[22] W. C. Lineberger and B. W. Woodward, "High resolution phtodetachment of S^- near threshold", *Phys. Rev. Lett.*, Vol. 25, pp.424–427, 1970.

[23] E. J. Robinson and S. Geltman, "Single- and double-quantum photodetachment of negative ions", *Phys. Rev.*, Vol. 153, no.1, pp.4–8, 1967.

[24] W. J. Karzas and R. Latter, "Electron radiative transitions in a Coulomb field", *Astrophys. J. Suppl. Ser.*, Vol. 6, no.55, pp.167–212, 1961.

[25] W. Frie, "Berechung der Gas zusammensetzung und der Materialfunktionen von SF_6", *Z. Phys.*, Vol. 201, pp.269–294, 1967.

[26] V. H. Maecker, "Über den Querschnitt des Fluoratoms gegenüber Elektronenstoß ", *Ann. Phys.*, Vol. 18, pp.441–446, 1956.

[27] C. E. Moore, *Atomic Energy Levels* Vol. II. Washington DC : NBS, 1952.

[28] G. Herzberg, *Molecular Spectra and Molecular Structure Vol. IV. Constants of Diatomic Molecules.* London : Litton, 1979.

[29] R. W. B. Pearse and A. G. Gaydon, *The Identification of Molecular Spectra*, New York : Wiley, 1976.

[30] W. H. Smith, "Absolute transition probabilities for some electronic states of CS, SO and S_2", *J. Quant. Spectrosc. Radiat. Transfer*, Vol. 9, pp.1191–1199, 1969.

[31] W. H. Smith and H. S. Liszt, "Franck-Condon factors and absolute oscillator strengths for NH, SiH, S_2 and SO", *J. Quant. Spectrosc. Radiat. Transfer*, Vol. 11, pp.45–54, 1971.

[32] L. Herman and P. Felenbok, "Effect des collisions sur la predissociation de S_2", *J. Quant. Spectrosc. Radiat. Transfer*, Vol. 3, pp.247–254, 1963.

[33] G. Herzberg, *Molecular Spectra and Molecular Structure Vol I. Spectra of Diatomic Molecules.* New York : Van Nostrand, 1950.

[34] G. R. Jones, *High Pressure Arcs in Industrial Devices, Diagnostic and Monitoring Techniques*, Cambridge : Cambridge University Press, 1988, p.167.

[35] M. I. Boulos, P. Fauchais and E. Pfender, *Thermal Plasma, Fundamentals and Applications, Vol. 1.* New York : Plenum, 1994, p.345

[36] J. R. Fuhr, G. A. Martin and W. L. Wiese, *Atomic Transition Probabilities Iron through Nickel Vol. 17, Suppl.4.* Maryland : NBS, 1988.

Chapter 4 The opening process of thermal plasma contacts in an SF_6 post-arc channel

4.1 Introduction

In chapter 2, decay aspect of the axial temperature distribution in the post-arc channel around the nozzle throat was found up to 100 μs after current zero. The temperature decreases more rapidly at the nozzle throat than at the other axial positions. In chapter 3, the author has described iron vapor concentration X_{Fe} in the post-arc channel in the quenching chamber. At any observation position along the nozzle axis, X_{Fe} was estimated to be 0.01 % during the period around current zero.

In the present chapter, an increase of electrical resistivity ρ_{res} of the post-arc channel up to 100 μs after current zero in a flat-type SF_6 gas-blast quenching chamber is described. First, ρ_{res} of SF_6 gas contaminated with the iron vapor is calculated as functions of temperature T and iron vapor concentration X_{Fe}. Secondly, using this theoretical data, the axial distribution of ρ_{res} of the post-arc channel is estimated from T and X_{Fe} given previously. The results demonstrate that ρ_{res} increases more rapidly at the nozzle throat than at the other axial positions. Thirdly, in terms of the increasing aspect of the axial distribution of ρ_{res}, a concept of 'thermal plasma contacts' is proposed to interpret arc quenching processes. Finally, the behavior of the thermal plasma contacts is numerically discussed in the case that a transient recovery voltage was applied between the electrodes in the flat-type SF_6 gas-blast quenching chamber.

4.2 Electrical resistivity of high-temperature SF_6 gas contaminated with iron vapor

4.2.1 Calculation procedure

Electrical resistivity ρ_{res} of high-temperature SF_6 gas contaminated with iron vapor can hardly found in the open literatures. Therefore, the author newly calculated it as a function of T under the condition of thermal equilibrium. Using the first order approximation of Chapman-Enskog method simplified by Yos, the electrical resistivity ρ_{res} of high-temperature gas can be computed [1]. The expression is given by

$$\rho_{\mathrm{res}} = \frac{kT}{e^2 N_{\mathrm{e}}} \sum_j{}' N_j \Delta_{ej}^{(1)}, \tag{4.1}$$

where

$$\Delta_{ej}^{(1)} = \frac{8}{3}\sqrt{\frac{2m_e m_j}{\pi kT(m_e+m_j)}}\pi\bar{\Omega}_{ej}^{(1,1)}, \tag{4.2}$$

T is the temperature, N_{e} is the electron density, N_j is the number density of species j, m_{e} is the mass of electron, e is the electronic charge, k is the Boltzmann's constant. The quantity $\pi\bar{\Omega}_{ej}^{(1,1)}$ is the diffusion cross section between the electron and the particle of the species j. Strictly speaking, this quantity is the collision integrals. In equation (4.1), the sign $\sum_j'$ designates the summation of $N_j\Delta_{ej}^{(1)}$ for all species except the electron, i.e. except j =e.

Calculation of ρ_{res} by equations (4.1) and (4.2) requires the numerical data on N_{e}, N_j and $\pi\bar{\Omega}_{ej}^{(1,1)}$. The author obtained these data as described below.

(1) **Number density N_{e} and N_j.** The equilibrium composition of high-temperature SF_6 gas contaminated with iron vapor has already been calculated theoretically to obtain number densities N_{e} and N_j in chapter 2.

Table 4.1. Radii for SF_6, SF_2, F_2, S_2 [2].

Species	Radii ($\times 10^{-10}$m)
SF_6	2.94
SF_4	2.66
SF_2	2.31
F_2	1.88
S_2	2.25

(2) **Diffusion cross section $\pi\bar{\Omega}_{ej}^{(1,1)}$.** Frie has reported radii of the neutral molecules SF_6, SF_4, SF_2, F_2 and S_2 as summarized in Table 4.1 [2]. From these radii, the author calculated approximately the diffusion cross-sections between the above neutral molecules and the electron on the basis of the hard-sphere method.

For the reaction between the electron and F as well as that between the electron and S, Robinson and Geltman have calculated the elastic cross sections as a function of electron energy [3]. From these data, the author calculated the diffusion cross sections as a function of temperature in accordance with the method given by Chapman and Cowling [4].

The diffusion cross section between the electron and Fe was assumed to be 'Ramsauer cross section' [5, 6]. The diffusion cross sections between the electron and ions were calculated from Gvosdover cross sections for Coulomb collisions [7].

Figure 4.1 shows the diffusion cross sections $\pi\bar{\Omega}_{ej}^{(1,1)}$ between the electron and various species as a function of temperature. Let us compare the diffusion cross section $\pi\bar{\Omega}_{e-Fe}^{(1,1)}$ of e–Fe with $\pi\bar{\Omega}_{e-F}^{(1,1)}$ of e–F and $\pi\bar{\Omega}_{e-S}^{(1,1)}$ of e–S, since the high-temperature SF_6 gas mainly consists of S and F species in the temperature range of 3000 to 8000 K. The cross section $\pi\bar{\Omega}_{e-Fe}^{(1,1)}$ is much higher than those of $\pi\bar{\Omega}_{e-F}^{(1,1)}$ and $\pi\bar{\Omega}_{e-S}^{(1,1)}$. At T=5000 K, for example, $\pi\bar{\Omega}_{e-Fe}^{(1,1)}$ is 2.0×10^{-18} m^2, whilst $\pi\bar{\Omega}_{e-F}^{(1,1)}$ is 0.019×10^{-18} m^2 and $\pi\bar{\Omega}_{e-S}^{(1,1)}$ is 0.063×10^{-18} m^2.

4.2.2 Dependence of electrical resistivity of SF_6-Fe mixture on temperature and on iron vapor concentration

Substituting the derived data on N_e, N_j and $\pi\bar{\Omega}_{ej}^{(1,1)}$ into equations (4.1) and (4.2) allowed the calculation of ρ_{res}. Table 4.2 presents the thus calculated ρ_{res} of pure SF_6 plasma at 0.1 MPa for six values of T. In Table 4.2, ρ_{res} values given by Frost and Liebermann and by Chervy *et al.* are also summarized for comparison with the present calculation results [8, 9]. Note that ρ_{res} calculated by the author shows good agreement with those performed by Frost and Liebermann and by Chervy *et al.* .

Figure 4.2 shows the calculated ρ_{res} at a pressure of 0.1 MPa in the temperature range from 3000 to 8000 K. Iron vapor concentration X_{Fe} is taken as a parameter. As shown in Fig. 4.2, ρ_{res} increases significantly with a decrease in T for all values of X_{Fe}. For instance, ρ_{res} for X_{Fe} = 0.1 % rises from 0.0020 to 0.164 Ωm with a reduction of T from 6000 to 4000 K.

An increase in X_{Fe} from 0 to 0.01 % results in no variation in ρ_{res} at temperatures above 5000 K, while at temperatures below 5000 K, a rise of X_{Fe} from 0 to 0.01 % causes a slight decrease in ρ_{res}. Furthermore, an increase in X_{Fe} from 0.01 to 10 % markedly

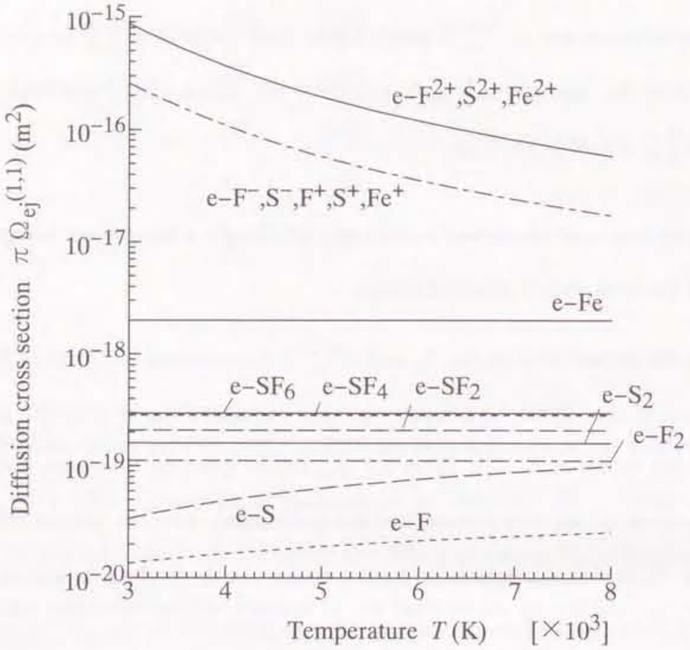

Figure 4.1. Diffusion cross sections between electron and various species at 0.1 MPa as a function of temperature. Iron vapor concentration is taken to be 0.01%.

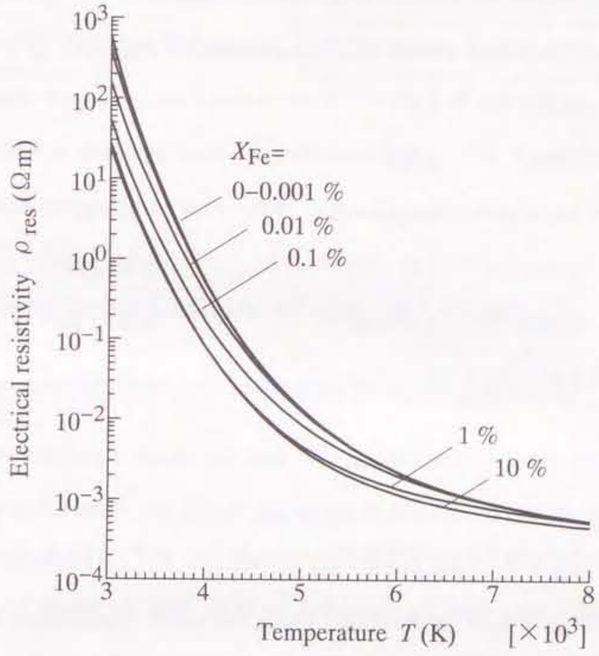

Figure 4.2. Electrical resistivity of SF_6 gas contaminated with iron vapor at 0.1 MPa as a function of temperature. Iron vapor concentration X_{Fe} is taken as a parameter.

Table 4.2. Comparison of electrical resistivity of pure SF_6 gas at 0.1MPa given by various researchers.

Temperature (K)	Electrical resistivity (Ωm)		
	The author	Frost and Liebermann [8]	Chervy *et al* [9]
3500	9.38	6.7	–
4000	0.500	0.310	0.160
5000	1.34×10^{-2}	1.20×10^{-2}	1.35×10^{-2}
6000	2.22×10^{-3}	2.67×10^{-3}	2.60×10^{-3}
7000	0.898×10^{-3}	1.16×10^{-3}	0.971×10^{-3}
8000	5.51×10^{-4}	6.73×10^{-4}	5.29×10^{-4}

reduces $\rho_{\rm res}$ at temperatures below 8000 K. For example, $\rho_{\rm res}$ at T=4000 K decreases from 0.36 to 0.080 Ωm with increasing $X_{\rm Fe}$ from 0.01 to 10 %. This reduction in $\rho_{\rm res}$ mainly results from the following mechanism. Iron has an ionization potential of 7.90 eV. This potential is much lower than that of the gas particles such as S or F (S : 10.357 eV, F : 17.42 eV) [10]. Iron is thus ionized more easily than the other gas particles. Consequently, as $X_{\rm Fe}$ rises to 10 %, the electron density increases and thus $\rho_{\rm res}$ decreases.

4.2.3 Error in theoretical calculation of electrical resistivity

In the theoretical calculation of $\rho_{\rm res}$, the diffusion cross section $\pi\bar{\Omega}^{(1,1)}_{\rm e-Fe}$ between the electron and Fe was used. The quantity $\pi\bar{\Omega}^{(1,1)}_{\rm e-Fe}$ was assumed to be 'Ramsauer cross section' in

the present dissertation. The cross section $\pi\bar{\Omega}^{(1,1)}_{\rm e-Fe}$ has an uncertainty of ±30 % [5, 6]. This uncertainty causes an uncertainty $\Delta\rho_{\rm res}$ in $\rho_{\rm res}$. Figure 4.3 shows $\Delta\rho_{\rm res}/\rho_{\rm res}$ at 0.1 MPa as a function of T with $X_{\rm Fe}$ as a parameter. The absolute value of the uncertainty $|\Delta\rho_{\rm res}/\rho_{\rm res}|$ decreases markedly with decreasing $X_{\rm Fe}$ in the temperature range from 3000 to 8000 K. For $X_{\rm Fe}$=0.01 %, $|\Delta\rho_{\rm res}/\rho_{\rm res}|$ is lower than 1.2×10^{-3} in this temperature range. For instance, $\Delta\rho_{\rm res}/\rho_{\rm res}$ was found to be $\pm5.2\times10^{-4}$ at 5000 K. $X_{\rm Fe}$ was estimated to be around 0.01% in the experiment, as indicated in Fig. 3.12. Therefore, the uncertainty in $\pi\bar{\Omega}^{(1,1)}_{\rm e-Fe}$ gives no significant uncertainty in $\rho_{\rm res}$ for estimation of $\rho_{\rm res}$ in the chamber.

4.3 Electrical resistivity of post-arc channel

4.3.1 Increase in electrical resistivity of post-arc channel

The above-mentioned theoretical data on $\rho_{\rm res}$ were used to estimate $\rho_{\rm res}$ of the post-arc channel from the measured T and $X_{\rm Fe}$ shown in Figs. 2.6 and 3.12. Figure 4.4 represents the axial distribution of the $\rho_{\rm res}$ around the current zero. The time t from current zero is taken as a parameter. From this figure, the following feature are noted.

(1) During the period from $t=-60$ to 0 μs, $\rho_{\rm res}$ values at all five observation positions increase slightly with the lapse of time, being about 0.01 Ωm.

(2) During the period from $t=0$ to 100 μs, i.e. after the current zero, $\rho_{\rm res}$'s at all the observation positions grows markedly with time. In particular, $\rho_{\rm res}$ rises very much more rapidly at the nozzle throat N than at the other observation positions. As a result, $\rho_{\rm res}$ is the highest at the nozzle throat among at the observation positions during the time from 40 to 100 μs.

(3) At 100 μs after the current zero, $\rho_{\rm res}$ at the nozzle throat increases to 4.3 Ωm which

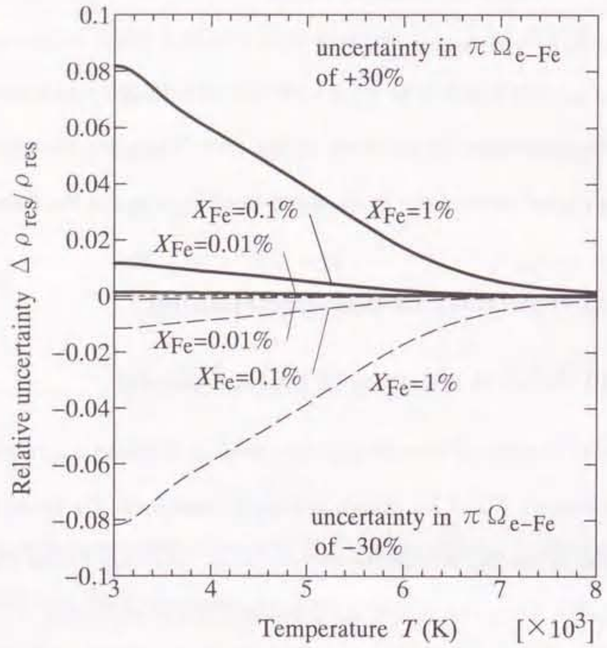

Figure 4.3. Relative uncertainty in electrical resistivity of SF_6 gas contaminated with iron vapor caused by uncertainty in $\pi\bar{\Omega}^{(1,1)}_{e-Fe}$ between electron and Fe. Total pressure is 0.1 MPa.

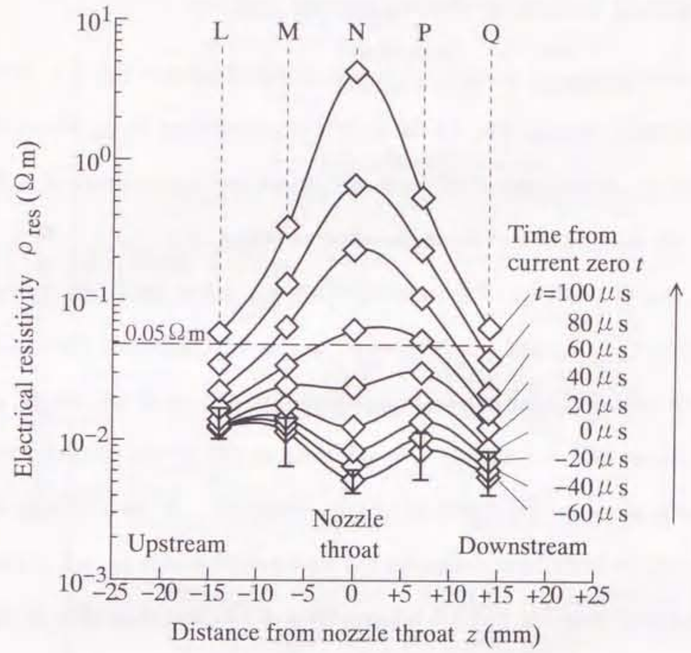

Figure 4.4. Increase aspect of axial distribution of electrical resistivity in SF_6 arc around current zero (peak value of current, 5 kA ; SF_6 gas flow rate, 50 liters min^{-1}).

is about 340 times as high as that at the current zero.

4.4 'Thermal plasma contact'

4.4.1 Opening process of 'thermal plasma contacts'

It is convenient to use the quantity 'z' to refer to the abscissa of Fig. 4.4. To explain the post-arc behavior shown in Fig. 4.4, let us take a certain value of ρ_{res}. Being able to take any value of ρ_{res} of the order of 10^{-2} Ωm, the author used a magnitude of 0.05 Ωm since adopting this value facilitated the explanation as follows :

In the case of t=+40 μs, the positions where ρ_{res} is less than 0.05 Ωm are found in Fig. 4.4 to be $z < -3.1$ and $z > +7.6$ mm. Figures 4.5 (a),(b),(c),(d) and (e) illustrate the roughly estimated positions with ρ_{res} below 0.05 Ωm at 20, 40, 60, 80 and 100 μs after the current zero respectively. The positions at 100 μs was estimated by means of extrapolation of ρ_{res} to the directions of iron electrodes. In each of these figures, the bold line with an arrow head designates the axial positions with ρ_{res} <0.05 Ωm.

The behavior shown in Fig. 4.5 is interpreted as follows : Just after an arc is extinguished at current zero, the low-ρ_{res} regions represented by the bold lines are present in the overall space between the electrodes. The low-ρ_{res} regions begin to separate at the nozzle throat around 30 μs after current zero. Fronts of the two low-ρ_{res} regions move along the direction of the nozzle axis. The gap length between the two low-ρ_{res} regions increases from 10.7 to 19.1 mm from 40 to 60 μs after the current zero. Such behavior of the low-ρ_{res} regions resembles opening behavior of contacts in a circuit breaker. Thus, it is possible to regard the low-ρ_{res} regions as the 'contacts'. The low-ρ_{res} regions are thus named 'thermal plasma contacts' in the present dissertation.

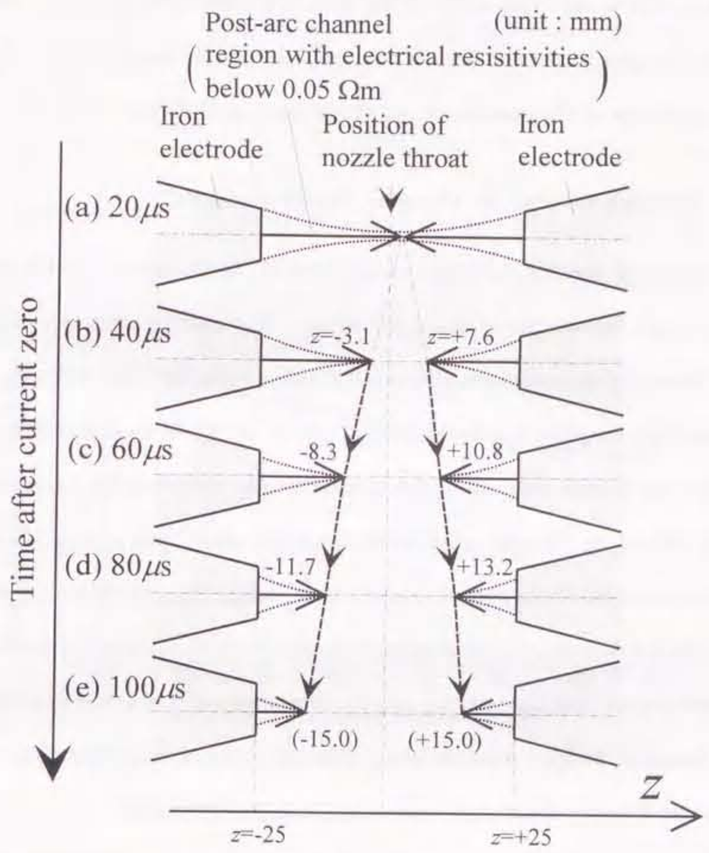

Figure 4.5. Opening process of 'thermal plasma contacts' with electrical resistivities below 0.05 Ωm in SF_6 post-arc channel.

In the above discussion, the author dealt with the behavior of thermal plasma contacts with ρ_{res}=0.05 Ωm as one example. The 'contacts' was defined by a different criterion of ρ_{res} of the order of 10^{-2} Ωm. Then, it was seen that these 'thermal plasma contacts' also keep opening after the current zero. Thus, the 'thermal plasma contacts' model described here is applicable to the case for all ρ_{res} of the order of 10^{-2} Ωm.

4.4.2 Opening velocity of 'thermal plasma contacts'

Let us define the opening velocity v of the thermal plasma contacts as the increment of the gap length between the contacts per second. The opening velocity v was estimated for the thermal plasma contacts defined as the area with ρ_{res} below 0.05 Ωm. Figure 4.6 represents time variation in the estimated v. From the figure, v exceeds 100 m s^{-1} at any time after the current zero. Next, the quantity v was estimated for the thermal plasma contacts defined by different criterion of ρ_{res} in the range from 0.01 to 0.1 Ωm. These estimations enabled the author to confirm that 'contacts' for different ρ_{res} have as high a v as that for 0.05 Ωm. It should thus be noted that the v values estimated above are very much higher than the opening velocity of mechanical contacts in practical gas-blast circuit breakers. Judging from the above discussion, the opening operation of a thermal plasma with a high velocity may achieve high current interruption.

The arc quenching chamber used in the experiment is small-scale and the post-arc channel in the quenching chamber seems to behave much more slowly than that in a practical circuit breaker. As described in chapter 2, the temperature decay rate and loss in the quenching chamber is 10^{-2} times than those in a practical circuit breaker. In spite of these facts, the opening velocity v of thermal plasma contacts in the chamber reaches more than 100 m s^{-1}. It may be found in a practical circuit breaker that there are 'thermal

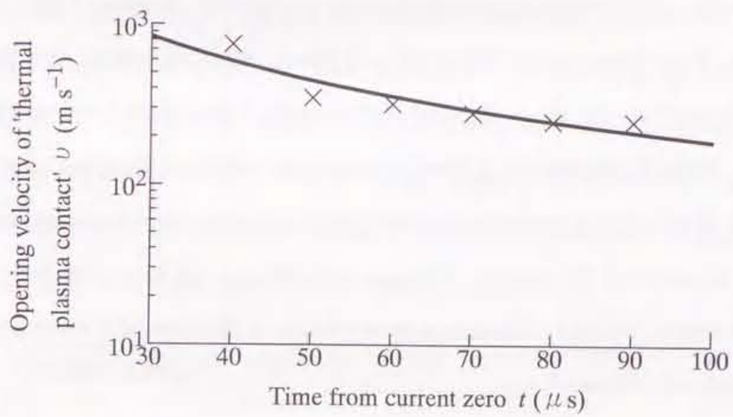

Figure 4.6. Opening velocity of 'thermal plasma-contacts' with electrical resistivities below 0.05 Ωm.

plasma contacts' opening with more rapid velocity.

4.5 Numerical simulation of behavior of thermal plasma contacts exposed to a transient recovery voltage

4.5.1 Assumptions and analysis procedure

In a practical circuit breaker, a transient recovery voltage TRV is applied between the electrodes after current zero. When rate of rise of the recovery voltage RRRV is smaller than a certain critical value, current interruption is succeeded. However, RRRV is larger than the critical value, current interruption is failed. Whether current interruption is succeed or not may depend on transient distributions of temperature and electrical resistivity. Thus, in this section, a transient axial distribution of electrical resistivity is estimated when a TRV is applied to the flat-type SF_6 gas-blast quenching chamber which attempts to interrupt the current of $5kA_{peak}$ with SF_6 gas flow rate of 50 liters min^{-1}. From the results, behavior of thermal plasma contacts in the successful interruption and thermal failure is discussed.

In this analysis, time variations in temperature T and electrical resistivity ρ_{res} in a post-arc channel was assumed to follow a simple energy balance equation :

$$\rho_m C_p \frac{\partial T}{\partial t} = \frac{E^2}{\rho_{res}} - P_{loss} \tag{4.3}$$

where ρ_m is the mass density, C_p the specific heat at constant pressure. The quantity P_{loss} is a total energy loss including a convection, conduction and radiation losses, E is electric field strength, t is time. For the sake of simplicity, one dimensional model along the nozzle axis was used in this analysis. In addition, the diameter of a post-arc channel at any position along the nozzle axis was assumed to be identical. Voltages due to a TRV

were assumed to be divided in proportion to the ρ_{res} values at each of axial positions. On the basis of these assumptions, electric field strength $E(z,t)$ was expressed as follows :

$$E(z,t) = \frac{\rho_{res}}{\int_{-25mm}^{+25mm} \rho_{res} dz} V(t) \tag{4.4}$$

where $V(t)$ is a TRV i.e. voltage applied across the iron electrodes, z the distance of nozzle throat along nozzle axis.

Equations (4.3) and (4.4) were simultaneously solved for different given TRV on the following additional assumptions : (i) local thermal equilibrium is established, (ii) total pressure is 0.1 MPa, (iii) a TRV is a ramp function which has a certain rate of rise of recovery voltage (RRRV), (iv) the initial temperature distribution is the same as that obtained in the experiment in chapter 2, (v) the current density j is identical along the nozzle axis, (vi) energy loss P_{loss} depends only on temperature, although real energy loss also does on temperature gradient, gradient of temperature gradient and flow velocity, and (vii) energy loss is the same as those estimated in chapter 2.

4.5.2 Current density

From the calculated ρ_{res} and E, post-arc current density j can be calculated through equation $j = E/\rho_{res}$. Figure 4.7 shows time variation of the post-arc current density.

Rate of rise of recovery voltage (RRRV) was taken as a parameter. In the case of RRRV=2.0 V μs^{-1}, the current density j increases with time from 0 to about 35 μs, while j decreases with the passage of time from 40 to 100 μs. Judging from such a convergent aspect of j, the author regarded that the flat chamber achieved the successful interruption in this case. On the other hand, at RRRV>2.5 V μs^{-1}, j rises exponentially with time. This case was regarded that the chamber failed to interrupt the current. This

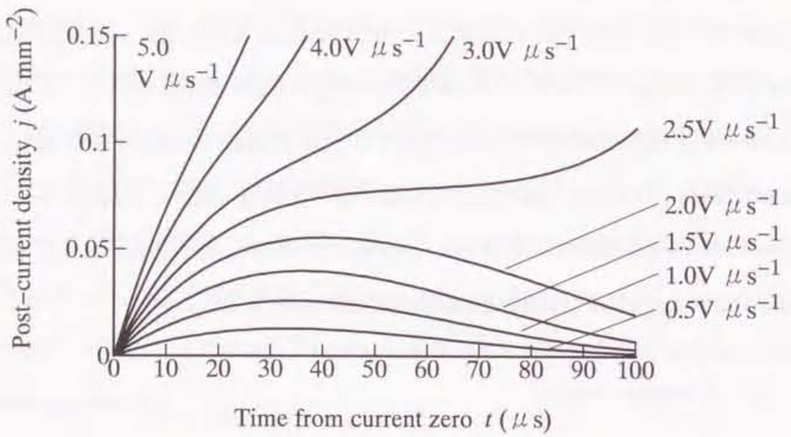

Figure 4.7. Time variation of the post-arc current density.

calculated interrupting capability was confirmed to have the same order as that derived experimentally.

4.5.3 Transient distribution of axial temperature and electrical resistivity

4.5.3.1 Case of successful interruption

Figures 4.8 and 4.9 indicate axial distributions of temperature and electrical resistivity, respectively, at a RRRV=2.0 V μs^{-1}. The temperature along the nozzle axis declines with a lapse of time. Corresponding to the temperature declines, electrical resistivity $\rho_{\rm res}$ at any positions along the nozzle axis continues to rise with time.

Following the previous section, let us regard the regions in which $\rho_{\rm res}$ is lower than 0.05 Ωm as 'thermal plasma contacts'. Figure 4.10 indicates behavior of the thermal plasma contacts. As seen in this figure, one can find that the thermal plasma contacts start opening at 20–40 μs after the current zero. At 40 μs, the distance D between the thermal plasma contacts reaches to 11.0 mm, whilst at 100 μs it reaches 25.7 mm. This represents the fact that thermal plasma contacts are formed in fronts of the electrodes and are in the opening state at least up to 100 μs after current zero. In the case that current interruption is succeeded, one can see that the thermal plasma contacts continues opening.

Figure 4.11 shows the distribution of electric potential between the electrodes at 100 μs after current zero. It should be noted that above 93% of TRV was applied between the 'thermal plasma contacts' at 100 μs after the current zero. In other words, almost all the voltage applied between the metallic electodes is applied between the 'thermal plasma contacts'.

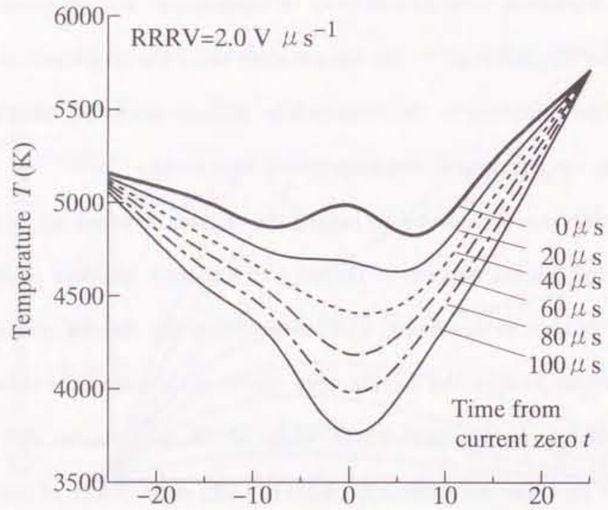

Figure 4.8. Time variation in axial temperature distribution for RRRV=2.0 V μs^{-1}.

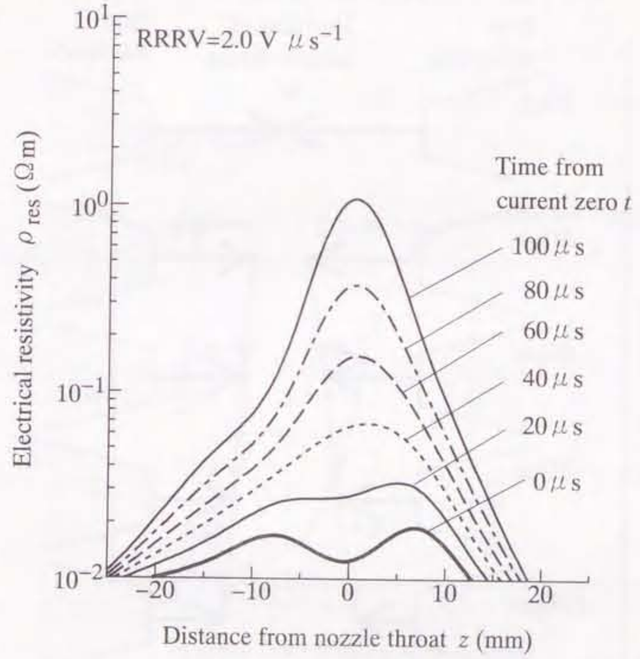

Figure 4.9. Time variation axial electrical resistivity distribution for RRRV=2.0 V μs^{-1}.

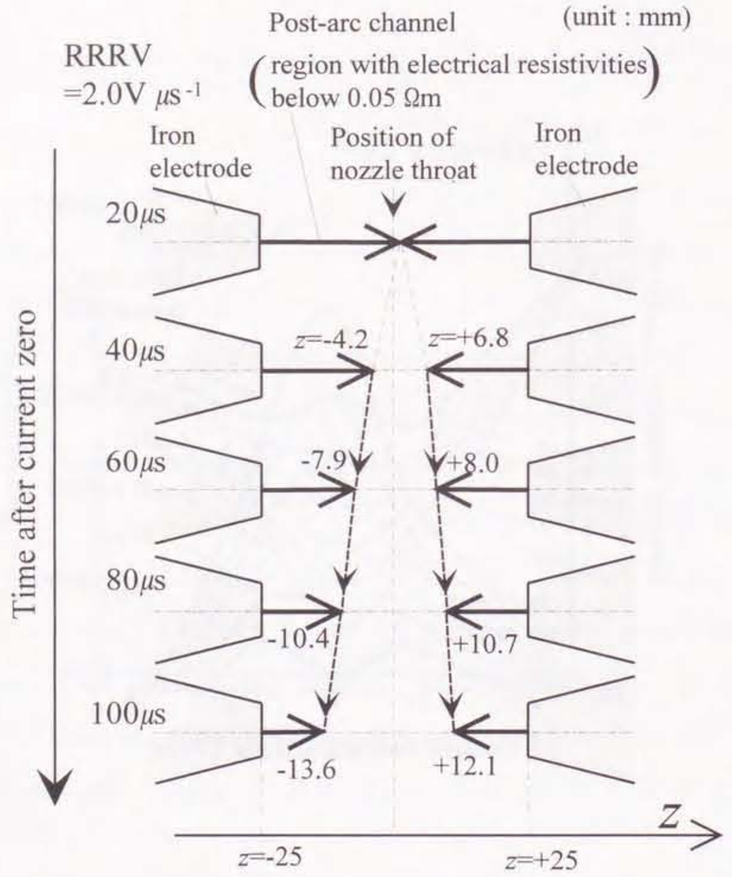

Figure 4.10. Transient aspect of thermal plasma contacts for RRRV=2.0 V μs^{-1}.

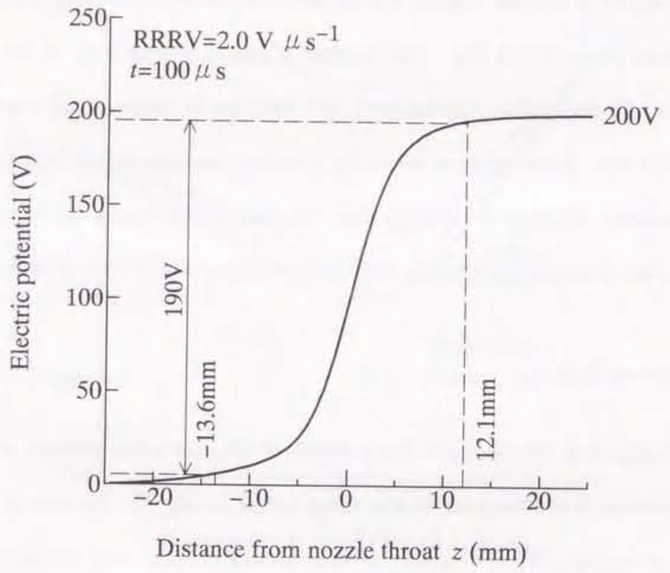

Figure 4.11. Axial distribution of electric potential at 100 μs after current zero for RRRV=2.0 V μs^{-1}.

4.5.3.2 Case of thermal failure

Figure 4.12 shows axial temperature distribution at a RRRV=3.0 V μs^{-1}. The temperature along the nozzle axis decreases with time up to 60 μs, while from 60 μs it increases dramatically. Figure 4.13 indicates the axial ρ_{res} distribution. The values ρ_{res} at any position along the nozzle axis rise with time up to 60 μs. On the other hand, they decay with time from 60 μs rapidly. Figure 4.14 shows behavior of the thermal plasma contacts defined by the value of 0.05 Ωm. The thermal plasma contacts open at 20–40 μs after current zero. At 60 μs after current zero, the distance D between the thermal plasma contacts is 9.3 mm. However, from 60 μs the thermal plasma contacts begin to close and then D decreases. At 80μs D becomes zero. As seen in this figure, the thermal plasma contacts cannot continue to separate, leading to a failure of the current interruption.

4.6 Discussion

Figure 4.15 indicates the electrical conductivity of SF_6 gas contaminated with iron vapor as a function of temperature in the range up to 20 000 K. As seen in this figure, the electrical conductivity of SF_6 gas increases almost linearly with temperatures above about 5000 K. The electrical conductivity is very much lower at temperatures below 4000 K than at temperatures above 5000 K. At temperatures of 4000–5000 K, the electrical conductivity varies remarkably with temperature. Thus, SF_6 gas is roughly regarded as an insulator at temperatures below about 4000 K and as a conductor at temperatures above about 5000 K. At temperatures of 4000–5000 K, SF_6 gas changes drastically from an insulator to a conductor. In other words, there is a boundary between insulator and conductor at temperatures of 4000–5000 K. In this temperature range, SF_6 gas has an

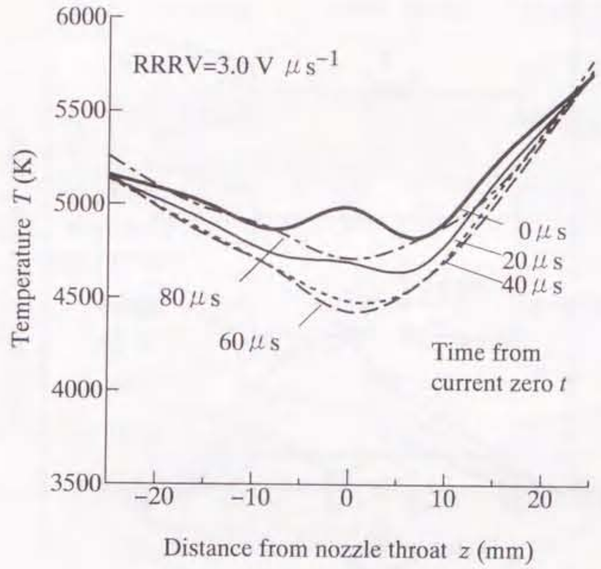

Figure 4.12. Time variation in axial temperature distribution for RRRV=3.0 V μs^{-1}.

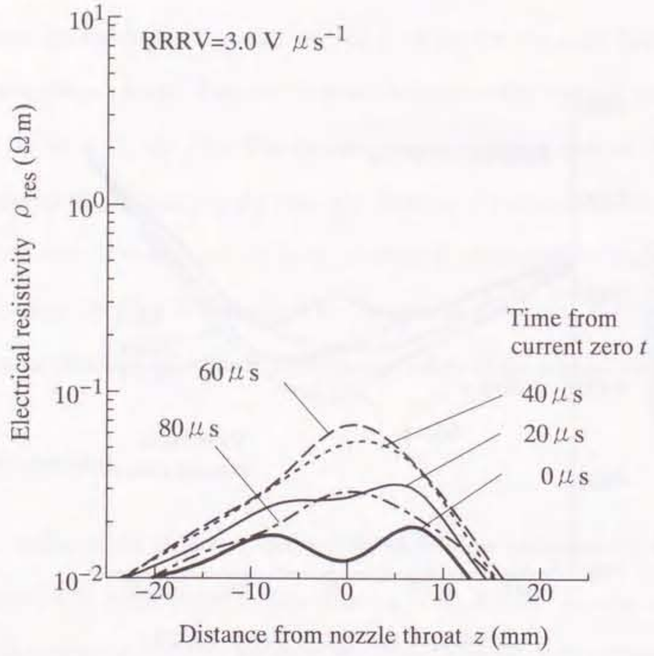

Figure 4.13. Time variation axial electrical resistivity distribution for RRRV=3.0 V μs^{-1}.

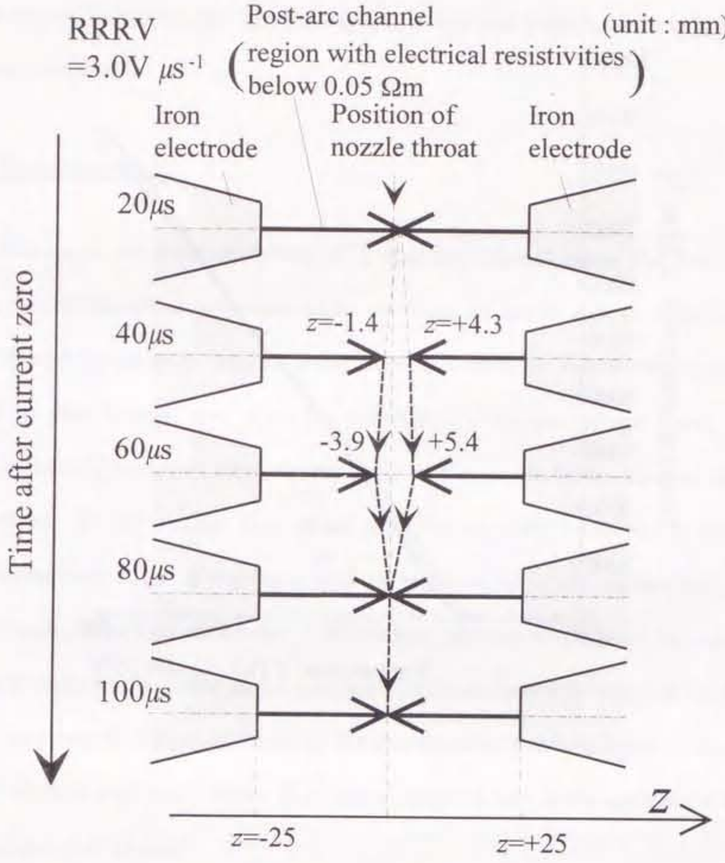

Figure 4.14. Transient aspect of thermal plasma contacts for RRRV=3.0 V μs^{-1}.

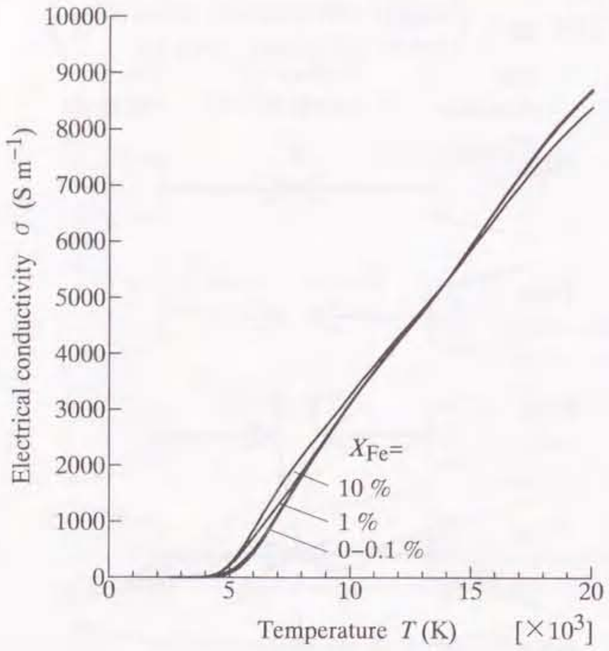

Figure 4.15. Electrical conductivity of SF_6 gas contaminated with iron vapor at 0.1 MPa as a function of temperature. Iron vapor concentration X_{Fe} is taken as a parameter.

electrical resistivity ρ_{res} of about 0.01–0.1 Ωm as shown in Fig. 4.2. On the other hand, as seen in section 4.4.1, thermal plasma contact is defined by ρ_{res} of the order of 10^{-2} Ωm. That is, thermal plasma contact is regarded as a kind of conductor. From this point of view, the author compared the opening velocity of thermal plasma contacts and that of mechanical contacts.

4.7 Conclusions

Time variations in electrical resistivity of a post-arc channel under the free recovery condition was measured at five observation positions on nozzle axis in a flat-type SF_6 gas-blast quenching chamber. The axial distribution of electrical resistivity was estimated up to 100 μs after current zero at all the observation positions. It was noted that the electrical resistivity increased more dramatically at the nozzle throat than at the other axial positions. At 100 μs after the current zero, the electrical resistivity at the nozzle throat increased to 4.3 Ωm. It was found that low electrical resistivity regions were present in front of each of the iron electrodes. The distance between the regions increased with time. This process was regarded as the opening of fictitious 'contacts' made of the thermal plasma. The opening velocity of 'thermal plasma contacts' was estimated to more than 100 m s^{-1} which is very much higher than the opening velocity of the mechanical contact in a practical circuit breaker.

The behavior of the thermal plasma contacts in the flat-type SF_6 gas-blast quenching chamber were simulated numerically in a case of application of a transient recovery voltage across the iron electrodes. If rate of rise of the recovery voltage is smaller than 2 V μs^{-1}, then post-arc current converged at zero. In this case, the thermal plasma contacts continue opening, this leading the post-current to the convergence at zero. On the other hand, rate

of rise of the recovery voltage above 3 V μs^{-1} results in impossible separation of thermal plasma contacts. These results lead to the conclusion that SF_6 gas-blast circuit breaker interrupts high current through the opening process of 'thermal plasma contacts'.

References

[1] J. M. Yos, *Transport properties of nitrogen, hydrogen, oxygen and air to 30,000 K, Technical Memorandum, RAD-TM-63-7.* Massachusetts : Research and Advanced Development Division AVCO Corporation, 1963, p.4.

[2] W. Frie, "Berechnung der Gaszusammensetzung und der Materialfunktionen von SF_6", *Z. Phys.*, Vol. 201, pp.201–294, 1967.

[3] E. J. Robinson and S. Geltman, "Single- and double photodetachment of negative ions", *Phys. Rev.*, Vol. 153, pp.4–8, 1967.

[4] S. Champan and T. G. Cowling, *The Mathematical Theory of Non-Uniform Gases.* London : Cambride University Press, 1958, ch.10, p.168.

[5] H. Maecker, "Über den Quershnitt des Fluoratoms gegenüber Elektronenstoß", *Ann. Phys., Lpz.*, Vol. 18, pp.441–446, 1956.

[6] S. Flügge, *Hundbuch der Physik.* Berlin :Springer, 1956, Vol. 22 p.380.

[7] J. M. Yos, *Transport properties of nitrogen, hydrogen, oxygen and air to 30,000 K, Technical Memorandum, RAD-TM-63-7.* Massachusetts : Research and Advanced Development Division AVCO Corporation, 1963, pp.14–5

[8] L. S. Frost and R. W. Liebermann, "Composition and transport properties of SF_6 and their use in a simplified enthalpy flow arc model", *Proc. IEEE*, Vol. 59, pp.474–485, 1971.

[9] B. Chervy, A. Gleizes and M. Razafinimanana, "Thermodynamic properties and transport coefficients in SF_6-Cu mixtures at temperatures of 300–30 000 K and pressures of 0.1–1 MPa", *J. Phys. D: Appl. Phys.*, Vol. 27, pp.1193–1206, 1994.

[10] C. E. Moore, *Atomic Energy Levels Vol.II.* Washington DC : NBS, 1952.

Chapter 5 Particle composition and electrical conductivity of high-pressure SF_6 plasma with electron temperature greater than gas temperature

5.1 Introduction

In an SF_6 gas-blast circuit breaker, detailed investigations on a post-arc channel with temperatures below 6000 K after current zero are essential for a proper understanding of current interruption process.

In chapters 2, 3 and 4, the temperature, metallic vapor concentration and electrical resistivity in post-arc channel in flat-type SF_6 gas-blast quenching chamber were measured in the case that no transient recovery voltage (TRV) was applied between the electrodes. In section 4.5 the axial distributions of temperature and electrical resistivity of the post-arc channel in the chamber were discussed in the case that TRV having rate of its rise of the order of 2 or 3 V μs^{-1} were applied between the electrodes.

However, in a practical circuit breaker, much higher transient recovery voltage (TRV) is applied between the electrodes during the time after current zero. As a result, the post-arc channel is exposed to high electric field originated from the TRV. The high electric field elevates the kinetic energy of electrons in the post-arc channel and then increases the electron temperature T_e. As a result, T_e may become higher than gas temperature T_g in the post-arc channel even at a pressure of 0.1 MPa [1]–[3]. An increase in T_e may change the properties of the post-arc channel such as particle composition, transport and thermodynamic properties from those under the condition of thermal equilibrium.

It is therefore greatly important to investigate the properties of the post-arc channel in two-temperature states where T_e is greater than T_g.

Several papers have so far dealt with the particle compositions and transport properties of Ar, H_2 or N_2 plasma in two-temperature state [3]–[6]. In the calculation of the compositions in some of the papers, multi-temperature Saha's equation (MSE) is usually adopted to express chemical equilibrium in two-temperature state. However, it has been pointed out in recent works that MSE is invalid since it is not satisfied with the second law of thermodynamics [7, 8].

In this chapter, calculations were made to obtain the particle composition and electrical conductivity of SF_6 plasma in two-temperature steady state at a pressure of 0.1MPa on the basis of the second law of thermodynamics. Firstly, in order to express the populations of the internal energy states of heavy particles, effective excitation temperature was introduced. Secondly, using the effective excitation temperature, relation equations for ionization and dissociation equilibrium in two-temperature state were induced. Thirdly, particle compositions of SF_6 plasmas in two-temperature state were theoretically calculated at a fixed T_g above 3000 K as a function of T_e. Finally, from the composition data thus derived, the author computed electrical conductivity of two-temperature SF_6 plasma, since electrical conductivity of an arc is one of the most essential properties for interrupting capability of a circuit breaker.

5.2 Particle composition of SF_6 plasma in two-temperature state

5.2.1 Equations for calculating particle composition of SF_6 plasma in two-temperature state

In the present calculation, the author assumed that SF_6 plasma is in the following conditions :

(i) The plasma is homogeneous. Although it is possible to expect the disturbance of homogeneity in the SF_6 decomposition products in practical situation, homogeneous SF_6 plasma is discussed as the fundamental approach in this dissertation.

(ii) Total pressure is 0.1 MPa.

(iii) Electrons and heavy particles have Maxwellian energy distribution functions.

(iv) Temperatures of all the heavy particles are identical to gas temperature T_g.

(v) Electron temperature T_e is greater than T_g.

(vi) The populations of the internal energy states of the heavy particles follow Boltzmann's law.

(vii) Chemical equilibrium between the particles is established.

5.2.1.1 Effective excitation temperature of heavy particle

Let the author discuss the occupations of the internal energy states of heavy particles such as atoms, molecules and ions. This is because the internal energy states of the heavy particles have great influence on chemical reactions such as ionization and dissociation.

On the basis of Boltzmann's law, the population of the internal energy states of the heavy particle 'A' is given by

$$\frac{n_{\mathrm{A}}^{(u)}}{n_{\mathrm{A}}^{(l)}} = \frac{g_u}{g_l} \exp\left(-\frac{\epsilon_u - \epsilon_l}{kT_{\mathrm{A}}^{\mathrm{ex}}}\right), \tag{5.1}$$

where the scripts u and l denote the excitation levels, g : statistical weight, ϵ : excitation potential, k : Boltzmann constant. The quantity $T_{\mathrm{A}}^{\mathrm{ex}}$ is the so-called excitation temperature of the particle 'A'. The excitation temperature is considered to be close to T_e in low-pressure and low-temperature plasmas, where the excitation of the heavy particles results mainly from collisions with electrons. However, in high-pressure and high-T_g plasmas, the excitation of the heavy particle highly seems to result from collisions not only with electrons but also with heavy particles. In such plasmas, $T_{\mathrm{A}}^{\mathrm{ex}}$ depends on both of T_e and T_g. Thus, the author will newly express $T_{\mathrm{A}}^{\mathrm{ex}}$ in terms of T_e and T_g as described below.

Figure 5.1 depicts excitation process through collisions. As seen in Fig. 5.1(a), a heavy particle 'A' obtains energy of $\frac{3}{2}kT_eK_{e\mathrm{A}}\nu_{e\mathrm{A}}$ per second through collisions with electrons in excitation process, where $K_{e\mathrm{A}}$ and $\nu_{e\mathrm{A}}$ are the collision loss factor and the collision frequency between an electron and the particle 'A', respectively. In a similar manner, as shown in Fig. 5.1 (b), the particle 'A' also acquires energy of $\sum_{j(j\neq e)}\frac{3}{2}kT_gK_{j\mathrm{A}}\nu_{j\mathrm{A}}$ per second through collisions with various kinds of heavy particles, where $K_{j\mathrm{A}}$ and $\nu_{j\mathrm{A}}$ are the collision loss factor and the collision frequency between j and 'A', respectively. As a result, total energy $E_{\mathrm{A}}^{\mathrm{rec}}$ that the particle 'A' obtains is given by

$$E_{\mathrm{A}}^{\mathrm{rec}} = \frac{3}{2}kT_eK_{e\mathrm{A}}\nu_{e\mathrm{A}} + \frac{3}{2}kT_g\sum_{j(j\neq e)}K_{j\mathrm{A}}\nu_{j\mathrm{A}}. \tag{5.2}$$

This total energy $E_{\mathrm{A}}^{\mathrm{rec}}$ determines $T_{\mathrm{A}}^{\mathrm{ex}}$ of the particle 'A'. Let us relate $E_{\mathrm{A}}^{\mathrm{rec}}$ to $T_{\mathrm{A}}^{\mathrm{ex}}$. Without distinction of electron and heavy particles colliding with 'A', they can be regarded

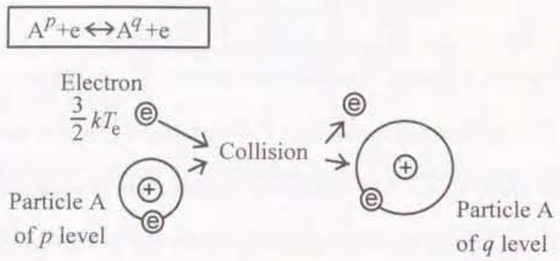

(a)Excitation process through collision with electrons

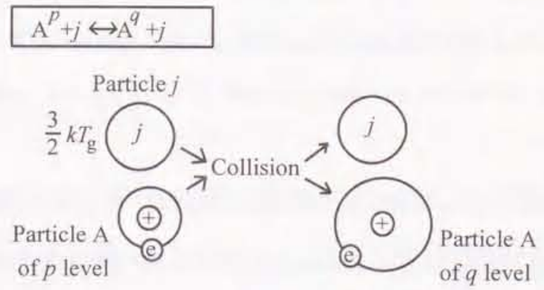

(b)Excitation process through collision with heavy particles

Figure 5.1. Excitation process of heavy particles through collisions.

as one kind of fictitious particle. Assume also that the fictitious particle has kinetic energy $\frac{3}{2}kT_{\mathrm{A}}^{\mathrm{ex}}$ and collides with 'A' with a frequency of $\nu_{\mathrm{eA}}+\sum_{j(j\neq \mathrm{e})}\nu_{j\mathrm{A}}$. The assumptions enable one to set up the following equation :

$$\frac{3}{2}kT_{\mathrm{A}}^{\mathrm{ex}}K(\nu_{\mathrm{eA}}+\sum_{j(j\neq \mathrm{e})}\nu_{j\mathrm{A}})=E_{\mathrm{A}}^{\mathrm{rec}}, \tag{5.3}$$

where K is the collision loss factor between fictitious particle and 'A'. The collision loss factors usually depend on the temperatures and species of interest. However, there have been few experimental data available on the factors so far. Then, for the sake of simplicity, it was assumed that K_{eA}, $K_{j\mathrm{A}}$ and K are the same, although this assumption is rough and results in underestimation of the effect of collision with electrons. Substituting equation (5.2) into (5.3) and rewriting equation (5.3) yields

$$T_{\mathrm{A}}^{\mathrm{ex}}=\frac{\nu_{\mathrm{eA}}T_{\mathrm{e}}+\sum_{j(j\neq \mathrm{e})}\nu_{j\mathrm{A}}T_{\mathrm{g}}}{\nu_{\mathrm{eA}}+\sum_{j(j\neq \mathrm{e})}\nu_{j\mathrm{A}}}. \tag{5.4}$$

This equation expressing $T_{\mathrm{A}}^{\mathrm{ex}}$ in terms of T_{e} and T_{g} is newly proposed in this dissertation. The author named $T_{\mathrm{A}}^{\mathrm{ex}}$ as "effective excitation temperature". The effective excitation temperature greatly affects chemical reactions, as will be shown later.

The collision frequencies ν_{eA} and $\nu_{j\mathrm{A}}$ can be estimated by

$$\nu_{\mathrm{eA}}=N_{\mathrm{e}}\bar{Q}_{\mathrm{eA}}(T_{\mathrm{e}})\bar{v}_{\mathrm{e}} \tag{5.5}$$

$$\nu_{j\mathrm{A}}=N_j\bar{Q}_{j\mathrm{A}}(T_{\mathrm{g}})\bar{v}_{j\mathrm{A}} \tag{5.6}$$

$$\bar{v}_{\mathrm{e}}=\left(\frac{8kT_{\mathrm{e}}}{\pi m_{\mathrm{e}}}\right)^{\frac{1}{2}} \tag{5.7}$$

$$\bar{v}_{j\mathrm{A}}=\left(\frac{8kT_{\mathrm{g}}(m_j+m_{\mathrm{A}})}{\pi m_j m_{\mathrm{A}}}\right)^{\frac{1}{2}}, \tag{5.8}$$

where m_{e} and m_j are the mass of the electron and of species j respectively, $\bar{Q}_{\mathrm{eA}}$ and $\bar{Q}_{j\mathrm{A}}$ are the collision cross section between the electron and species A and that between species

j and A respectively. In this dissertation, the author used the diffusion cross sections as $\bar{Q}_{eA}$ and $\bar{Q}_{jA}$ as follows.

(i) **Neutral molecule-neutral molecule interaction.** The cross section between neutral molecules were obtained by the hard-sphere method using the radii of the molecules.

(ii) **Neutral atom-neutral atom interaction.** For interaction of F–F and S–S, Abrahamson has given the parameters of Born-Mayor-Type interatomic potential for ground state [9]. Using the parameters, the diffusion cross sections of F–F and S–S were obtained through the table given by Monchick [10]. For interaction of F–S, the cross section was calculated on the basis of empirical combining law [11].

(iii) **Neutral particle-charged particle interaction.** The diffusion cross sections of F–F^+, F–F^-, S–S^+, S–S^-, F_2–F_2^+ and S_2–S_2^+ were obtained considering the effect of resonant charge exchange [12]. For the cross sections between neutral particle and charged particles except above, it was assumed that they coincide with that for neutral-neutral interactions.

(iv) **Electron-neutral interaction.** The cross sections between the electron and neutral molecule were calculated by the hard-sphere method. For the interaction of e–F and e–S, Robinson and Geltman have calculated the elastic cross sections as a function of kinetic energy of electron [13]. From these data, the diffusion cross sections of e–F and e–S were calculated as a function of temperature in accordance with the method given by Chapman and Cowling [14].

(v) **Interaction between charged particles.** The cross sections between charged particles were calculated from Gvosdover cross section for Coulomb potential [15].

5.2.1.2 Equations for chemical equilibrium in two-temperature state

Table 5.1 indicates ten dissociation and ten ionization equilibrium reactions taken into account in the present calculation. The magnitude of dissociation and ionization potentials are also listed in this table [16]–[18]. Equations for the reactions will be derived below.

5.2.1.2.1 Ionization equilibrium Let us discuss the ionization equilibrium in two-temperature state :

$$A + M \rightleftharpoons A^+ + e^- + M, \tag{5.9}$$

where M is an electron or a heavy particle colliding with 'A'. For this ionization equilibrium, the following expression is established on the basis of the second law of thermodynamics [7, 8] :

$$\frac{\mu_A}{T_g} + \frac{\mu_M}{T_M} = \frac{\mu_{A^+}}{T_g} + \frac{\mu_e}{T_e} + \frac{\mu_M}{T_M}, \tag{5.10}$$

where the temperature T_M of M is T_e when M is an electron, while T_M is T_g when M is a heavy particle. Also, μ_x(x=e, A, A^+ or M) is the chemical potential of each species. Using this relationship, the author will introduce the basic equation expressing ionization equilibrium in two-temperature state.

The chemical potential μ_x is expressed in terms of partition function U_x, number density N_x and volume of plasma V :

$$\frac{\mu_x}{T_x} = -k \ln\left(\frac{U_x}{N_x V}\right). \tag{5.11}$$

Special attention was paid to the partition function of 'A^+'. The partition function of A^+ with reference to the ground state of 'A' is expressed as $U_{A^+} \times \exp[-(E_A - \Delta E)/kT_A^{ex}]$, where E_A is the ionization potential of 'A' and ΔE represents a lowering of ionization potential. This is because the populations of the excited states of 'A' follow Boltzmann

Table 5.1. Chemical reactions taken into account in the calculation. 'M' indicates an electron or a heavy particle.

SF_6	$+M \rightleftharpoons$	$SF_5 + F$	$+M$	(4.00 eV[16])
SF_5	$+M \rightleftharpoons$	$SF_4 + F$	$+M$	(2.27 eV[16])
SF_4	$+M \rightleftharpoons$	$SF_3 + F$	$+M$	(3.47 eV[16])
SF_3	$+M \rightleftharpoons$	$SF_2 + F$	$+M$	(2.92 eV[16])
SF_2	$+M \rightleftharpoons$	$SF + F$	$+M$	(4.01 eV[16])
SF	$+M \rightleftharpoons$	$S + F$	$+M$	(3.52 eV[16])
SSF_2	$+M \rightleftharpoons$	$SF_2 + S$	$+M$	(3.90 eV[16])
FSSF	$+M \rightleftharpoons$	$SF + SF$	$+M$	(3.71 eV[16])
F_2	$+M \rightleftharpoons$	$F + F$	$+M$	(1.60 eV[16])
S_2	$+M \rightleftharpoons$	$S + S$	$+M$	(4.37 eV[16])
F^-	$+M \rightleftharpoons$	$F + e^-$	$+M$	(3.40 eV[16])
S^-	$+M \rightleftharpoons$	$S + e^-$	$+M$	(2.08 eV[16])
F	$+M \rightleftharpoons$	$F^+ + e^-$	$+M$	(17.4 eV[17])
S	$+M \rightleftharpoons$	$S^+ + e^-$	$+M$	(10.4 eV[17])
F^+	$+M \rightleftharpoons$	$F^{2+} + e^-$	$+M$	(35.6 eV[17])
S^+	$+M \rightleftharpoons$	$S^{2+} + e^-$	$+M$	(23.4 eV[17])
F_2	$+M \rightleftharpoons$	$F_2^+ + e^-$	$+M$	(15.8 eV[18])
S_2	$+M \rightleftharpoons$	$S_2^+ + e^-$	$+M$	(8.30 eV[18])
SF	$+M \rightleftharpoons$	$SF^+ + e^-$	$+M$	(10.1 eV[18])
SF^-	$+M \rightleftharpoons$	$SF + e^-$	$+M$	(2.10 eV[16])

law for the temperature of T_A^{ex}. By substituting equation (5.11) into (5.10), the author gets

$$\frac{N_e N_{A^+}}{N_A} = \frac{U_e U_{A^+}}{U_A V} \exp\left(-\frac{E_A - \Delta E}{kT_A^{ex}}\right), \tag{5.12}$$

$$\Delta E \ [\mathrm{eV}] = 6.96 \times 10^{-9} (N_e[\mathrm{m}^{-3}])^{\frac{1}{3}}. \tag{5.13}$$

For the derivation of number densities through equation (5.12), the calculation of partition functions U_A, U_{A^+} and U_e is necessary. The author will therefore discuss the dependence of the partition functions on T_e, T_g and T_A^{ex} as follows.

(1) **Partition function for electron U_e.** Translational motions of electrons depend only on T_e, because T_e indicates the kinetic energy of electrons. Thus, U_e in two-temperature state is expressed as a function of T_e :

$$U_e = 2U_e^{tr} = 2V\left(\frac{2\pi m_e k T_e}{h^2}\right)^{\frac{3}{2}}, \tag{5.14}$$

where U_e^{tr} is the translational partition function of the electron, h is Planck's constant and m_e is the mass of an electron.

(2) **Partition function for heavy particle U_A and U_{A^+}.** Heavy particles have three energy states : translational, rotational–vibrational and electronic states. Translational motions of heavy particles depend on T_g. Translational partition function U_A^{tr} is thus calculated using T_g :

$$U_A^{tr} = V\left(\frac{2\pi m_A k T_g}{h^2}\right)^{\frac{3}{2}}. \tag{5.15}$$

The author assumed that rotational–vibrational motions of heavy particles depend on T_g, because these motions are due to the kinetic motions. In this case, rotational–vibrational partition function U_A^{rv} is written by

$$U_A^{rv} = U_A^{rv}(T_g). \tag{5.16}$$

The partition functions $U_{\mathrm{A}}^{\mathrm{rv}}$ for diatomic molecules and for polyatomic molecules were calculated in accordance with the methods suggested by Burhorn [19] and Herzberg [20]. On the other hand, since the internal energy state of 'A' is governed by $T_{\mathrm{A}}^{\mathrm{ex}}$, electronic partition function $U_{\mathrm{A}}^{\mathrm{ele}}$ is obtained as a function of $T_{\mathrm{A}}^{\mathrm{ex}}$:

$$U_{\mathrm{A}}^{\mathrm{ele}} = U_{\mathrm{A}}^{\mathrm{ele}}(T_{\mathrm{A}}^{\mathrm{ex}}) = \sum_{\mathrm{i}} g_i \exp\left(-\frac{\epsilon_i}{kT_{\mathrm{A}}^{\mathrm{ex}}}\right), \tag{5.17}$$

where g_i and ϵ_i are statistical weight and excitation potential, respectively. These values are given by Chase *et al.* for polyatomic molecules [16], by Herzberg for diatomic molecules [18] and by Moore for monatomic particles [17]. Use of equations (5.15), (5.16) and (5.17) induces one to have

$$U_{\mathrm{A}} = V\left(\frac{2\pi m_{\mathrm{A}} kT_{\mathrm{g}}}{h^2}\right)^{\frac{3}{2}} U_{\mathrm{A}}^{\mathrm{rv}}(T_{\mathrm{g}}) U_{\mathrm{A}}^{\mathrm{ele}}(T_{\mathrm{A}}^{\mathrm{ex}}). \tag{5.18}$$

In a similar manner, the partition function for the ion 'A^+' can be expressed as

$$U_{\mathrm{A}^+} = V\left(\frac{2\pi m_{\mathrm{A}^+} kT_{\mathrm{g}}}{h^2}\right)^{\frac{3}{2}} U_{\mathrm{A}^+}^{\mathrm{rv}}(T_{\mathrm{g}}) U_{\mathrm{A}^+}^{\mathrm{ele}}(T_{\mathrm{A}^+}^{\mathrm{ex}}). \tag{5.19}$$

Finally, substitution of equations (5.14), (5.18) and equation (5.19) into (5.12) yields an expression :

$$\begin{aligned}\frac{N_{\mathrm{e}} N_{\mathrm{A}^+}}{N_{\mathrm{A}}} &= 2\left(\frac{2\pi m_{\mathrm{e}} kT_{\mathrm{e}}}{h^2}\right)^{\frac{3}{2}} \frac{U_{\mathrm{A}^+}^{\mathrm{rv}}(T_{\mathrm{g}}) U_{\mathrm{A}^+}^{\mathrm{ele}}(T_{\mathrm{A}^+}^{\mathrm{ex}})}{U_{\mathrm{A}}^{\mathrm{rv}}(T_{\mathrm{g}}) U_{\mathrm{A}}^{\mathrm{ele}}(T_{\mathrm{A}}^{\mathrm{ex}})} \\ &\times \exp\left(-\frac{E_{\mathrm{A}} - \Delta E}{kT_{\mathrm{A}}^{\mathrm{ex}}}\right)\end{aligned} \tag{5.20}$$

This is the equation that the author newly developed for ionization equilibrium in two-temperature state. Note that equation (5.20) includes the effective excitation temperature. Equation (5.20) was applied to express each of ten ionization equilibrium shown in Table 5.1.

5.2.1.2.2 Dissociation equilibrium Let us discuss the following dissociation equilibrium :

$$\mathrm{A} + \mathrm{M} \rightleftharpoons \mathrm{B} + \mathrm{C} + \mathrm{M}, \tag{5.21}$$

where A is a molecule, B and C are heavy particles, and M is an electron or a heavy particle. In a similar way as the procedure for deriving (5.20), the following expression can be obtained

$$\begin{aligned}\frac{N_{\mathrm{B}} N_{\mathrm{C}}}{N_{\mathrm{A}}} &= \left(\frac{2\pi m_{\mathrm{B}} m_{\mathrm{C}} kT_{\mathrm{g}}}{m_{\mathrm{A}} h^2}\right)^{\frac{3}{2}} \\ &\times \frac{U_{\mathrm{B}}^{\mathrm{rv}}(T_{\mathrm{g}}) U_{\mathrm{C}}^{\mathrm{rv}}(T_{\mathrm{g}})}{U_{\mathrm{A}}^{\mathrm{rv}}(T_{\mathrm{g}})} \frac{U_{\mathrm{B}}^{\mathrm{ele}}(T_{\mathrm{B}}^{\mathrm{ex}}) U_{\mathrm{C}}^{\mathrm{ele}}(T_{\mathrm{C}}^{\mathrm{ex}})}{U_{\mathrm{A}}^{\mathrm{ele}}(T_{\mathrm{A}}^{\mathrm{ex}})} \\ &\times \exp\left(-\frac{E_{\mathrm{A}}^{\mathrm{d}}}{kT_{\mathrm{A}}^{\mathrm{ex}}}\right),\end{aligned} \tag{5.22}$$

where $E_{\mathrm{A}}^{\mathrm{d}}$ is the dissociation potential of 'A'. Above expression was adopted to express each of dissociation equilibrium shown in Table 5.1.

5.2.1.3 Other governing equations for two-temperature plasma

Besides the above-mentioned equations (5.20) and (5.22), three equations for Dalton's law of partial pressure, charge neutrality and conservation law of stoichiometric equilibrium were set up. The equation for Dalton's law in two-temperature state is written by

$$P + \Delta P = N_{\mathrm{e}} kT_{\mathrm{e}} + \sum_{j(j\neq \mathrm{e})} N_j kT_{\mathrm{g}}, \tag{5.23}$$

$$\Delta P = \frac{kT_{\mathrm{e}}}{24\pi}\left[\frac{e^2}{\varepsilon_0}\left(\frac{N_{\mathrm{e}}}{kT_{\mathrm{e}}} + \sum_{j(j\neq \mathrm{e})} \frac{z_{\mathrm{eff}\,j}^2 N_j}{kT_{\mathrm{g}}}\right)\right]^{\frac{3}{2}}, \tag{5.24}$$

where P is the total pressure, ΔP the pressure correction term resulting from the electrostatic interactions [21], $z_{\mathrm{eff}\,j}$ the effective charge number, ε_0 the permittivity of vacuum, e the electronic charge.

5.2.2 Calculation procedure

Table 5.2 summarizes the governing equation for calculating the particle composition of two-temperature SF_6 plasmas. These twenty three simultaneous equations were solved through following procedures :

(i) T_e and T_g are given.

(ii) Initial values of number densities N_j of each of species are given.

(iii) T_j^{ex} is derived using equation (5.4) and ΔE is also calculated by equation (5.13).

(iv) The obtained T_j^{ex} and ΔE are substituted into twenty simultaneous equations for ionization and dissociation equilibrium corresponding to equations (5.20) and (5.22).

(v) All of twenty-three simultaneous equations are solved using Newton-Raphson method to newly derive number densities N_j.

(vi) Procedures of (iii)–(v) are iterated until T_j^{ex} and ΔE converge.

5.2.3 Calculation results

Figure 5.2 shows the calculated particle composition of SF_6 plasma as a function of T_e at fixed T_g =3000 K. The composition at T_e=3000 K corresponds to that under the condition of thermal equilibrium at 3000 K. An increase in T_e from 3000 to 20 000 K brings about the little change in the composition. Figure 5.3 shows the derived T_j^{ex} of each of the heavy particles as a function of T_e under the same condition as that on Fig. 5.2. All of T_j^{ex} almost equal T_g. The results shown in Figs 5.2 and 5.3 arise from the following fact : At T_g = 3000 K, the electron density N_e is as low as of the order of 10^{17} m^{-3}. Thus, collision frequencies between heavy particles and electrons are very much lower

Table 5.2. Equations for calculating particle composition of two-temperature SF_6 plasmas.

$$\frac{N_{SF_5}N_F}{N_{SF_6}} = \left(\frac{2\pi m_{SF_5} m_F kT_g}{m_{SF_6}h^2}\right)^{\frac{3}{2}} \frac{U^{tv}_{SF_5}(T_g)U^{ele}_F(T^{ex}_F)}{U^{tv}_{SF_6}(T_g)} \exp\left(-\frac{E^d_{SF_6}}{kT^{ex}_{SF_6}}\right) \tag{5.25}$$

$$\frac{N_{SF_4}N_F}{N_{SF_5}} = \left(\frac{2\pi m_{SF_4} m_F kT_g}{m_{SF_5}h^2}\right)^{\frac{3}{2}} \frac{U^{tv}_{SF_4}(T_g)U^{ele}_F(T^{ex}_F)}{U^{tv}_{SF_5}(T_g)} \exp\left(-\frac{E^d_{SF_5}}{kT^{ex}_{SF_5}}\right) \tag{5.26}$$

$$\frac{N_{SF_3}N_F}{N_{SF_4}} = \left(\frac{2\pi m_{SF_3} m_F kT_g}{m_{SF_4}h^2}\right)^{\frac{3}{2}} \frac{U^{tv}_{SF_3}(T_g)U^{ele}_F(T^{ex}_F)}{U^{tv}_{SF_4}(T_g)} \exp\left(-\frac{E^d_{SF_4}}{kT^{ex}_{SF_4}}\right) \tag{5.27}$$

$$\frac{N_{SF_2}N_F}{N_{SF_3}} = \left(\frac{2\pi m_{SF_2} m_F kT_g}{m_{SF_3}h^2}\right)^{\frac{3}{2}} \frac{U^{tv}_{SF_2}(T_g)U^{ele}_F(T^{ex}_F)}{U^{tv}_{SF_3}(T_g)} \exp\left(-\frac{E^d_{SF_3}}{kT^{ex}_{SF_3}}\right) \tag{5.28}$$

$$\frac{N_{SF}N_F}{N_{SF_2}} = \left(\frac{2\pi m_{SF} m_F kT_g}{m_{SF_2}h^2}\right)^{\frac{3}{2}} \frac{U^{tv}_{SF}(T_g)U^{ele}_{SF}(T^{ex}_{SF})U^{ele}_F(T^{ex}_F)}{U^{tv}_{SF_2}(T_g)} \exp\left(-\frac{E^d_{SF_2}}{kT^{ex}_{SF_2}}\right) \tag{5.29}$$

$$\frac{N_S N_F}{N_{SF}} = \left(\frac{2\pi m_S m_F kT_g}{m_{SF}h^2}\right)^{\frac{3}{2}} \frac{U^{ele}_S(T^{ex}_S)U^{ele}_F(T^{ex}_F)}{U^{tv}_{SF}(T_g)U^{ele}_{SF}(T^{ex}_{SF})} \exp\left(-\frac{E^d_{SF}}{kT^{ex}_{SF}}\right) \tag{5.30}$$

$$\frac{N_{SF_2}N_S}{N_{SSF_2}} = \left(\frac{2\pi m_{SF_2} m_S kT_g}{m_{SSF_2}h^2}\right)^{\frac{3}{2}} \frac{U^{tv}_{SF_2}(T_g)U^{ele}_S(T^{ex}_S)}{U^{tv}_{SSF_2}(T_g)} \exp\left(-\frac{E^d_{SSF_2}}{kT^{ex}_{SSF_2}}\right) \tag{5.31}$$

$$\frac{N^2_{SF}}{N_{FSSF}} = \left(\frac{2\pi m^2_{SF} kT_g}{m_{FSSF}h^2}\right)^{\frac{3}{2}} \frac{[U^{tv}_{SF}(T_g)U^{ele}_{SF}(T^{ex}_{SF})]^2}{U^{tv}_{FSSF}(T_g)} \exp\left(-\frac{E^d_{FSSF}}{kT^{ex}_{FSSF}}\right) \tag{5.32}$$

$$\frac{N^2_F}{N_{F_2}} = \left(\frac{\pi m_F kT_g}{h^2}\right)^{\frac{3}{2}} \frac{[U^{ele}_F(T^{ex}_F)]^2}{U^{tv}_{F_2}(T_g)U^{ele}_{F_2}(T^{ex}_{F_2})} \exp\left(-\frac{E^d_{F_2}}{kT^{ex}_{F_2}}\right) \tag{5.33}$$

$$\frac{N^2_S}{N_{S_2}} = \left(\frac{\pi m_S kT_g}{h^2}\right)^{\frac{3}{2}} \frac{[U^{ele}_S(T^{ex}_S)]^2}{U^{tv}_{S_2}(T_g)U^{ele}_{S_2}(T^{ex}_{S_2})} \exp\left(-\frac{E^d_{S_2}}{kT^{ex}_{S_2}}\right) \tag{5.34}$$

$$\frac{N_F N_e}{N_{F^-}} = \left(\frac{2\pi m_e kT_e}{h^2}\right)^{\frac{3}{2}} \frac{2U^{ele}_F(T^{ex}_F)}{U^{ele}_{F^-}(T^{ex}_{F^-})} \exp\left(-\frac{E_{F^-} - \Delta E}{kT^{ex}_{F^-}}\right) \tag{5.35}$$

$$\frac{N_S N_e}{N_{S^-}} = \left(\frac{2\pi m_e kT_e}{h^2}\right)^{\frac{3}{2}} \frac{2U^{ele}_S(T^{ex}_S)}{U^{ele}_{S^-}(T^{ex}_{S^-})} \exp\left(-\frac{E_{S^-} - \Delta E}{kT^{ex}_{S^-}}\right) \tag{5.36}$$

$$\frac{N_{F^+} N_e}{N_F} = \left(\frac{2\pi m_e kT_e}{h^2}\right)^{\frac{3}{2}} \frac{2U^{ele}_{F^+}(T^{ex}_{F^+})}{U^{ele}_F(T^{ex}_F)} \exp\left(-\frac{E_F - \Delta E}{kT^{ex}_F}\right) \tag{5.37}$$

$$\frac{N_{S^+} N_e}{N_S} = \left(\frac{2\pi m_e kT_e}{h^2}\right)^{\frac{3}{2}} \frac{2U^{ele}_{S^+}(T^{ex}_{S^+})}{U^{ele}_S(T^{ex}_S)} \exp\left(-\frac{E_S - \Delta E}{kT^{ex}_S}\right) \tag{5.38}$$

Table 5.2. Equaitons for calculating particle composition of two-temperature SF_6 plasmas (*continued*).

$$\frac{N_{F^{2+}}N_e}{N_{F^+}} = \left(\frac{2\pi m_e kT_e}{h^2}\right)^{\frac{3}{2}} \frac{2U^{ele}_{F^{2+}}(T^{ex}_{F^{2+}})}{U^{ele}_{F^+}(T^{ex}_{F^+})} \exp\left(-\frac{E_{F^+} - \Delta E}{kT^{ex}_{F^+}}\right) \tag{5.39}$$

$$\frac{N_{S^{2+}}N_e}{N_{S^+}} = \left(\frac{2\pi m_e kT_e}{h^2}\right)^{\frac{3}{2}} \frac{2U^{ele}_{S^{2+}}(T^{ex}_{S^{2+}})}{U^{ele}_{S^+}(T^{ex}_{S^+})} \exp\left(-\frac{E_{S^+} - \Delta E}{kT^{ex}_{S^+}}\right) \tag{5.40}$$

$$\frac{N_{F_2^+}N_e}{N_{F_2}} = \left(\frac{2\pi m_e kT_e}{h^2}\right)^{\frac{3}{2}} \frac{2U^{rv}_{F_2^+}(T_g)U^{ele}_{F_2^+}(T^{ex}_{F_2^+})}{U^{rv}_{F_2}(T_g)U^{ele}_{F_2}(T^{ex}_{F_2})} \exp\left(-\frac{E_{F_2} - \Delta E}{kT^{ex}_{F_2}}\right) \tag{5.41}$$

$$\frac{N_{S_2^+}N_e}{N_{S_2}} = \left(\frac{2\pi m_e kT_e}{h^2}\right)^{\frac{3}{2}} \frac{2U^{rv}_{S_2^+}(T_g)U^{ele}_{S_2^+}(T^{ex}_{S_2^+})}{U^{rv}_{S_2}(T_g)U^{ele}_{S_2}(T^{ex}_{S_2})} \exp\left(-\frac{E_{S_2} - \Delta E}{kT^{ex}_{S_2}}\right) \tag{5.42}$$

$$\frac{N_{SF^+}N_e}{N_{SF}} = \left(\frac{2\pi m_e kT_e}{h^2}\right)^{\frac{3}{2}} \frac{2U^{rv}_{SF^+}(T_g)U^{ele}_{SF^+}(T^{ex}_{SF^+})}{U^{rv}_{SF}(T_g)U^{ele}_{SF}(T^{ex}_{SF})} \exp\left(-\frac{E_{SF} - \Delta E}{kT^{ex}_{SF}}\right) \tag{5.43}$$

$$\frac{N_{SF}N_e}{N_{SF^-}} = \left(\frac{2\pi m_e kT_e}{h^2}\right)^{\frac{3}{2}} \frac{2U^{rv}_{SF}(T_g)U^{ele}_{SF}(T^{ex}_{SF})}{U^{rv}_{SF^-}(T_g)U^{ele}_{SF^-}(T^{ex}_{SF^-})} \exp\left(-\frac{E_{SF^-} - \Delta E}{kT^{ex}_{SF^-}}\right) \tag{5.44}$$

$$N_F/N_S = 6 \tag{5.45}$$

$$\begin{aligned} N_F &= 6N_{SF_6} + 5N_{SF_5} + 4N_{SF_4} + 3N_{SF_3} + 2N_{SF_2} + N_{SF} + 2N_{SSF_2} \\ &+ 2N_{FSSF} + 2N_{F_2} + N_F + N_{F^-} + N_{F^+} \\ &+ N_{F^{2+}} + 2N_{F_2^+} + N_{SF^-} + N_{SF^+} \end{aligned}$$

$$\begin{aligned} N_S &= N_{SF_6} + N_{SF_5} + N_{SF_4} + N_{SF_3} + N_{SF_2} + N_{SF} + 2N_{SSF_2} + 2N_{FSSF} \\ &+ 2N_{S_2} + N_S + N_{S^-} + N_{S^+} + N_{S^{2+}} \\ &+ 2N_{S_2^+} + N_{SF^-} + N_{SF^+} \end{aligned}$$

$$N_{F^-} + N_{S^-} + N_{SF^-} + N_e = N_{F^+} + N_{S^+} + 2N_{F^{2+}} + 2N_{S^{2+}} + N_{F_2^+} + N_{S_2^+} + N_{SF^+} \tag{5.46}$$

$$P + \Delta P = N_e kT_e + \sum_{j(j\neq e)} N_j kT_g \tag{5.47}$$

$$\Delta P = \frac{kT_e}{24\pi\lambda_D^3}$$

Table 5.2. Equaitons for calculating particle composition of two-temperature SF_6 plasmas (*continued*).

$$\frac{1}{\lambda_D^2} = \frac{e^2}{\varepsilon_0}\left(\frac{N_e}{kT_e} + \sum_{j(j\neq e)} \frac{z^2_{eff\,j}N_j}{kT_g}\right)$$

$$\Delta E[\text{eV}] = 6.96 \times 10^{-9} N_e^{\frac{1}{3}} \tag{5.48}$$

$$T_j^{ex} = \frac{\nu_{ej}T_e + \sum_{i(i\neq e)} \nu_{ij}T_g}{\nu_{ej} + \sum_{i(i\neq e)} \nu_{ij}} \quad (j = 1, 2, \cdots, 22) \tag{5.49}$$

where T_g the gas temperature, T_e the electron temperature, N_i the number density, U_i^{rv} the rotational-vibrational partition function, U_i^{ele} the internal electronic partition function, E_i the dissociation or ionisation potential, m_i the mass of species i $z_{eff\,i}$ the effective ionic charge of species i, h Planck's constant, k : Boltzmann's constant, e the electronic charge, ε_0 the dielectric constant of a vacuum

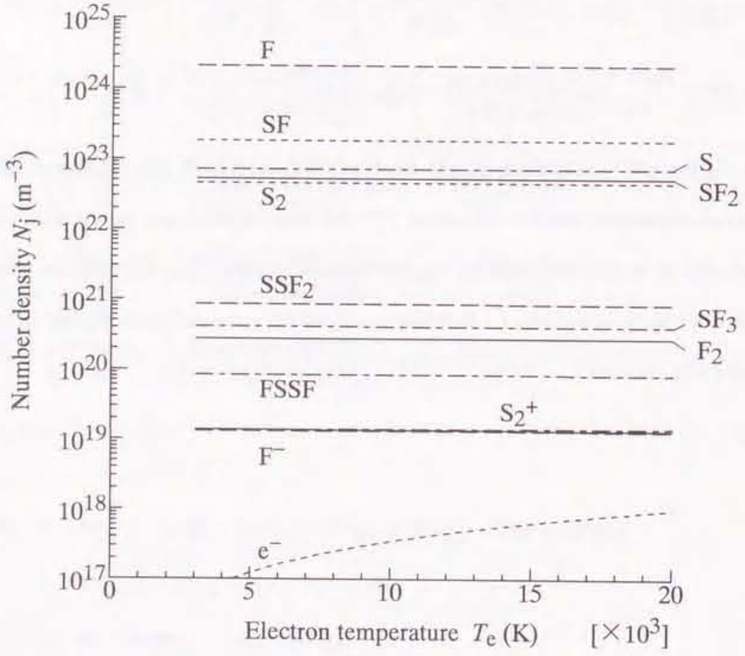

Figure 5.2. Particle composition of two-temperature SF_6 plasma at 0.1 MPa as a function of electron temperature. Gas temperature is fixed at 3000 K.

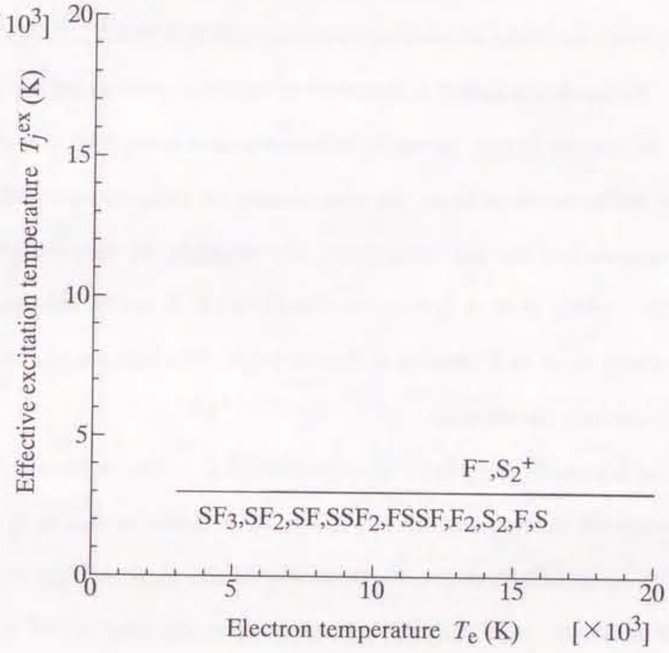

Figure 5.3. Effective excitation temperature of various species in two-temperature SF_6 plasma at 0.1 MPa as a function of electron temperature. Gas temperature is fixed at 3000 K.

than those between heavy particles. In other words, the heavy particles collide more frequently with the other heavy particles than with electrons. As a result, T_j^{ex} of the heavy particle remain T_g regardless of T_e. As a consequence, T_e hardly affects dissociation and ionization reactions, resulting in insignificant change in the composition.

Figure 5.4 represents the obtained particle composition at fixed $T_g = 6000$ K as a function of T_e. No significant change in composition are found with increasing T_e from 6000 to 8000 K. In contrast to this, raising T_e to temperatures above 9000 K leads to marked dissociation and ionization of heavy particles, causing the composition to differ from that under the condition of thermal equilibrium. For example, N_e rises from 6.24×10^{20} to 9.24×10^{22} m^{-3} with a grow of T_e from 6000 to 12 000 K. It can be also seen in Fig. 5.4 that N_e is almost equal to S^+ density at T_e <15 000 K. This indicates that the ionization of S mainly produces the electron.

Figure 5.5 represents derived T_j^{ex} as a function of T_e. Let us discuss T_S^{ex} of S that mainly produce the electron. As seen in Fig. 5.5, T_S^{ex} is almost as high as T_g at $T_e < 9000$ K, while T_S^{ex} agrees with T_e at T_e >10 000 K. The results shown in Figs. 5.4 and 5.5 are interpreted as follows : At T_e <9000 K, N_e is as low as the order of 10^{20} m^{-3} so that S is excited or ionized mainly by collision with heavy particles. Thus, T_S^{ex} is kept constant at T_g. On the other hand, Since N_e exceeds 10^{22} m^{-3} at T_e >10 000 K, S is excited or ionized mainly by collision with electrons and thus T_S^{ex} increases to T_e. Consequently, the particle composition depends on T_e markedly and differs from that under the condition of thermal equilibrium.

Figure 5.6 shows the particle composition at fixed T_g=9000 K as a function of T_e. As can be seen in this figure, an increase in T_e induces the dissociation and ionization of all particles, thus causing the number densities of the particle to vary greatly. Figure

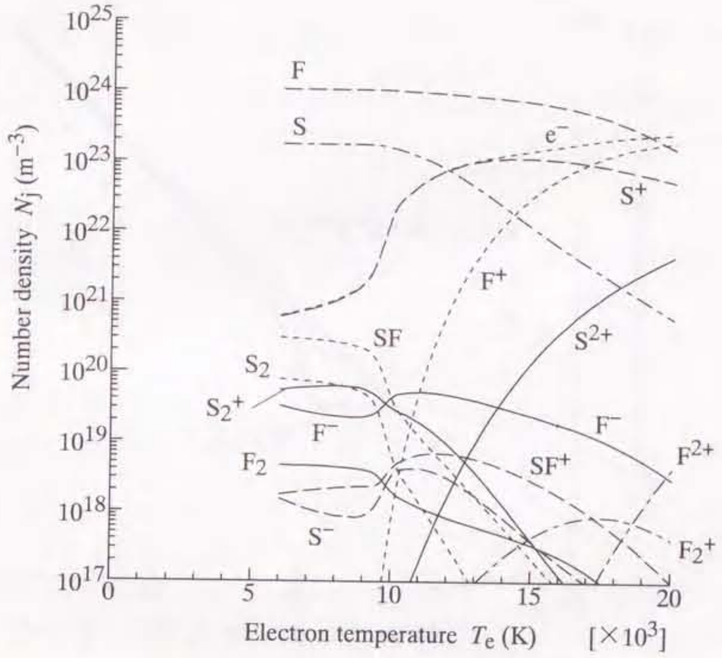

Figure 5.4. Particle composition of two-temperature SF_6 plasma at 0.1 MPa as a function of electron temperature. Gas temperature is fixed at 6000 K.

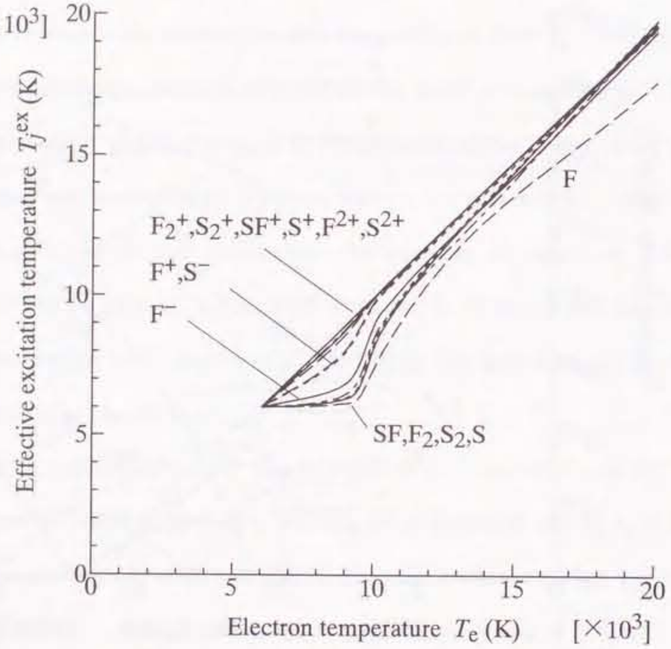

Figure 5.5. Effective excitation temperature of various species in two-temperature SF_6 plasma at 0.1 MPa as a function of electron temperature. Gas temperature is fixed at 6000 K.

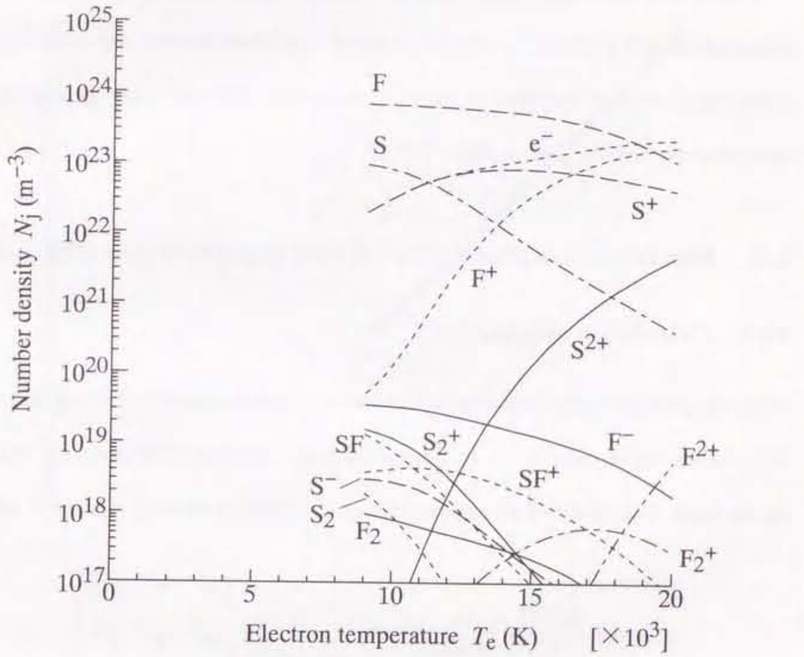

Figure 5.6. Particle composition of two-temperature SF_6 plasma at 0.1 MPa as a function of electron temperature. Gas temperature is fixed at 9000 K.

5.7 represents T_j^{ex} at T_g=9000 K. The effective excitation temperatures of almost all the species rise linearly with T_e. This indicates the particle composition depends almost only on T_e.

Figure 5.8 shows electron density at constant T_g of 6000 K as functions of electron temperature and pressure. It should be noted that there are two region in Fig. 5.8 : One is the region electron density has values of the order of 10^{21} m^{-3}, and another is the region with electron density greater than 10^{23} m^{-3}.

5.3 Electrical conductivity of two-temperature SF_6 plasma

5.3.1 Calculation method

Using the particle composition data thus derived, electrical conductivity of two-temperature SF_6 plasma can be calculated. In this calculation, electrical conductivity σ was computed on the basis of the third order approximation of Chapman-Enskog method as follows [22]:

$$\sigma = \frac{3e^2N_e^2}{2}\left(\frac{2\pi}{m_e k T_e}\right)^{\frac{1}{2}} \times \begin{vmatrix} q^{11} & q^{12} \\ q^{12} & q^{22} \end{vmatrix} \times \begin{vmatrix} q^{00} & q^{01} & q^{02} \\ q^{01} & q^{11} & q^{12} \\ q^{02} & q^{12} & q^{22} \end{vmatrix}^{-1} \tag{5.50}$$

where q^{ij} is the matrix elements concerning the collision integrals. Expressions on these elements are given by Devoto [22].

5.3.2 Calculation results

Figure 5.9 shows σ of two-temperature SF_6 plasma at P=0.1 MPa as functions of T_e and T_g. The bold curves designate the dependence of σ on T_e at fixed T_g=3500, 6000 and 9000 K.

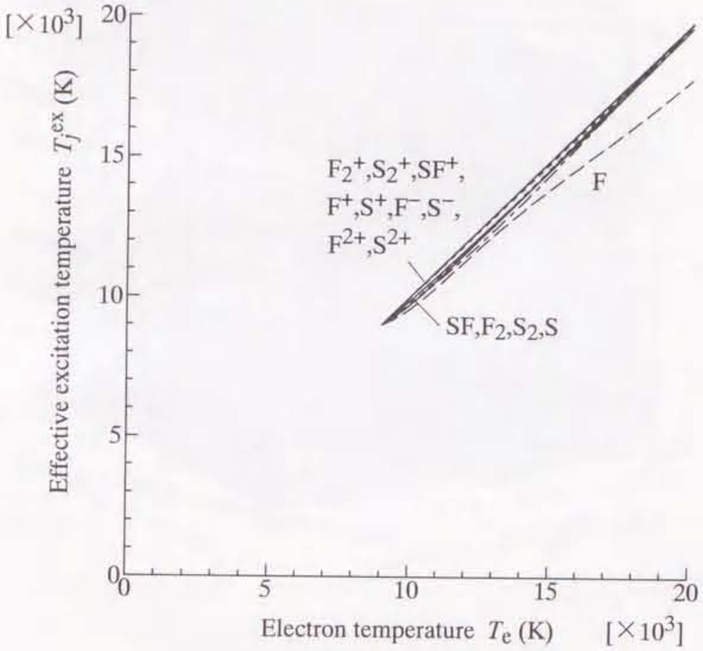

Figure 5.7. Effective excitation temperature of various species in two-temperature SF_6 plasma at 0.1 MPa as a function of electron temperature. Gas temperature is fixed at 9000 K.

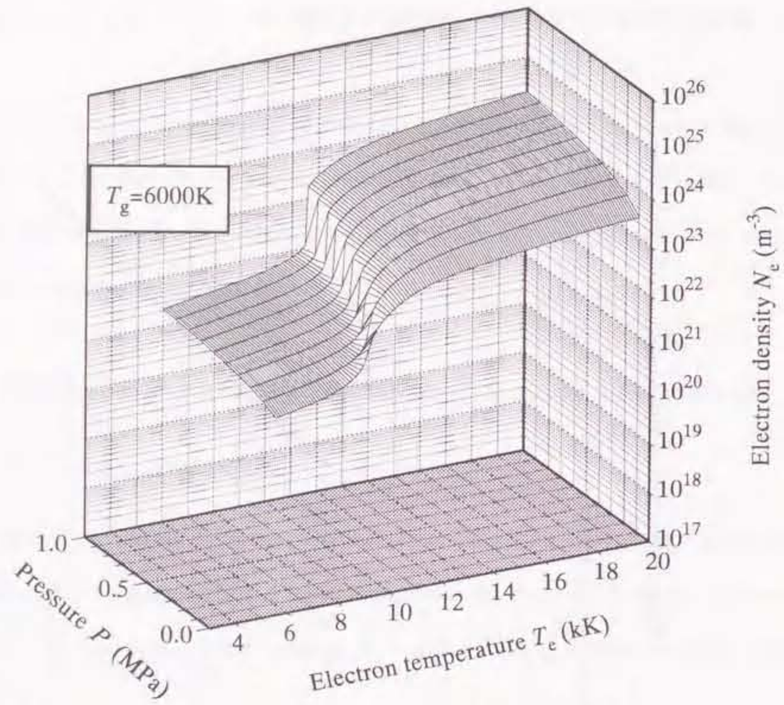

Figure 5.8. Electron density in two-temperature SF_6 plasma as functions of electron temperature and total pressure. Gas temperature is fixed at 6000 K.

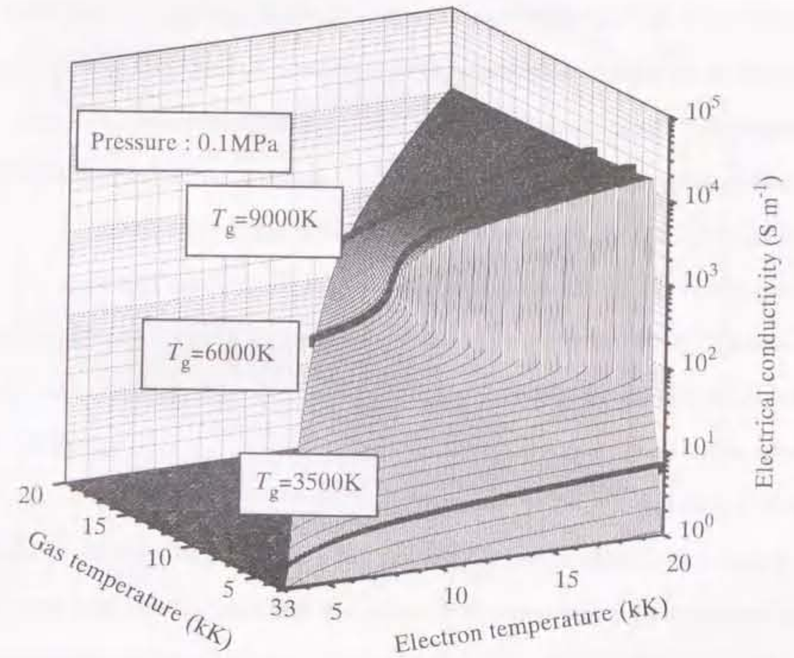

Figure 5.9. Electrical conductivity of SF_6 plasma in two-temperature state at a pressure of 0.1 MPa as functions of electron and gas temperatures.

At a fixed T_g=3500 K, σ slightly increases with T_e. For instance, at T_e=20 000 K, σ is 5.82 S m^{-1}, which is 3.55 times as high as that under the condition of thermal equilibrium at $T_e = T_g$=3500 K. In the case of T_g=6000 K, a rise of T_e from 6000 to 8000 K yields to the gradual development of σ. Increasing T_e from 8000 to 9000 K enhances σ drastically. This is responsible mainly to the encouragement of the ionization of S due to very frequent collisions with electrons. At T_e=20 000 K, σ reaches to 1.36×10^4 S m^{-1}. At a fixed T_g=9000 K, σ gradually rises with T_e from 9000 to 20 000 K.

Let us now discuss the dependence of σ on T_g in the case that T_e is fixed. For example at a fixed T_e=20 000 K, σ is almost independent of a change in T_g from 6000 to 20 000 K. The similar dependence of σ on T_g is found at fixed T_e from 9000 to 20 000 K. The above results reveal that σ is predominated almost entirely by T_e in the range of T_g >6000 K and T_e >9000 K.

Figure 5.10 demonstrates the dependence of σ at fixed T_g=6000 K on T_e and P. The bold curves in Fig. 5.10 denote σ at a fixed T_e=10 000 and 15 000 K. At a fixed T_e below 10 000 K, rising P reduces σ. This arises from the following fact that the pressure rise at T_e <10 000 K causes the greater collision frequency between heavy particles than those between the electron and heavy particles. This leads to the dominance of T_g in T_j^{ex} to decline the ionization reactions. On the other hand at T_e above 12 000 K, higher P elevates σ. This is because the at T_e >12 000 K the higher P produces more n_e.

5.4 Conclusions

Particle composition of SF_6 plasma above 0.1 MPa in two-temperature state was theoretically calculated, in which electron temperature T_e is higher than gas temperature T_g. In order to simply express the populations of the internal energy states of heavy particles,

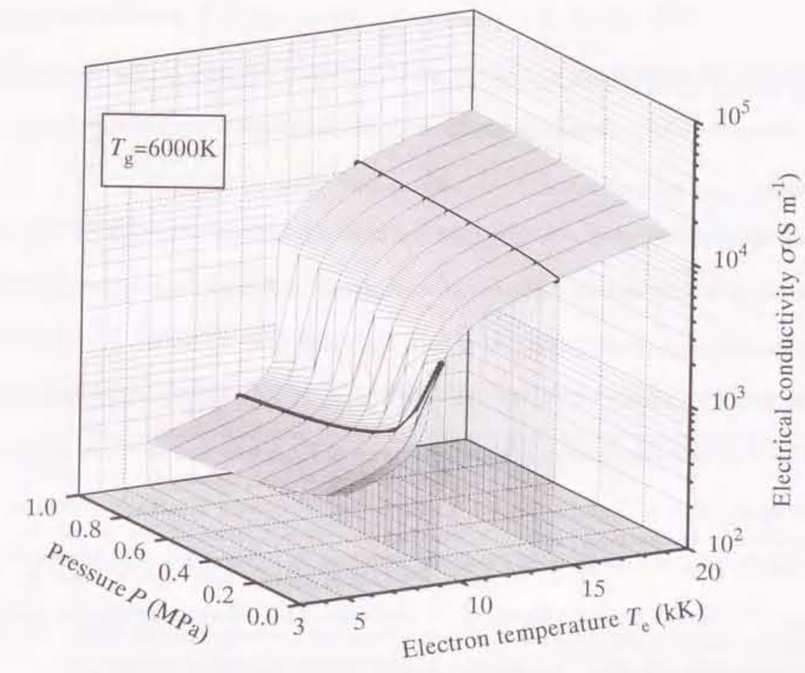

Figure 5.10. Electrical conductivity of SF_6 plasma in two-temperature state as functions of electron temperature and total pressure. Gas temperature is fixed at 6000 K.

the effective excitation temperature was proposed considering collision frequency. At fixed T_g in the range of 6000–9000 K at a pressure of 0.1 MPa, a rise of T_e from 9000 to 20 000 K encourages the dissociation and ionization of particles, resulting in the composition of SF_6 plasma to differ markedly from the composition under the condition of thermal equilibrium.

Electrical conductivity σ was computed for two-temperature SF_6 plasma using the composition data thus derived. Electrical conductivity σ is one of the most important factor dominating arc interruption. At a fixed T_g <4500 K or T_g >9000 K, σ increases gradually with T_e up to 20 000 K. On the other hand, at a fixed T_g in range from 4500 to 9000 K, σ drastically elevates in a certain range of T_e, finally having the maginitude of the order of 10^4 S m^{-1} at T_e=20 000 K. Therefore, increasing T_e greatly affects on σ in this gas temperature range in SF_6 plasma, resulting in a decrease in the interrupting capablility of a circuit breaker. This may be very serious for an arc interruption, since a post-arc channel usually has temperatures around 6000 K just after current zero.

References

[1] M. T. C. Fang, Q. Uhuang, and X. J. Guo, "Current-zero behaviour of an SF_6 gas-blast arc. part II : turbulent flow", *J. Phys. D: Appl. Phys.*, Vol. 27, pp.74–83, 1994.

[2] J. J. Gonzalez, A. Gleizes, and P. Krenek, "SF_6 circuit breaker arc modelling : influence of the electric field on the electrical conductivity", *J. Phys. D : Appl. Phys.*, Vol. 27, pp.985–993, 1994.

[3] D. Kannappan, and T. K. Bose, "Transport properties of a two-temperature argon plasma", *Phys. Fluids*, Vol. 20, pp.1668–1673, 1977.

[4] K. Chen and T. L. Eddy, "Composition and partition functions of partially ionized hydrogen plasma in non-local thermal equilibrium (Non-LthE) and non-local chemical equilibrium (Non-LChE)", *J. Non-Equilib. Thermodyn.*, Vol. 18, pp.1–18, 1993.

[5] E. Richley and T. Tuma, "On the determination of particle concentrations in multitemperature plasmas", *J. Appl. Phys.*, Vol. 53, pp.8537–8542, 1982.

[6] E. J. Miller and S. I. Sandler, "Transport properties of two-temperature partially ionized argon", *Phys. Fluids*, Vol. 16, 491–494, 1973.

[7] M. C. M. van de Sanden, P. P. J. M. Schram, and A. G. Peeters, "Thermodynamics generalization of the Saha equation for a two-temperature plasma", *Phys. Rev. A*, Vol. 40, pp.5273–5276, 1989.

[8] A. Morro and M. Romeo, "The law of mass action for fluid mixtures with several temperatures and velocities", *J. Non-Equilib.*, pp.339–353, 1988.

[9] A. A. Abrahamson, "Born-Mayor-type interatomic potential for neutral ground state atoms with U=2 to U=105", *Phys. Rev.*, Vol. 178, pp.76–79, 1969.

[10] L. Monchick, "Collision integrals for the exponential repulsive potential", *Phys. Fluids*, Vol. 2, pp.695–700, 1959.

[11] J. O. Hirschfelder, C. F. Curtiss and R. B. Bird, *Molecular Theory of Gases and Liquids*. New York : John Wiley & Sons, 1954, p.168.

[12] D. Rapp and W. E. Francis, "Charged exchange between gaseous ions and atoms", *J. Phys. D: Appl. Phys.*, Vol. 37, pp.2613–2615, 1962.

[13] E. J. Robinson and S. Geltman, "Single and double photodetachment of negative ions", *Phys. Rev.*, Vol. 153, 4–8, 1967.

[14] S. Chapman and T. G. Cowling, *The Mathematical Theory of Non-Uniform Gases*. London : Cambridge University Press, 1958, ch.10, p.168.

[15] J. M. Yos, *Transport properties of nitrogen, hydrogen, oxygen and air to 30 000 K, Technical Memorandum RAD-TM-63-7*. Research and Advanced Development Division, AVCO Corp, Massachusetts, 1963, pp.14–15.

[16] M. W. Chase Jr., C. A. Davles, J. R. Downey Jr., D. J. Frurip, R. A. McDonald and A. N. Syverud, *JANAF Thermochemical Tables, 3rd ed. Vol.14 Suppl.1*. Washington DC : NBS, 1985.

[17] C. E. Moore, *Atomic Energy Levels*. Washinton DC : NBS, 1949.

[18] G. Herzberg, *Molecular Spectra and Molecular Structure IV Constants of Diatomic Molecules*. New York : Van Nostrand Reinhold, 1979.

[19] F. Burhorn and R. Winecke, "Berechnung der inneren Umstandssummen einiger zweiatomiger Moleküle bei höheren Temperaturen", *Z. Phys. Chem. Leipz.*, Vol. 212, pp.105–117, 1957.

[20] G. Herzberg, *Molecular Spectra and Molecular Structure II Infrared and Raman Spectra of Polyatomic Molecules*. New York : D Van Nostrand, 1966, pp.501–510.

[21] M. I. Boulos, P. Fauchais and E. Pfender, *Thermal Plasmas, Fundamentals and Applications, Vol. 1*. New York : Plenum, 1994, p.253.

[22] R. S. Devoto, "Simplified expressions for the transport properties of ionized monatomic gases", *Phys. Fluid*, Vol. 10, pp.2105–2112, 1967.

Chapter 6 Conclusions

6.1 Introduction

In an SF_6 gas-blast circuit breaker, an ac arc discharge burns between the electrodes during current interruption processes. The arc discharge is extinguished at current zero following a peak current of several thousands of amperes. After current zero, there remains a post-arc channel with a temperatures of about 6000 K between the electrodes. The diagnosis of physical state in the post-arc channel is therefore greatly important for the understanding of arc quenching processes.

Several papers have described experimental approaches to study SF_6 gas-blast arcs. In these experiments, the spectroscopic observation techniques have often been performed to estimate arc parameters such as temperature, electron density and metallic vapor concentration. However, these experiments were limited to peak current phase. On the other hand, few research studies on the post-arc channel after current zero have been published. This is mainly because the radiation intensities of spectral lines emitted from ions and atoms such as S^+, F or Cu are hardly detectable in the post-arc channel.

In the present dissertation, a post-arc channel after current zero was investigated fundamentally in a flat-type SF_6 gas-blast quenching chamber with a gas flow rate of 50 liters min^{-1}. First, the post-arc temperature was measured using the radiation intensities of two spectral lines emitted from Fe. Iron was intentionally used as an electrode material. The time variation in temperature of post-arc channel for peak current of 5 kA was estimated, and transient axial temperature distribution up to 100 μs after current zero

was discussed. Secondly, a method for estimating the metallic vapor concentration in a post-arc channel was developed. The use of this method permitted the estimation of the iron vapor concentration up to 100 μs after current zero. Thirdly, the electrical resistivity of a post-arc channel was obtained. From this result, a new concept about the thermal plasma contacts was introduced in order to interpret the arc quenching processes. Behavior of these thermal plasma contacts were discussed. Finally, a post-arc channel exposed to high electric field originating from a transient recovery voltage was numerically investigated considering non-local thermal equilibrium effects i.e. two-temperature effects. The particle composition and electrical conductivity of SF_6 plasma in two-temperature state were theoretically calculated.

The results derived in this dissertation are summarized in the following sections.

6.2 Measurement of axial temperature distribution in post-arc channel

In chapter 2, the following facts were found :

(1) Theoretical calculations were made for emission coefficients of 132 main Fe spectral lines in SF_6 gas at a pressure of 0.1 MPa as a function of temperature under the condition of thermal equilibrium. The calculated results reveal that Fe spectral lines at wavelengths of 426.0 and 442.7 nm have much higher emission coefficients than S^+, F or Cu at temperatures below 5000 K.

(2) In the experiment, a flat-type SF_6 gas-blast quenching chamber was adopted. Adoption of a flat-type chamber facilitates measurement of arc radiations and discussion of arc quenching processes. Iron was intentionally used as an electrode material for

the injection of iron vapor into a post-arc channel. The radiation intensities I_{Fe426} and I_{Fe443} of the two Fe spectral lines at 426.0 and 442.7 nm were measured along the nozzle axis. These spectral lines were detectable up to 100 μs after current zero under the condition that the peak current is 5 kA and SF_6 gas flow rate is 50 liters min^{-1}. Furthermore, the use of the two-line method to the Fe spectral lines enabled the author to determine the temperature in the post-arc channel. The temperature decay could be estimated up to 100 μs after current zero.

(3) The radiation intensities of the two Fe spectral lines were measured at five positions along the nozzle axis in the flat-type SF_6 gas-blast quenching chamber. At each of the five positions, these spectral lines could be detected up to 100 μs after current zero. From the radiation intensities of these spectral lines, the axial temperature distribution was obtained. The results revealed that the temperature in the post-arc channel decreased more rapidly at the nozzle throat than at the other axial positions. The temperature at the nozzle throat decays from 5000 to 3500 K from 0 to 100 μs after current zero.

6.3 Method for estimating metallic vapor concentration in post-arc channel and its axial distribution

In chapter 3, the following facts were obtained :

(1) In the spectroscopic observation, the radiation intensity I_{455} of background spectra at a wavelength of 455.0 nm was simultaneously measured. The reason was as follows : since measured radiation intensities I'_{426} and I'_{443} at 426.0 and 442.7 nm were found to contain the background radiation, so the subtraction of I_{455} from I'_{426}

and I'_{443} was required to obtain the net radiation intensities I_{Fe426} and I_{Fe443}.

For the estimation of metallic vapor concentration using these radiation intensity of background spectra, emission coefficient of continuous spectra has to be calculated. Therefore, emission coefficient ε_{cont} of continuous spectra at 455.0 nm in SF_6 gas was theoretically calculated in the temperature range of 3000–6000 K. However, the temperature dependence of ε_{cont} is found to show no agreement with that of I_{455} in the temperature range from 3000 to 5000 K.

(2) Emission coefficients ε_{S_2455} of S_2 spectra due to $B^3\Sigma_u^- - X^3\Sigma_g^-$ transition at 455 nm in SF_6 gas were theoretically calculated as a function of temperature. The total emission coefficient ε_{455} of background spectra was derived by summing ε_{S_2455} and ε_{cont}. The temperature dependence of ε_{455} agreed fairly well with that of I_{455}. From the results, it is found that the background spectra at 455.0 nm is dominated by not continuous spectra but molecular spectra at temperatures below about 4500 K.

(3) A method for estimating metallic vapor concentration was developed : a radiation intensity ratio of background spectra to Fe spectral line was utilized.

This method was applied to the post-arc channel in the flat-type SF_6 gas-blast quenching chamber with the iron electrodes. From the measured radiation intensities, iron vapor concentration was successfully estimated up to 100 μs after current zero.

(4) An axial distribution of iron vapor concentration was also obtained around current zero. From the results, the iron vapor concentration was found to have a magnitude of 0.01% at all observed positions along the nozzle axis during the time around current zero.

6.4 Thermal plasma contact

In chapter 4, the following facts were found.

(1) An electrical resistivity ρ_{res} of SF_6 gas contaminated with iron vapors was theoretically calculated by the first order approximation of Chapman-Enskog method. Using the theoretical data, ρ_{res} was estimated from the measured temperature and iron vapor concentration. The result showed that ρ_{res} increases more drastically at the nozzle throat than at the other axial positions. At 100 μs after current zero ρ_{res} at the nozzle throat became 4.3 Ωm which is about 340 times higher than that at current zero.

(2) The low electrical resistivity regions were found in front of the electrodes. The distance between these regions is observed to increase with time. This increasing process was regarded as an opening process of fictitious 'contacts' made of thermal plasma. Furthermore, the opening velocity of these 'thermal plasma contacts' was estimated to be higher than 100 m s^{-1}. This value is very much higher than the opening velocity of mechanical contacts in a practical circuit breaker. These results led to the conclusion that SF_6 gas-blast circuit breakers may interrupt high currents through the opening process of these thermal plasma contacts.

(4) The transient temperature, electrical resistivity and current density were computed when a transient recovery voltage was applied across the electrodes in a one dimensional axial model. In this calculation, the rate of rise of recovery voltage RRRV was taken as a parameter. At RRRV=2.0 V μs^{-1}, the current density is found to converges to zero and this was regarded as to denote the success of current interruption. On the other hand, the divergence of current density at RRRV=3.0 V μs^{-1}

was considered to be the failure of current interruption. In both cases, behavior of thermal plasma contacts were discussed. In the case of the success of current interruption, the thermal plasma contacts continue to move apart during the arc quenching process. However, in the case of the failure of current interruption, the thermal plasma contacts are unable to keep up the opening process.

6.5 Particle composition and electrical conductivity of two-temperature SF_6 plasma

In practice, after current zero, the post-arc channel across the electrodes in a circuit breaker is subjected to TRV. The post-arc channel is therefore exposed to high electric field strength due to TRV. The high electric field elevates the kinetic energy of electrons in the post-arc channel and thereby increases the electron temperature T_e. As a result, T_e can be higher than gas temperature T_g in the post-arc channel. In these two-temperature states, the properties of SF_6 plasmas such as particle composition, transport and thermodynamic properties may differ from those under the condition of thermal equilibrium. Thus, the composition and electrical conductivity of SF_6 plasmas in two-temperature states were calculated in chapter 5.

In the calculation of particle compositions, in order to express the populations of the internal energy states of heavy particles, effective excitation temperature was proposed. The effective excitation depends on both T_e and T_g. The equations defining the ionization and dissociation equilibrium were developed for two-temperature SF_6 plasmas. The Newton-Raphson method was adopted to derive the particle composition of two-temperature SF_6 plasmas. Using the composition data thus derived, an electrical conductivity was also

computed for two-temperature SF_6 plasmas. From these calculations, the following facts were found :

(1) At a constant T_g of 3000 K and T_e in the range of 3000 to 20 000 K, there is slight change in particle composition, thus the electrical conductivity increases slightly with T_e. This is mainly because the electron density is as low as of the order of 10^{17} m^{-3}. Therefore, heavy particles excited through collisions mainly with heavy particles.

(2) At a constant T_g=6000 K, no significant change in the composition is found with an increase in T_e from 6000 to 9000 K. In contrast to this, T_e above 9000 K leads to a marked dissociation and ionization of heavy particles, causing the composition to differ from that under the condition of thermal equilibrium. This drastic change develops the number densities of charged particles, thus enhancing the electrical conductivity remarkably. An enhanced electrical conductivity arising from higher electron temperature than gas temperature can result in the lower interrupting capability of a circuit breaker.

(3) In the case of a constant T_g=9000 K, an increase in T_e encourages the dissociation and ionization of all particles, thus causes the composition to vary. This results in the gradual enhancement of the electrical conductivity.

6.6 Scope for the future research

In the present work, the facts mentioned in the previous sections were derived. However, much more investigations are necessary in order to understand fully arc quenching phenomena.

In chapters 2 and 3, the methods for estimating temperature and iron vapor concentration in a post-arc channel were devised. These methods were adopted to the arcs in a flat-type SF_6 gas-blast quenching chamber. It was found that the nozzle throat is a significant position for an arc interruption process in the adopted flat-type SF_6 gas-blast quenching chamber. However, the physical reason for this has not been revealed completely. Some effects such as the velocity distribution of gas flow, pressure, energy balance as well as the nozzle ablation are considered. Therefore, theoretical approaches on this point should be performed, for example, using the computational fluid dynamics. It is of interest to measure the temperature distribution of post-arc channel under different conditions for pressure, gas flow rate, interrupting current and nozzle shape. Furthermore, both experimental and theoretical understanding of the relationship between arc behavior in the small-scale chamber used in this work and that in the practical circuit breaker is very important problem, although it is extremely diffult problem to solve. These approaches would prove helpful to fundamentally understand the arc quenching phenomena.

In chapter 5, particle compositions of SF_6 plasmas in non-thermal equilibrium, i.e. two-temperature state were calculated. The author believes that this is a novel approach for elucidation of the arc interruption phenomena. In the calculation, it was assumed that chemical equilibrium exists although the electron temperature becomes higher than gas temperature. For the next step, the calculations of transport properties including thermal conductivities, viscosity and diffusion coefficients should be performed. The use of these properties would likely to enable one to simulate arc in two-temperature state. These calculations are going to be helpful to clarify systematically the two-temperature effects on arc interruption.

An electric arc is often diagnosed and simulated on the assumption of local thermal equilibrium, as indicated in the present dissertation. This assumption is generally valid for a stationary arc or for a slow transient arc. However, for a transient arc with very rapid decay such as in a circuit breaker, the assumption of LTE may not always be valid when the gas pressure is above 0.1 MPa. Even chemical equilibrium may not occur because the chemical reactions such as ionization, dissociation and their reverse reactions require non-zero time of the order of 10^{-5}s. For this reason, plasma diagnosis and plasma simulation without the assumption of LTE should be used.

Furthermore, arc interruption phenomena involve a large number of physical processes such as nozzle ablation, electrode evaporation, recombination, electron attachment, dissociation, charge exchange and so on. The role of each of these elementary processes in arc quenching should be investigated for elucidation of the arc interruption phenomena, although numerous data on various cross sections, reaction rates have to be amassed.

The author believes that these fundamental approaches will reveal the mechanism of arc interruption.

Acknowledgements

The author would like to express his great appreciation to Professor Toshiro MATSUMURA, Department of Electrical Engineering, Nagoya University, for his encouragement and instructive suggestions in completing this dissertation.

The author is deeply grateful to Professor Hideo SUGAI, Department of Electrical Engineering, Nagoya University, for his helpful advices in preparing this dissertation.

The author is greately indebted to Professor Hitoshi OKUBO, Department of Electrical Engineering, Nagoya University, for his valuable discussions in preparing this dessertation.

The author wishes to express his gratitude to Professor Yukio KITO, President of Toyota National College of Technology and Emeritus Professor of Nagoya University, for his inspiring guidance throughout the course of this work.

The author is sincerely grateful to Associate Professor Yasunobu YOKOMIZU, Department of Electrical Engineering, Nagoya University, for his inspiring guidance and encouragement throughout the course of this work.

The author wishes to express his gratitude to the members of Professor MATSUMURA's laboratory for their help and encouragement.

The understanding and constant encouragement of the author's parents, sister and friends were invaluable.

List of Papers Concerned with this Dissertation

Chapter	Title	Journal & Date	Author
2	Transient behaviour of axial temperature distribution in post-arc channel after current zero around nozzle throat in flat-type SF_6 gas-blast quenching chamber	J. Phys. D: Appl. Phys., Vol.28, pp.2095–2103, 1995	Y. Tanaka Y. Yokomizu T. Matsumura Y. Kito
	Transient distributions of arc temperature and its electrical resistivity along nozzle throat axis around current zero in a flat-type SF_6 arc chamber	Proc. 11th Int. Conf. on Gas Discharges and Their Applications, Tokyo, 1995, Vol.I, pp.42–45	Y. Tanaka Y. Yokomizu T. Matsumura Y. Kito
3	Dominant spectra of background radiation in an SF_6 post-arc channel	IEEE Trans. Plasma Sci., Vol.25, pp.986–990, 1997	Y. Tanaka Y. Yokomizu M. Ishikawa T. Matsumura Y. Kito
	Transient distribution of metallic vapour concentration in post-arc channel after current zero along nozzle axis in a flat-type SF_6 gas-blast quenching chamber	J. Phys. D: Appl. Phys., Vol.29, pp.1540–1550, 1996	Y. Tanaka Y. Yokomizu T. Matsumura Y. Kito
	Diagnosis of temperature and metallic vapour concentration in post-arc at nozzle throat in flat-type SF_6 gas-blast quenching chamber	Proc. 7th Annual Conf. of Power & Energy Society IEE Japan, Osaka, 1996, pp.345–350	Y. Tanaka Y. Yokomizu T. Matsumura Y. Kito

(Continued)

Chapter	Title	Journal & Date	Author
4	The opening process of thermal plasma contacts in a post-arc channel after current zero in a flat-type SF_6 gas-blast quenching chamber	J. Phys. D: Appl. Phys., Vol.30, pp.407–416, 1997	Y. Tanaka Y. Yokomizu T. Matsumura Y. Kito
	Opening process of fictitious contacts made of thermal plasma after current zero in a flat-type SF_6 gas-blast quenching chamber	IEE of Japan, Vol.116-B, pp.1204–1211, 1996 (in Japanese)	Y. Tanaka Y. Yokomizu T. Matsumura Y. Kito
5	Particle composition of high-pressure SF_6 plasma with electron temperature greater than gas temperature	IEEE Trans. Plasma Sci., Vol.25, pp. 991–995, 1997	Y. Tanaka Y. Yokomizu M. Ishikawa T. Matsumura
	Particle composition of two-temperature SF_6 plasma in pressure range from 0.1 to 1 MPa	Proc. 12th Int. Conf. on Gas Discharges and Their Applications, Greifswald, 1997, Vol.II, pp.566–569.	Y. Tanaka Y. Yokomizu T. Matsubara T. Matsumura
	Electrical conductivity and enthalpy of two-temperature SF_6 plasma at a pressure of 0.1 MPa	Proc. Int. Conf. on Electrical Engineering '97, Matsue, 1997, pp.726–729	Y. Tanaka Y. Yokomizu M. Ishikawa T. Matsumura
	Electrical conductivity and enthalpy of SF_6 plasma in two-temperature state	Proc. 12th Int. Conf. on Gas Discharges and Their Applications, Greifswald, 1997, Vol.I, pp.94–97	Y. Tanaka Y. Yokomizu T. Matsubara T. Matsumura